UNIVERSITÀ
DEGLI STUDI
DI PADOVA

DIPARTIMENTO
DI INGEGNERIA
DELL'INFORMAZIONE

DEPARTMENT OF INFORMATION ENGINEERING

MASTER THESIS IN
ICT FOR INTERNET AND MULTIMEDIA - INGEGNERIA PER LE COMUNICAZIONI MULTIMEDIALI E INTERNET

"Implementation of polarization sensitive OCT"

Supervisor: Prof. Palmieri Luca

Master Candidate: Camillo Alessandro

ACADEMIC YEAR 2021 – 2022

18/10/2022

Abstract

This thesis aims to be a guide to the realization of a functional Polarization sensitive OCT (PS-OCT) system.

OCTs are interferometric technologies used for generating 2D or 3D images of samples. In the first and second chapters there is an introduction to the terminologies and an explanation of the principles upon which these imaging devices works. In chapter 2 we will also discuss the two classes of OCT technologies which are: Time Domain OCT (TD-OCT) and Fourier Domain OCT (FD-OCT).

In chapter 3 we start discussing the implementation of a FD-OCT making use of the Sweep-Source technique. In this chapter we discuss the realization of a typical OCT imaging system which is capable to generate intensity images. Once we discuss the realization of the optical circuit we will cover the implementation of the software required to generate the images and correct distortions introduced by the components.

In chapter 4 we further evolve the set up in order to obtain a PS-OCT. The process consist in the realization of a second input channel and the implementation of code for the evaluation of light polarization. The theory regarding light polarization will be discuss in this chapter.

Finally in chapter 5 we first cover the problems in our PS-OCT. then we will analyse an image from a PS-OCT found in the literature in order to have an idea of what polarization images should look like. To conclude we will see images of different materials taken with our system and evaluate the material properties.

Future developments would be the implementation of volumetric imaging and the introduction of indexes for measurement of thickness and polarization variance.

Sommario

Questa tesi ha lo scopo di essere una guida sul implementazione di un sistema OCT con sensibilità della polarizzazione della luce (PS-OCT)

Le tecnologie OCT fanno parte delle tecniche interferometriche usate per la creazione di immagini 2D e 3D. Nel primo e secondo capitolo introduciamo le terminologie e spieghiamo i principi fisici usati da questi dispositivi. Sempre nel capitolo 2 introduciamo le due classi di OCT: OCT nel dominio temporale (TD-OCT) e nel dominio di Fourier (FD-OCT).

Il capitolo 3 coprire l'implementazione di un classico OCT utilizzante la tecnica Sweep-Source per la realizzazione di immagini di intensità. Finito di discutere la realizzazione del circuito ottico copriamo la realizzazione del software che si occupa dell'elaborazione degli input e della compensazione di distorsioni introdotte dall'apparecchiature.

Nel capitolo 4 evolviamo il sistema in modo da disporre di due canali input e aggiungiamo codice per permettere il tracciamento della polarizzazione della luce. Così facendo introdurremmo la sensibilità alle polarizzazioni al nostro macchinario OCT.

Per finire nel capitolo 5 discutiamo i difetti del nostro apparato d'immagine. Dopo di che commentiamo un immagine presa con un sistema PS-OCT estratta dalla letteratura in modo da avere un paragone con cui confrontare le nostre immagini. Finita la spiegazione su come immagini di polarizzazione vanno interpretate andiamo a commentare immagini prese con il sistema implementato.

Sviluppi futuri potrebbero essere l'implementazione di immagini volumetriche e l'introduzione di indici per la misurazione di spessore o la variazione della polarizzazione.

INDEX

CHAPTER 1: Introduction to OCT

1.1 Definition of OCT

Optical Coherence Tomography (or OCT in shorts) is an imaging technique that measures the echoes of backscattered light and their delays to generate high resolutions images. The generated images generally have resolutions in the orders of 1-15 μm[8]. OCT techniques allow enface and volumetric imaging depending on the necessity. Often find applications in the medical field especially in: ophthalmic, intravascular imaging and general endoscopic endeavours[2,3].

In figure 1.1 some example of images taken by OCT technologies.

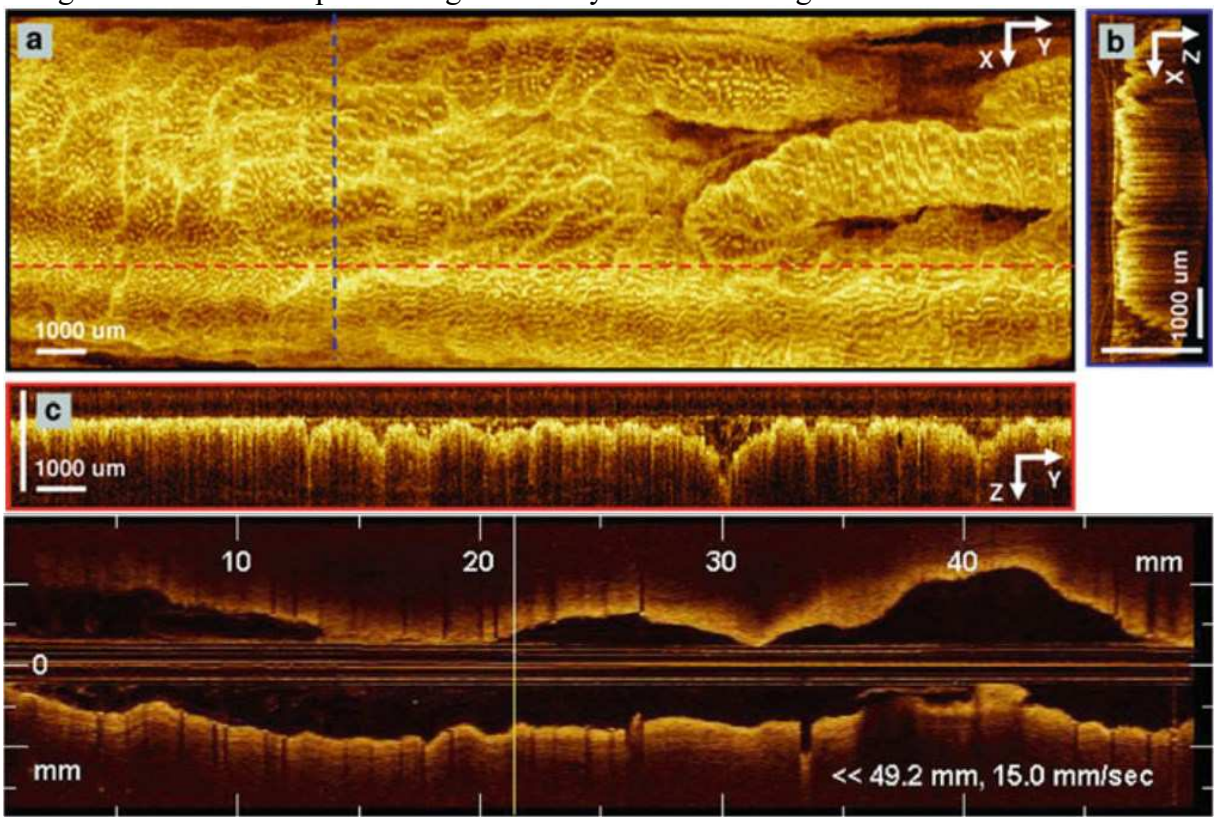

Figure 1.1: top image is an intravascular image of a vein. The lettered images depicts images of human colon obtained with OCT techniques. **a)** is an enface image obtained thanks to the summation of the datasets representing XZ cross-section. **b)** is a XZ cross section of the colon along the blue line in the **a)** image. **c)** is a ZY cross-section taken along the red line in the **a)** image; this image is also obtained by summation of the XZ cross-sections.

1.2 How images are formed in OCT and terminology

There are many OCT techniques with each of them elaborating the measurements of echoes and delays in different ways. Anyway these methodology can be grouped into 3 categories[8]:

- Time Doman OCT (TD-OCT)
- Spectral/Fourier Domain OCT (SD-OCT)
- Swept source/Fourier Domain OCT (SS-OCT)

As we can see the second type and the third can both be referred as Fourier Domain OCT (FD-OCT) since these types use the Fourier transform on the plot acquired[17], which is an amplitude of backscattered light over wavelength into amplitude over distance.

The TD-OCT instead uses a continuous signal and a delay line to produce an interference between the echoes from the sample and the delayed signal. This interference is then transformed into a plot of amplitudes over the time delay between echoes and delayed signal[20]. Since there is a one to one correspondence between time of arrival and distance from the source of the obstacle that is generating the backscattering we can easily obtain once again a plot of amplitudes over distances.

The amplitudes over distances plots obtained are called A-scans and are mapping the backscattered light along the direction we are shining the laser beam. the A-scans are elaborated with algorithms that generates a line of pixel in which there is a correspondence between colour assigned to a pixel and the amplitudes of the corresponding sample [9]. It's common to use grey-scale or false colours.

Now if we collect multiple A-scans taken with parallel beams we can generate an image of the plane called B-scan[7]. The same process can be repeated combining B-scans to obtain volumetric images called C-scans[9]. The process of generation of B-scan and C-scan is summation.

In Figure 1.2 there are examples of: A-scan, B-scan and C-scan.

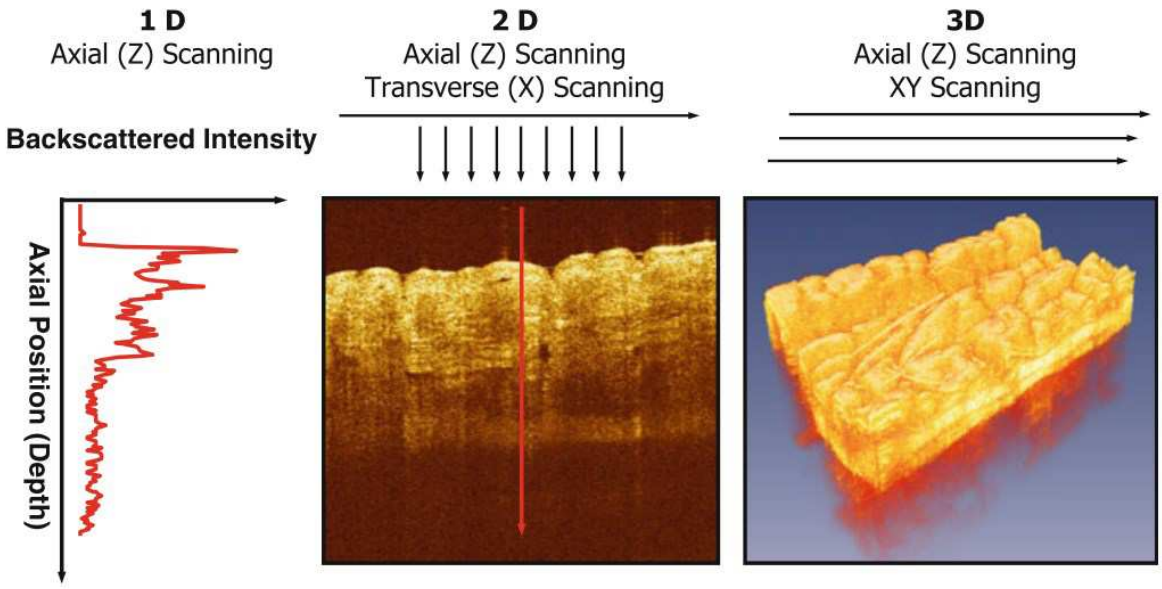

Figure 1.2: from left to right we have an A-scan. The short arrows above the B-scan indicate the direction along which the A-scans maps the scattering; the longer arrow instead shows the direction the beam is moving to take the different A-scans.

Summation refers to the combination of different images in order to obtain other multidimensional images (or matrix) in order to obtain more information [8].

This includes the process for the generation of B-scans that allow us to move from single lines of pixels (that has almost no meaning alone), into an image of the scanned plane which allows to obtain information such as thickness of biological structures or damages. The further step of obtaining C-scans allow us to select cross-sections of the scan region along directions different from the ones actually used to create the volumetric image. one example of this is in Figure 1.3: the images a) Enface B-scans and b) depth B-scans have been combined to create a C-scan that has then been sectioned along different planes in order to generate a new sets of B-scans in image c).

Another way of using summation is to combine B-scans on planes with different orientation in order to obtain more detailed C-scans, by using interpolation algorithms that allow to fill the gaps. An example this is combining a collection of ZY B-scans with a less spatially-dense collection of enface (XY) B-scans. Assuming that the ZY B-scans are on planes separated by 5 pixels on the XY B-scans we can estimate the missing ZY B-scans by cross fitting information from both sets of B-scans allowing us to generate a more accurate volumetric image with more pixel and higher resolution than what we could have gather from using only one type of data.

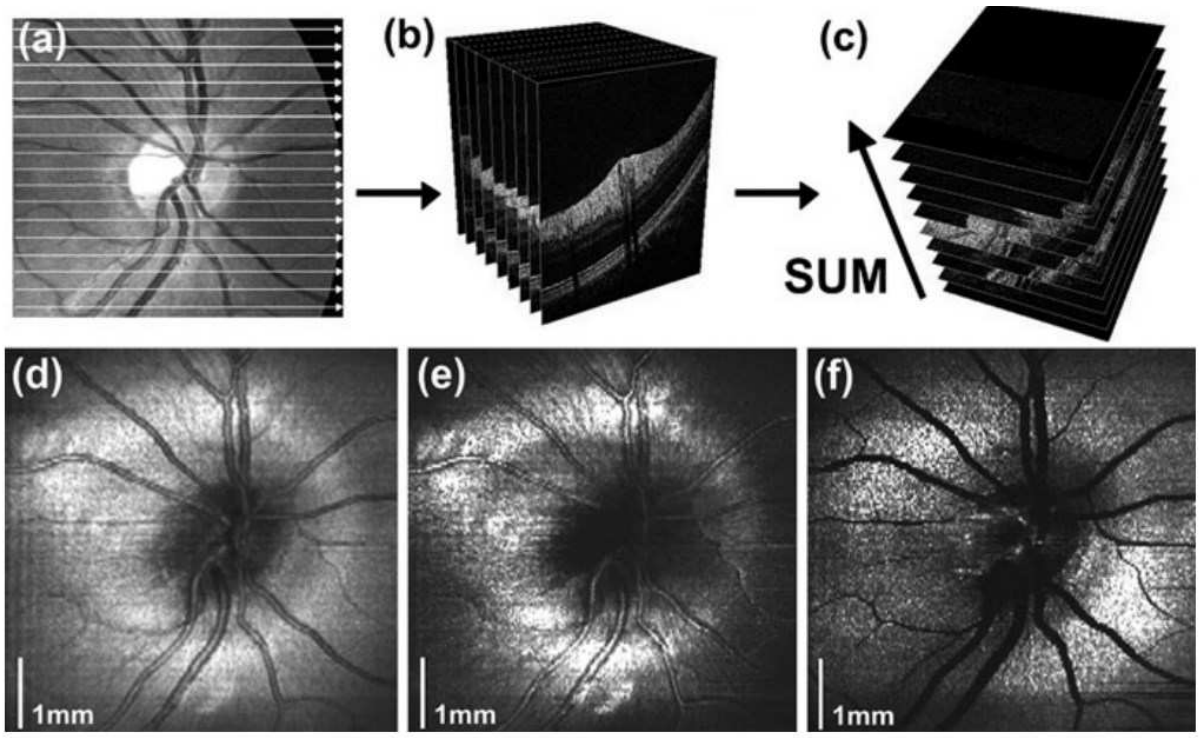

Figure 1.3: an example of combining few enface B-scans (a) with multiple ZY B-scans (b) in order to create a matrix (c) from which we can recover more detailed enface B-scans (d,e,f) at depth at which we did not scan.

We will not talk here on how exactly the A-scans are obtained since it's depends on the category to which the OCT belongs. The argument of measurements and what elaborations are used to generate A-scans will be explained in Chapter 2.

1.3 OCT compared to other technology

As we now know OCT techniques are imagining tools so it's natural to compare them with other imaging technologies such as microscopy and ultrasound.

1.3.1 OCT compared to ultrasound

Ultrasound imaging is a very similar technique to OCT the main difference is that the backscattered waves are sound waves instead of electro-magnetic ones. Even though on paper the general idea is the same the difference in frequencies and speeds of the waves used have many consequences.

In ultrasound we generally use frequencies in the range of 3-40 MHz that leads to image resolutions of 0.1-1 mm; having said that the larger wavelength allow this imaging technology to reach long length inside biological tissue allowing non-intrusive mapping of organs and limbs. In alternative there is the so called high frequency ultrasound that offer resolutions of 15-20 μm; the main problem with this approach is that the resolution is still lower than that offered by OCT and offers image penetration of only 1-2 mm which is still worse than OCT imaging[7].

Overall ultrasound are preferred to OCT when non-invasive imaging of "large" entities (like bones and organs) are required and high precision is unnecessary. Ultrasound technology is also much cheaper than OCT systems since the lower speed of sound allow the use of simple electronics with time resolution of ~100 ns and the direct measurement of the echoes[0]. In OCT systems instead the time resolution required is of 30 fs and also the sensitivity required for direct measurement of the echoes are not reachable by electronic sensors alone; it's required to use other techniques such as interferometry to obtain a readable signal that will require more computation to be transformed in to an images. The overall higher requirement of OCT systems leads to much higher costs[8].

1.3.2 OCT compared to microscopy

Optical and electron microscopy technology use phenomena as: reflection, refraction and diffraction of electromagnetic fields to produce an image of the specimens. Usually the field is used by either wide-field irradiation of the sample or beam scanning of it.
The main feature of this techniques is an extremely high transverse resolution that are below 1 μm. Since the attenuation is very high in biological samples and signals and contrast are degraded by the scattering of unwanted light the depth is confined to a 100 μm in most cases. The extremely limited penetration capability relegate microscopy to only enface imaging which limits the use of this method on sample that have to be superficial or have been extracted from the live specimen[24, 12, 11].
It's interesting to compare the two imaging method in histology (also known as microscopic anatomy). We can find in Figure 1.4 images of the same sample taken with the two methodologies. In OCT images the different tissues are recognisable due to different optical property. This is a plus since we don't need much preparation or the extraction of samples to analyse[12]; but it comes at the expense that many structures like cell nuclei do not have significant differences in optical property and so they are not visible[12].
In microscopy instead thanks to the use of excision it's possible to have samples of tissue to be: processed, embedded, sectioned and strained in order to obtain higher contrast in the optical property of different structure obtaining much more detailed pictures.

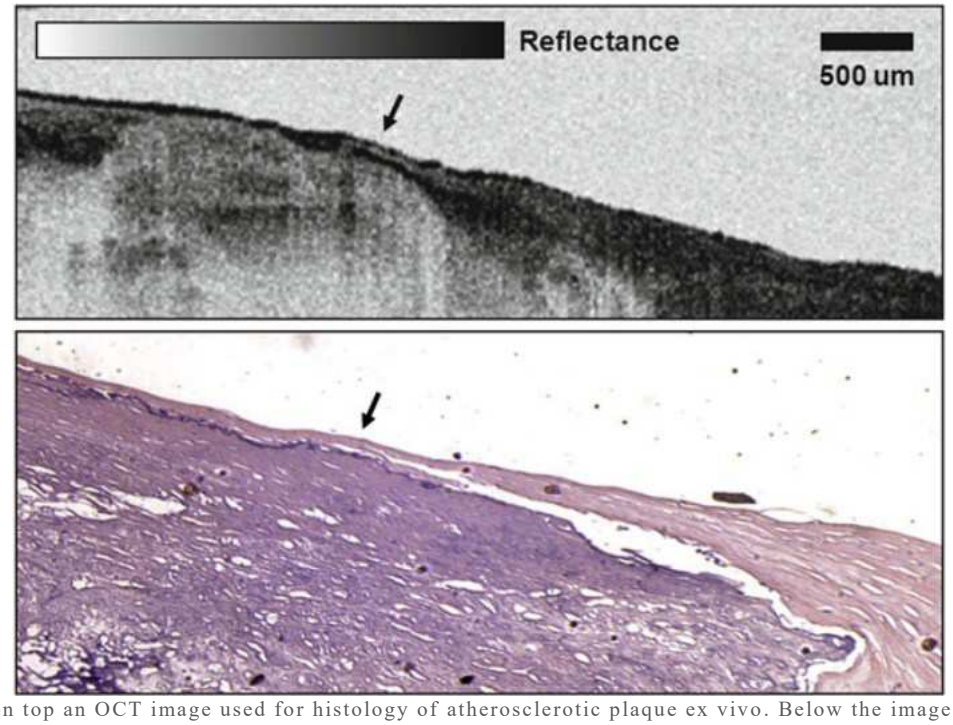

Figure 1.4: on top an OCT image used for histology of atherosclerotic plaque ex vivo. Below the image of the same sample using microscopy[12].

1.3.3 Where OCT found it's place compare to the other two.

To conclude this section on the comparison in Figure 1.5 an image that immodestly gives us an idea of where these methodology stand with respect to one another.

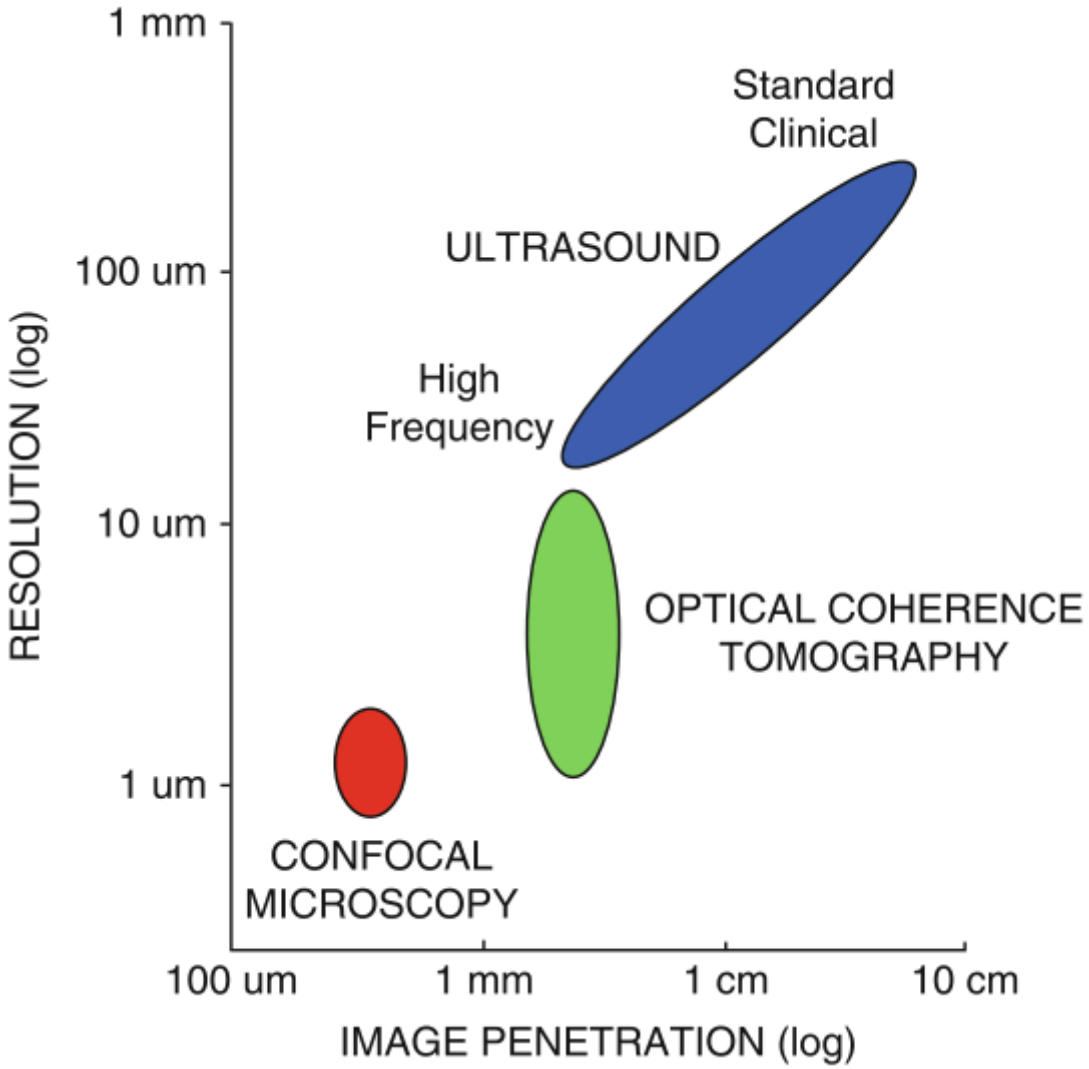

Figure 1.5: a plot of the resolutions and imaging depth possible for the available technology.

As we can see OCT imaging cover a gap that for many years has been between ultrasound and microscopy. At the moment OCT finds use as a real time ultra-high resolution imagining technology capable to allow doctors to make diagnosis without requiring tissue excision that could easily produce false negative if the samples have been extracted in the wrong locations. Also thanks to the low light absorption of the eyes OCT has become the standard in ophthalmic.

1.4 OCT and probes

OCT systems can easily be integrated in probes in order to reach impossible areas for microscopy[14].

This versability has led to improvements in both the intravascular and endoscopic field. In the case of probes using OCT the B-scans are obtained by rotating the probe in order to scan in a 360° angle; this means that the A-scans that forms the XY B-scans are not placed side by side but instead disposed in a radial pattern. Once the radial B-scans is done we then push the device further inside the aperture.

It's important to know that in intravascular probes have to integrate a saline flushing functionality in order to remove blood from the imaging field since it’s a source of high attenuation[13].

Figure 1.6 depict images taken with a saline flushing probe of a blood vessel.

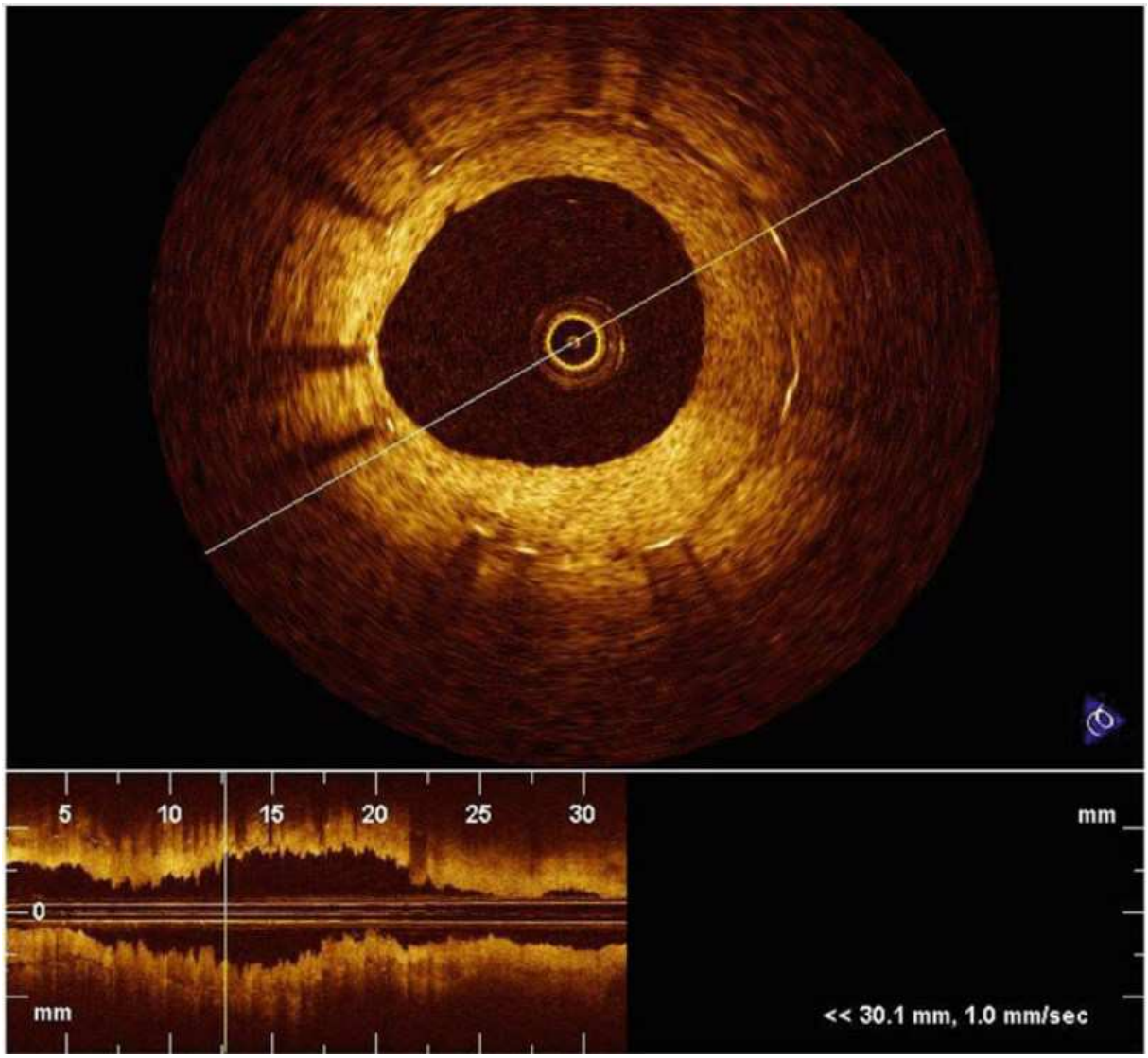

Figure 1.6: on top a radial B-scan of an in vivo artery using saline flushing. On the bottom another B-scan obtained by combining the A-scans of multiple radial B-scans along the selected plane[14]

1.5 Objective of the thesis

This is an experimental thesis in which we aim to realise a working prototype for a polarization sensitive OCT (PS-OCT) imaging tool.
The main improvement of a polarization sensitive OCT compared to traditional ones is the possibility to track how the polarization of light changes in the scanned space. This option is significant since many biological tissues are birefringent. Tracking the polarization rotation of light in the tissue could allow us to more easily distinguish different types of organic materials[27]. Another purpose for polarization sensitive imaging is for early diagnosis of pathologies as glaucoma where there is a build-up of pressure in the eye that will eventually lead to permanent damage to the sight; the higher pressure is noticeable by monitoring stokes parameter since higher concentration of liquids in the eye will lead to an increase of the rotation of light polarization.

Our main goal is to obtain a device capable to generate B-scans (ie two dimensional images of a sample) with the possibility to choose if we want to see a traditional OCT image which is basically just a mapping of the backscattered light on a grey scale or in alternative we can display images obtained from the elaborations of Stokes parameters.
In the second type of images it will be possible to choose if we want to display just one parameter so in this case we will have green pixel where the selected parameter is negative and red where it’s positive while the intensity of the colour is determined by the modulus of the parameter used. In alternative there is the option to display all three parameters in the same picture, but to do that we have to make same considerations so we will not comment on it here.

It's of the outmost importance to keep the program fast and capable to produce the images in real time. To achieve this it has been necessary to learn GPU programming and the use of Nvidia’s CUDA libraries for C++ in order to make use of the high parallel computation capabilities of graphic cards.

We are not interested in realization of C-scans which generally require the collection and memorization of multiple B-scans; also require knowledge of 3D image programs. We discarded this possibility and focussed on learning to create 2D textures to realize B-scans of intensity and polarization (elliptical angles).

1.6 Disclaimer

This thesis is an evolution on previous thesis from Gianluca Marcon named: “design of real time oct” that has been presented on April 18 of 2018.
His software has been used as a bases to develop the polarization sensitive OCT that we will timplement. In particular his code for the control the control of Galvanometric mirrors and for the transfer of the data from the acquisition card to the memory of the PC, have been taken from his work, while we had to add new functionalities.
The new functionalities implemented are:

- Two channel inputs through DAQ.
- Fourier transform of the channel with analytic signal evaluation to reduce aliasing.
- Chromatic compensation.
- Mirror curvature correction.
- Evaluation of Stokes vectors.
- Evaluation of elliptical angles.
- Generation of texture using Stokes parameter and elliptical angles.
- Frequency shifts to fix miss-alignments between channels.

The graphic interface used to pilot the polarization sensitive OCT (PS-OCT) is an evolution of Marcon’s interface to fit the new functionalities.
As far for the OCT design is completely new and so the elaborations of the data after the acquisition is newly made to meet the goals and the necessities of the new setup.

1.7 Structure of the thesis

The chapters that will compose this document will be five.

Chapter 1: is an introduction that aims to offer a definition of what are OCT technologies and how they compare to pre-existent ones.

Chapter 2: here will be recalled the notion from physic necessary to understand the processes that take place in the OCT system. It will also contain an explanation on how the information required to create an image is encoded in the signal generated by the interference.

Chapter 3: will provide an explanation of the set-up that has been implemented. It starts discussing the components used for the optical circuit; how the components impact the specifics of the set up. We follow by describing the two type of reference arms possible and which we choose. To finish we will discuss the data elaborations to used on the channels to produce intensity images typical of standard OCT technologies.

Chapter 4: we talk about light polarization and how it evolves in birefringent materials. Then we discuss on how to evaluate the Stokes parameters and the choices made to decide how the images are created.

Chapter 5: we will first discuss the defects of our system and briefly comment on them. It will be then discuss how the images of the elliptical angles are used to diagnose birefringence or fluctuation in refractive index using an example found in the literature. Then we will show same pictures taken with our machine of a few birefringent and non-birefringent materials and comment them.

CHAPTER 2: THEORY OF OCT

Here we will discuss the basic theory around how OCT's interferometry. So we will quickly cover the interference theory and then proceed to explain the workings of the three types of OCTs.
Some theory like Chromatic Dispersion and Stokes vectors will not be treated here since it's better for the first to be explained when we will talk about compensating dispersions and deformations in chapter 3.
While the Stokes theory is introduced in chapter 4 where we talk in detail about the polarization sensitivity of our device.

2.1 Interference

As we already said in the introduction OCT uses interferometry measurements to obtain the information required to generate images. So here we will cover the basic.

2.1.1 electromagnetic waves

Light is an electromagnetic (EM) radiation propagating through space and hence it has to respect the Maxwell equations:

$$\nabla \cdot \boldsymbol{E} = \frac{\rho}{\varepsilon}$$

$$\nabla \cdot \boldsymbol{B} = 0$$

$$\nabla \times \boldsymbol{E} = -\frac{1}{c}\frac{\partial \boldsymbol{B}}{\partial t}$$

$$\nabla \times \boldsymbol{B} = \frac{1}{c}\left(4\pi \boldsymbol{J} + \frac{\partial \boldsymbol{E}}{\partial t}\right)$$

Must be satisfy in an EM wave in order to have propagation. Assuming we have an homogeneous and isotropic medium in which the EM wave is propagating then the solution of the Maxwell equations is a transverse EM radiation. So a traveling EM wave on a generic cartesian coordinate system is indicated as:

$$S = \{\boldsymbol{E}(\boldsymbol{r}, t) + \boldsymbol{B}(\boldsymbol{r}, t)\}$$

Since it's a transverse wave it exists a cartesian system so that:

$$S = \{\boldsymbol{E}(\boldsymbol{x}, t) + \boldsymbol{B}(\boldsymbol{y}, t)\}$$

We can also simplify the EM wave formula for monochromatic light using Steinmetz notation:

$$\boldsymbol{E}(\boldsymbol{r},t) = Re\left[\widetilde{\boldsymbol{E}}(\boldsymbol{r})e^{j\omega t}\right] \qquad \boldsymbol{H}(\boldsymbol{r},t) = Re\left[\widetilde{\boldsymbol{H}}(\boldsymbol{r})e^{-j\omega t}\right]$$

Where $\widetilde{\boldsymbol{E}}$ and $\widetilde{\boldsymbol{H}}$ are complex vectors.

Steinmetz notation results particularly useful since we can now describe a broadband light as an overlapping of multiple distinct monochromatic lights:

$$\widetilde{\boldsymbol{E}}(\boldsymbol{r}) = \sum_i a_i(\boldsymbol{r})e^{j\,\omega_i t}$$

A representation of light composed by two components rotating during propagation is given in figure 2.1.

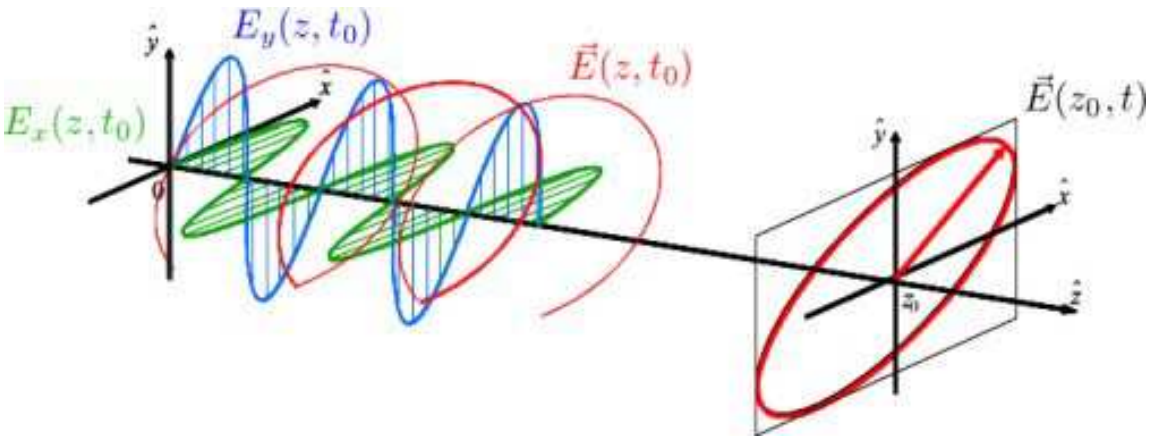

Figure 2.1: vectorial representation of a monochromatic plane wave.

As we said in chapter 1 the main feature of OCT technologies is the ability to keep track of the backscattered power. It's then important to give a definition of intensity.

Intensity of a EM wave is the average quantity of energy that passes through an unitary area orientated in a perpendicular manner with respect of the direction of propagation of the light within one second. Using a more mathematical description we can define intensity as:

$$I \propto \langle|\boldsymbol{E}|^2\rangle$$

Now we can apply Steinmetz notation to archive:

$$\langle|\boldsymbol{E}|^2\rangle = \frac{1}{4}\langle|\widetilde{\boldsymbol{E}}|^2(\boldsymbol{r})e^{-2j\omega t} + |\widetilde{\boldsymbol{E}^*}|^2(\boldsymbol{r})e^{2j\omega t} + 2\,|\widetilde{\boldsymbol{E}}|\cdot|\widetilde{\boldsymbol{E}^*}|\rangle$$

If we consider a averaging time larger than T where T is the period the electric field we can ignore the probabilistic side of the equation and obtain a constant value for $\langle|\boldsymbol{E}|^2\rangle$:

$$\langle|\boldsymbol{E}|^2\rangle = \frac{1}{2}|\widetilde{\boldsymbol{E}}|\cdot|\widetilde{\boldsymbol{E}^*}| = constant$$

2.2 Interference

Interference is a physical phenomenon typical of waves that happens when multiple waves of same frequencies overlaps in the same spatial region. Since light is a EM wave it's also subject to this phenomena. We will quickly cover the basic since it's a key mechanism required to produce the signals that OCTs use to produce images.

2.2.1 Monochromatic light

As we know interference happens when waves have the same frequencies. Since in our contest we are using light in a specific region of space at a specific time t_1, the condition for the interference is to have same wavelength λ.

Now we suppose that in a specific region there are two electric fields $\boldsymbol{E}_1$ and $\boldsymbol{E}_2$ that propagate along the same direction $\hat{z}$ and with the same λ so that:

$$\boldsymbol{E}_1(\boldsymbol{r},t) = Re\left[\widetilde{\boldsymbol{E}_1}(\boldsymbol{r})e^{j\omega t}\right]$$

$$\boldsymbol{E}_2(\boldsymbol{r},t) = Re\left[\widetilde{\boldsymbol{E}_2}(\boldsymbol{r})e^{j\omega t}\right]$$

With:

$$\widetilde{\boldsymbol{E}_i}(\boldsymbol{r}) = a_i e^{j(\boldsymbol{k}\cdot\boldsymbol{r}-\delta_i)} \qquad i = 1,2.$$

Where $|\boldsymbol{k}| = \frac{2\pi}{\lambda}$ and δ_i is the initial phase of the field when it started propagating. For our interest we can assume $\delta_i = 0$. We can also ignore the time dependence of the light if we assume their sources are statics.

In this scenario if we try to measure the intensity of the light in the overlap area we find[6]:

$$I = I_1 + I_2 + J_{12} \propto \langle \boldsymbol{E}_1{}^2 \rangle + \langle \boldsymbol{E}_1{}^2 \rangle + 2\langle \boldsymbol{E}_1 \cdot \boldsymbol{E}_2 \rangle$$

The third term is the so called interference term and in the simplest case in which both fields are polarized along $\hat{x}$ we can write:

$$I = I_1 + I_2 + 2\sqrt{I_1 I_2}cos\delta$$

Where $\delta = \Delta z \ \frac{2\pi}{\lambda}$ the phase difference due to the different paths.

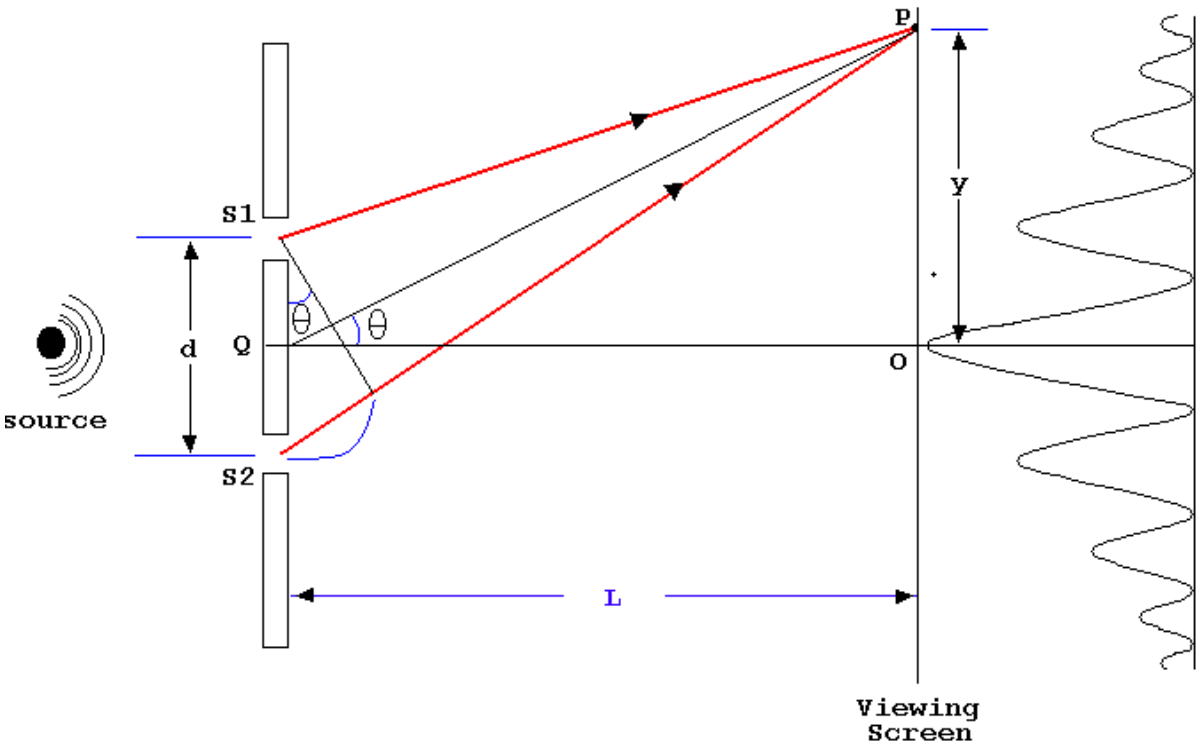

Figure 2.2: we now see the interference pattern of two identical point sources. The amplitude at maximum at point O since there is no path difference hence cosδ is 1 as we move away the term decreases to then increase once again. It is not a cosine due to the fact that as the path increases some of the light is absorbed along the path.

2.2.2 Coherence length and coherence time

As we already said interference happens when light with same frequencies interact. Hence if we have purely monochromatic light source and using it as in Figure 2.2 to produce two identical point sources then we would have interference at every point $\boldsymbol{r}$ located after the slits s_1 and s_2. In practice this is not the case[6'] since we never have a truly monochromatic source, but we are bound to have some bandwidth due to the Heisenberg principle:

$$\Delta\lambda \cdot \Delta E \geq \frac{h}{4\pi}$$

If we use the two slit method on a real source we will see that the interference fringes start to fade as the $\Delta\boldsymbol{r}$ start to increase. On a Viewing Screen (we refer to Figure 2.2) we would observe that in a range $[d, -d]$ around the point O we have the formation of an interference image. Outside this interval the resulting I is given simply by the sum of the intensity coming from the slits.

From this results we can deduce that in the points on the screen in which there is no interference the light coming from s_1 and s_2 are no longer coherent. Only the optical path difference $\Delta\boldsymbol{r}$ changes between the regions. So we can define the concept of coherence length.

Coherence length of a light source is the maximum path difference that rays from the source can have in order to produce interference. The coherence length is inversely proportional to the bandwidth of the source[6].

We can easily confirm this by thinking about a simple lightbulb and how it never produce an interference image.

The path difference is not truly the reason for which we lose coherence but it's a derived parameter from the Coherence time.

If we use a beam splitter to produce two beams, that will interfere on a screen after introducing path difference within the coherence length. The two paths introduce a delay of $\Delta\tau$. If the increases the delay bay changing the refractive indexes we will reach a $\Delta\tau$ for which the interference will no longer appear.

Coherence time of a source is due to the Heisenberg uncertainty principle and is determined by the average time τ with which the material of the source produces photons[6]. It's an intrinsic phenomena due to uncertainty of the transition of electrons between bands in terms of energy of the photons and time of realise. For this reason coherence time is unavoidable in real light sources an coherence length is a by-product due to propagation delays.

2.2.3 Michelson interferometer

Michelson interferometer is one of the most common configurations in interferometry.
The setup consist in a light beam impinging on a beam-splitter (BS). The two emerging beams then go through different path until they overlap on a screen. A typical Michelson scheme is in Figure 2.3.

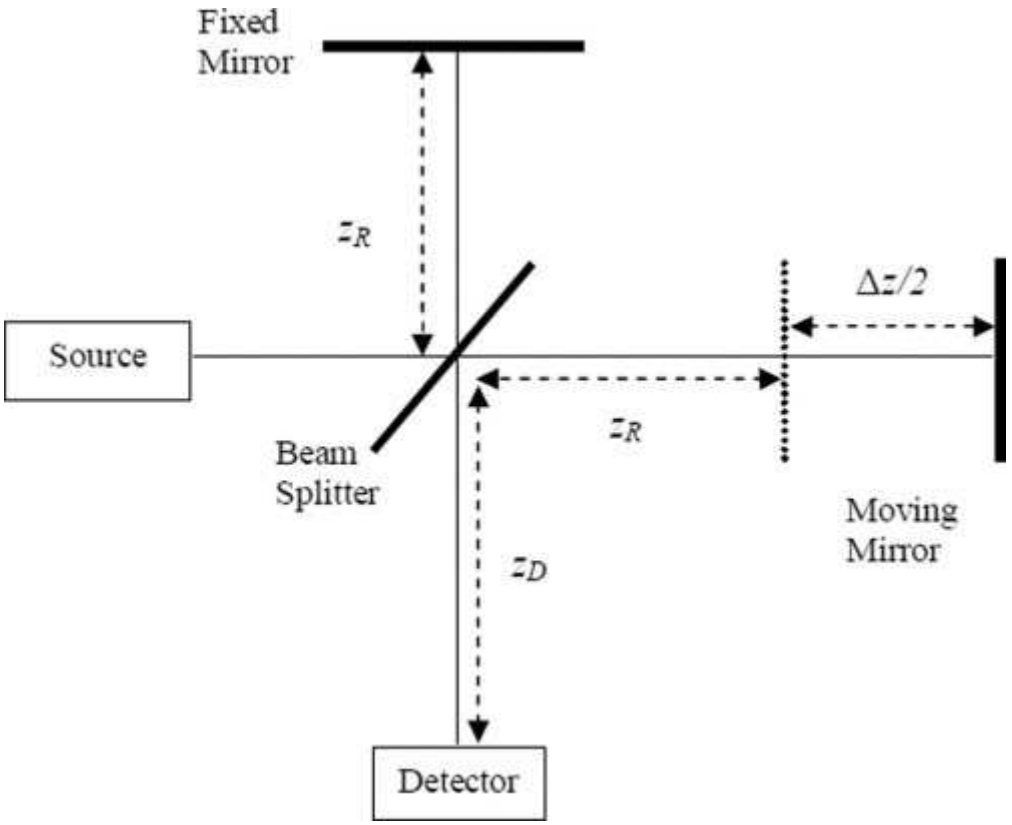

Figure 2.3: Schematic of typical Michelson configuration

Michelson interferometer are typically equipped with moving parts to control the coherence length of the two beams[6].
We are able to track the path difference by measuring the intensity at the centre of the screen and evaluating how the interference component changes in function of the path length.

2.2.4 Fringe visibility

For monochromatic fields interfering we can define a new parameter called fringe visibility or simply visibility. It's defined as[6']:

$$v = \frac{I_{max} - I_{min}}{I_{max} + I_{min}}$$

We can immediately notice that if $I_i = I_j$ then $I_{max} = 0$ resulting in $v = 1$.

Despite in theory visibility is a constant in reality it is time or space dependent. This is due to the probabilistic nature of the photon emitting process that introduce a broadening of the emitted bandwidth and as we saw causes the existence of coherence times (τ_c).

If we split the light coming from a real "monochromatic" source and then we overlap the two beams in a way that the light of the first beam arrives in the interference region at time t while the light of the second beam arrive in the area at time $t + \tau$. We can then define the visibility in function of τ and we observe that the visibility is an exponentially decaying function with:

$$v(\tau_c) = \frac{1}{e}$$

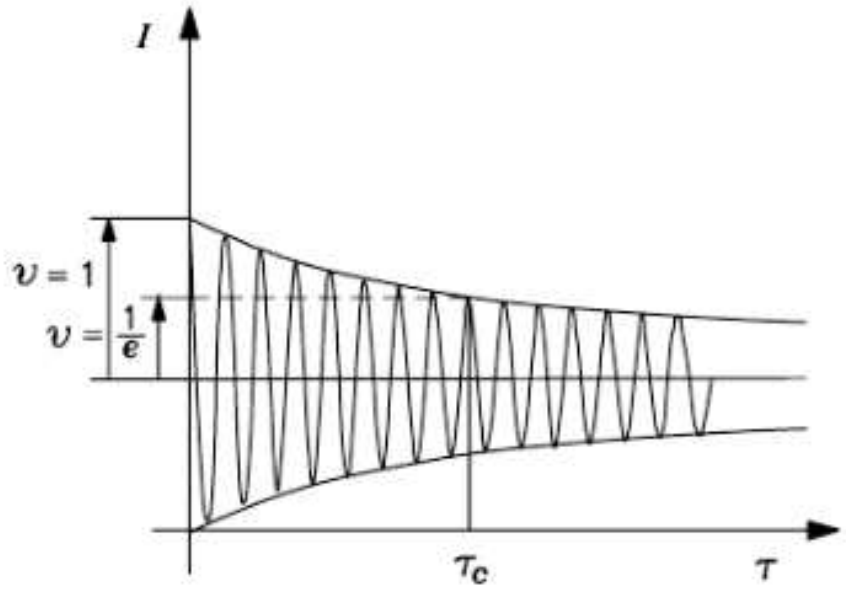

Figure 2.4: effect of how the intensity at the output of a Michelson interferometer changes as a function of τ.

From the results we can conceive τ_c as a time slot. After each time slot some property of the source have changed due to the stochastic nature of the emitting process. Since every τ_c time the source has changed we have losses in the coherence of light emitted at different times.

In a ideal monochromatic source with would have $\tau_c = \infty$ resulting in perfect visibility of the fringes no mater the time delay between the interacting lights.

2.2.5 Coherence function

The coherence function is a measure of coherence for broadband sources. For these sources it could happen that only a certain percentage of the light coming from two broadbands sources will interfere.

An easy scenario where not all the light interfere, is given by two sources with partially overlapping bandwidths. In this case only the common frequencies have the capability to interfere. To address the problem of evaluating how prevalent the interference phenomena is between two generic field it has been formulated the mutual coherence function defined as[6]:

$$\Gamma_{ij}(\tau) = \langle \boldsymbol{E}_i(t+\tau)\boldsymbol{E}_j^*(t)\rangle$$

In the case $\boldsymbol{E}_i = \boldsymbol{E}_j$ it's called self-coherence function Γ_{ii}. If then $\tau = 0$ the self-coherence is reduced to the field intensity:

$$\Gamma_{ij}(0) = I_i$$

Our definition of coherence function despite being correct we will usually find it in its normalised form:

$$\gamma_{ij}(\tau) = \frac{\Gamma_{ij}(\tau)}{\sqrt{\Gamma_{ii}(0)}\sqrt{\Gamma_{jj}(0)}}$$

Where the main advantage of this notation is the direct one to one correspondence between the percentage of interfering light and the normalized form. Knowing this correlation we can easily make three observations:

- $|\gamma_{ij}(\tau)| = 0$ completely incoherent fields; no interference fringes.
- $|\gamma_{ij}(\tau)| = 1$ completely coherent fields; total field has the interference therm.
- $0 < |\gamma_{ij}(\tau)| < 1$ partially coherent fields; there are visible fringes and the visibility is given by:

$$v = \frac{\sqrt{I_i I_j}}{I_i + I_j}|\gamma_{ij}|$$

The normalized notation is also useful since it gives us information also on how the interference shapes the total intensity in the regions were the two field overlaps. The total intensity can be rewritten using the normalized coherence function as follow:

$$I = I_i + I_j + 2\sqrt{I_i I_j}|\gamma_{ij}(\tau)|\cos\left(\delta + |\gamma_{ij}\right)$$

Last important feature of coherence functions is the possibility to recover the coherence time τ_c. τ_c is defined as the full-width-half-maximum (FWHM) of the self-coherence function of the source.

$$\tau_c = |\gamma_{ii}(\tau)| = \frac{|\gamma_{ii}(0)|}{2}$$

To end this the coherence function of a source is determined by its power spectral density (PSD) since the Winer-Khintchine theorem states that for random process the Fourier transform of the autocorrelation function is proportional to its PSD.

2.3 Time Domain OCT (TD-OCT)

Time domain OCT is the first OCT technology [23]. It's setup is similar to the Michelson's. We have a source how's beam is split along two paths.

The first path is called Sample arm that guide a beam to a sample we want to measure. After the interaction with the sample occurs the back-scattered light is guided to the photodetector where the interference will take place.

The second path is called Reference arm. Here the light is guided to a movable mirror and back to the photodiode.

A simple TD-OCT obtained from a Michelson interferometer is given in Figure 2.5.

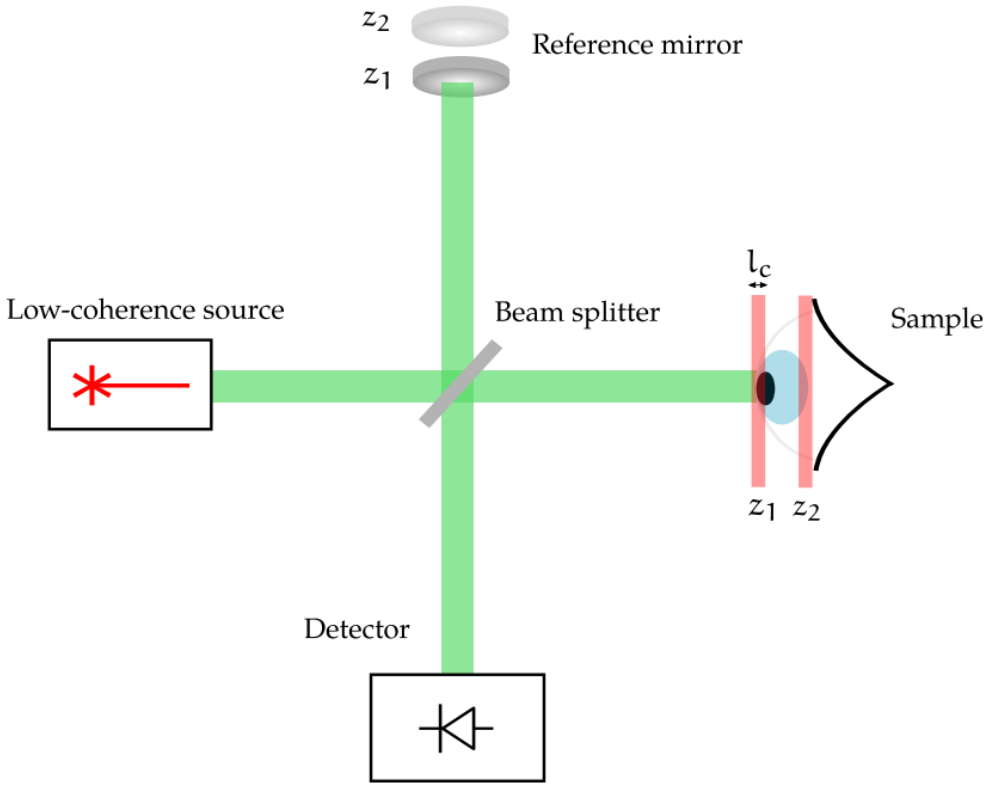

Figure 2.5: Schematics of simple TD-OCT

The general idea is to recover information from the interference about the reflectivity of the sample at different points.

To explain how we recover these info we will observe the case in which our sample is a mirror. We are in a scenario like in Figure 2.3. if the path difference between reference and sample (Δz) is larger than the coherence length l_c we have no interference, hence a flat line at the output of the photo detector. If instead $\Delta z < l_c$ we will have interference[22]. From these observation we understand that if we send a continuous beam from our source while we move the reference mirror in an interval such that the $\Delta z \in [-l_c - a, b + l_c]$ we can plot the signal produced by the photodiode in function of Δz and produce an A-scan with the form in Figure 2.6.

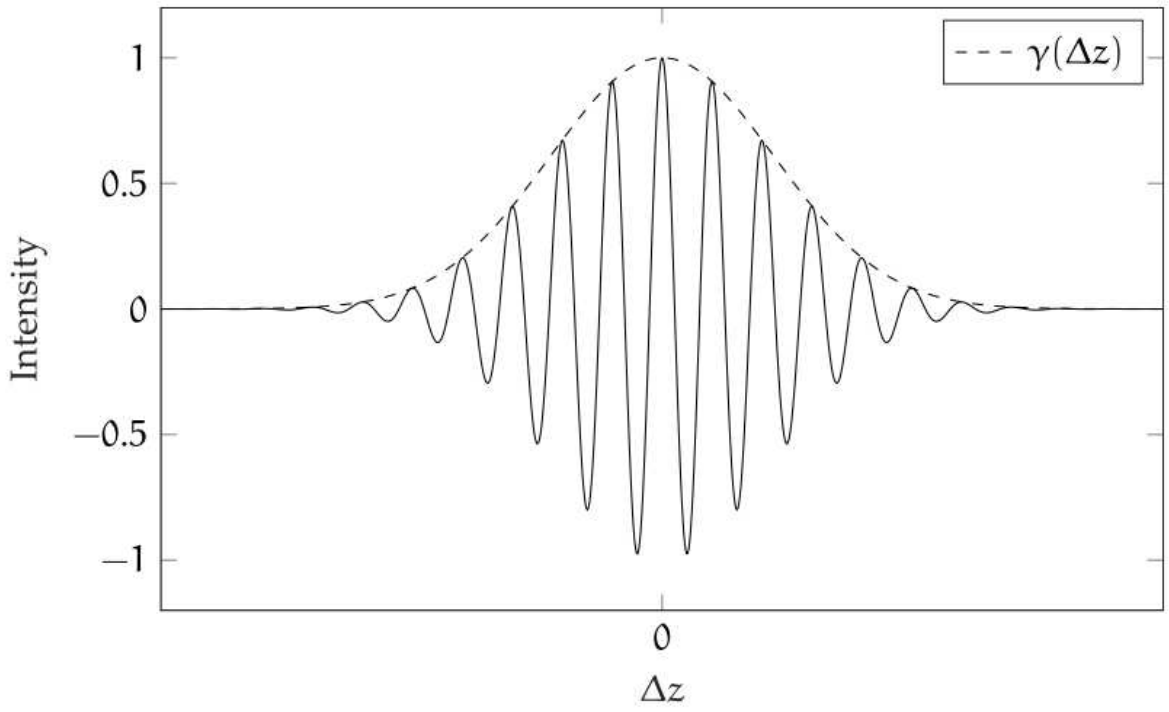

Figure 2.6: A-scan of TD-OCT with a mirror as sample

As we can see we initially have no interference until $\Delta z = -l_c$ we have no interference. As Δz goes to 0 we have the peak interference for it to decrease as Δz grows. the signal is a sinusoid enveloped by the coherence function $\gamma(\Delta z) \cdot \rho$ where ρ is the reflectivity of the mirror. If the arms are balanced we can change the horizontal axes with an axes reporting the mirror shift from 0 onward; by doing so we can locate the position of the mirror by looking at the location of the maximum interference.

If we have multiple semi-transmitting mirrors we would see multiple envelops each corresponding to a mirror. By mapping multiple A-scans into grayscales based on the

received intensity we can obtain an image (B-scan) of the region scanned by the reference moving mirror.

It's evident the resolution of the image is dependent on l_c since reflectors located closer from each other than l_c would not be distinguishable. Time domain OCT is also called low coherency OCT since low coherence high bandwidth sources are the most desirable due to higher resolution images[17].

The consideration made for an array of mirror are translatable to a generic sample since we can conceive the sample as composed by multiple discrete reflectors[8].

The scheme in figure 2.5 while theoretically work and ideal for explaining the way TD-OCT work it's unpractical. Modern TD-OCT use fibers to guide the beams and a fiber coupler instead of BS in order to reduce alignment problems. Also lens are used in order to direct and collect backscattered light more effectively. A piezoelectric transducer (PZT) is used to modulate the frequency of the incoming light in order to shift the distance range visible by the photodiode.

This configuration has been introduced by Fujimoto in 1986 and is called optical ranging[19].

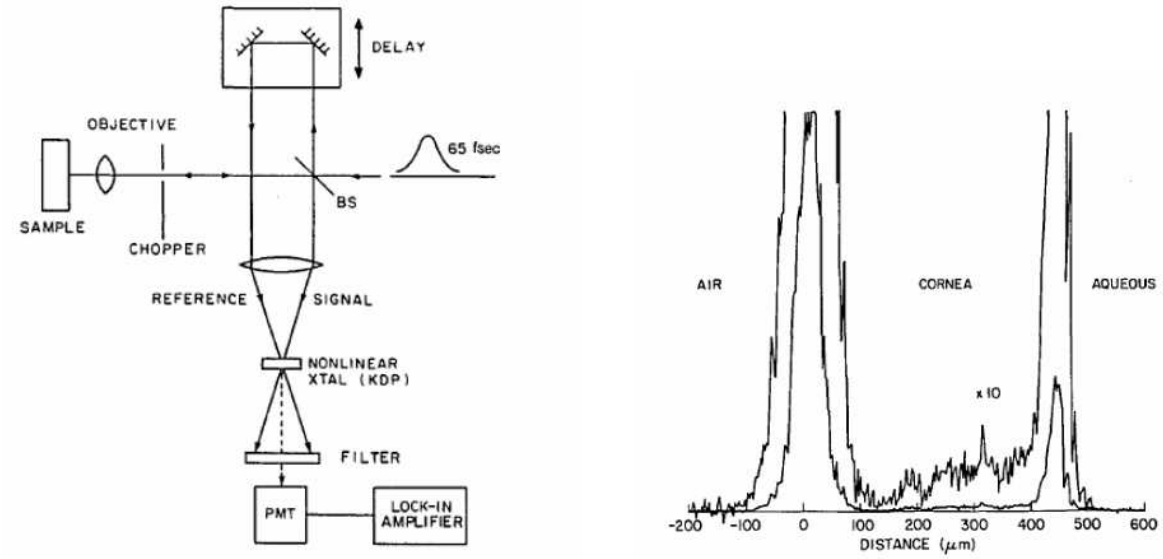

(a) Optical ranging setup (b) Rabbit cornea.

Figure 2.7: a)Fujimoto original set up b)A-scan of TD-OCT of a rabbit cornea

In figure 2.7 we have an example of an A-scan obtained by optical ranging.
The main peaks corresponds to the interfaces between two different materials. The first interface is air-cornea and the second is cornea-aqueous. In the air and aqueous we have basically no back reflection while in the cornea we do. If we want to map the A-scan onto a grey scale; the image would be a grey stripe(cornea) bordered by white lines where the separation surfaces are located.
By combining multiple greyscale A-scan we obtain a B-scan representing a cornea. The image is useful for thickness and curvature measurements in order to diagnose possible defects.
The main problem of TD-OCT is the long acquisition times required in order to produce the A-scans. This means that in vivo sample are difficult to image since movement during the acquisition will deform the image[17].
For this reason TD-OCT have been largely abandoned in favour of FD-OCT a newer technology much faster and with better resolutions.

2.4 Fourier Domain OCT (FD-OCT)

Fourier domain OCT is a class of OCT techniques that encode the information relative to dept and reflectivity in the frequency response of the output signal.
The main advantage of these techniques is the high acquisition speed of the A-scans. Due to the new encoding of information there is no longer need for a moving mirror in the reference arm. The reduction of mechanical parts required to scan a sample lead to quicker acquisition times and a reduction in distortion due to vibration of the moving components[4].
Drawbacks of FD-OCT is the requirement of much more sophisticated light sources and the requirement of post processing of the signal in order to remove aberration due to the optical equipment and high speed ADCs. FD-OCT also require more elaborated schemes resulting in higher cost for the setup.
The main two categories are spectral domain OCT and swept-source OCT.

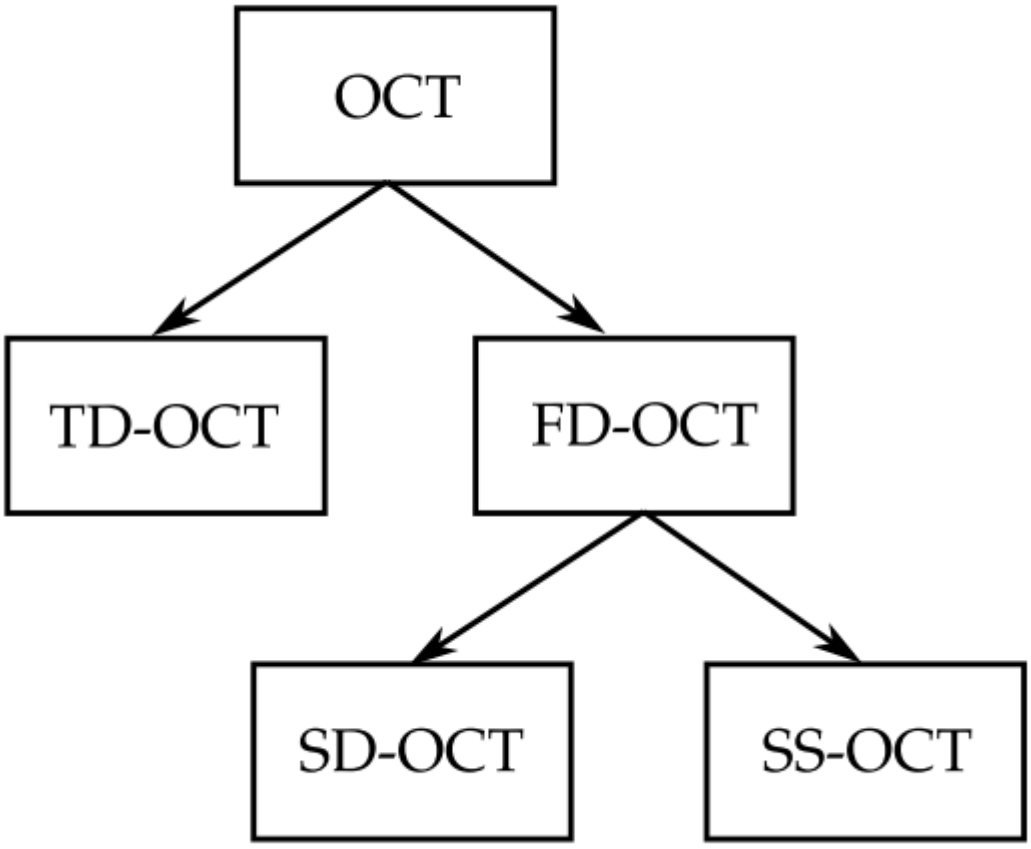

Figure 2.8: Diagram of FD-OCT classes

2.4.1 Spectral Domain OCT (SD-OCT)

First among the FD-OCT techniques was introduced in 2002 by Wojkowski[21]. His original scheme for SD-OCT used a Michelson interferometer using a Super luminescent diode (SLD) as a broadband source. Wojkowki set up also substituted the screen with a combination of a reflection grating and complementary metal-oxide semiconductor (CMOS) camera. This combination uses the grating to spatially separate the various wavelength in order to quire the spectral intensity of the interference with the camera[21].

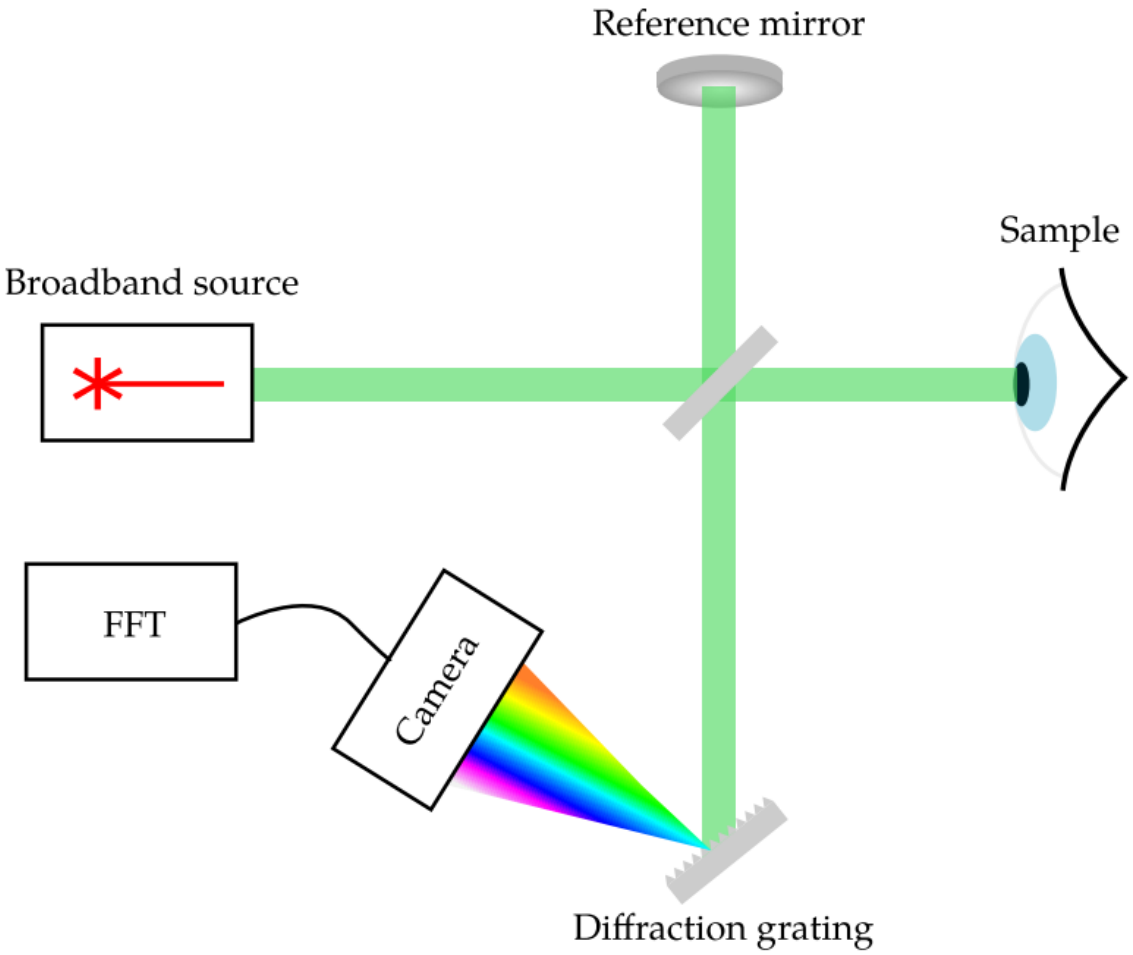

Figure 2.9:rappresentation of Wojkowaski set up

After the acquisition of the A-scan it's require post processing for evaluating the Fourier transform and other filtering operations making the use of fast GPU essential.

We know from the TD-OCT that the intensity of the interfering beams follows

$$I(\Delta z) \propto |\rho_s|^2|E|^2 + |\rho_r|^2|E|^2 + |\rho_s\rho_r|^2|E|^2|\gamma(\Delta z)| \cos\left(\frac{2\pi}{\lambda}\Delta z\right)$$

And it can be rewritten in function of $k = \frac{2\pi}{\lambda}$ as:

$$I(k) \propto I_{source}(k) \cos(k\Delta z)$$

As we can immediately notice the spectral intensity is no longer dependent on Δz, that used to vary in time with TD-OCT, but now dependent on k. Thanks to the camera-grating combination we are able to obtain immediately the spectral intensity of a broadband signal. Now if we consider a reflector in position $d = \Delta z/2$ it will modulate the intensity of the spectrum dependent on d.

In the figure below we see how two reflectors located at $d_1 = \frac{\Delta z}{2} = 12.5\ \mu m$ and $d_2 = \Delta z = 25\ \mu m$ affect the spectrum of a broadband source wit central wavelength 1310 nm.

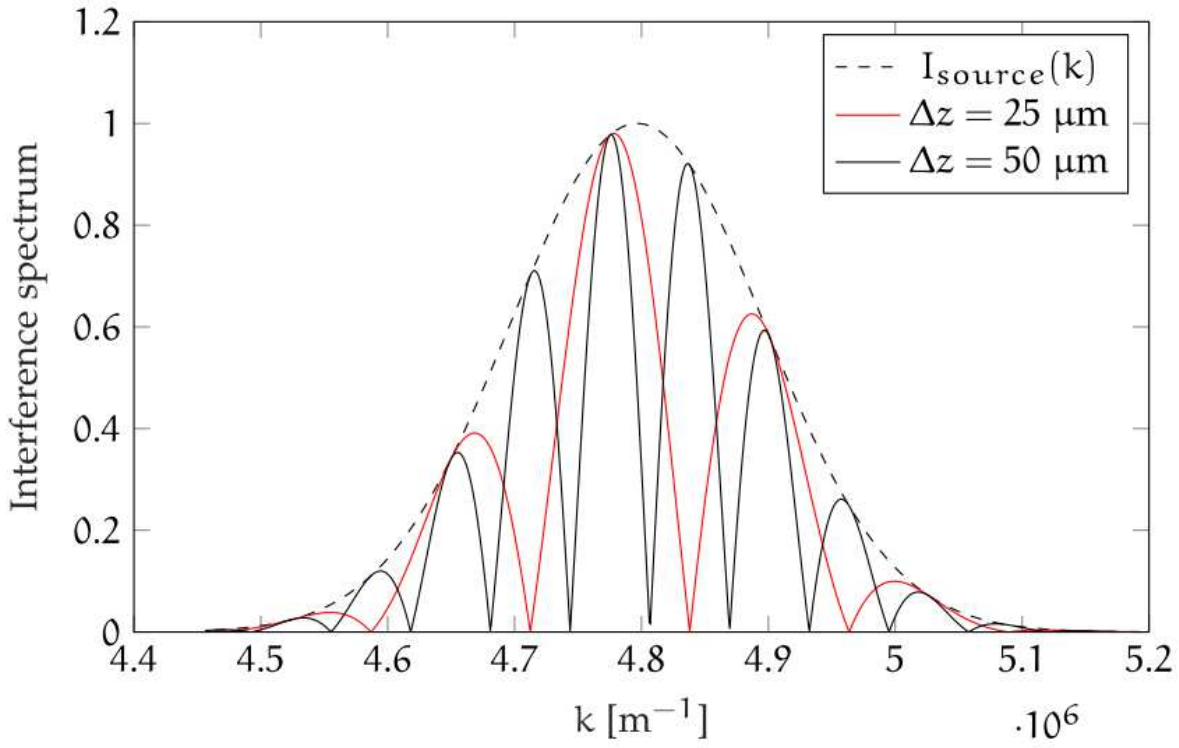

Figure 2.9:SD-OCT A-scan modulated by two reflectors

Once we capture the A-scan (a power spectral density of the interference). we have to compute the Fourier transform to change the abscissa axe from k to position d.
The depth of the reflectors is encoded in the modulation frequency in the spectrum while the reflectivity is encoded into the fringe visibility.
By using the Fourier transform we will see two different peaks located at distance $\frac{d_1}{2}$ and at distance $\frac{d_2}{2}$.
It's important to notice that in SD-OCT the role of the coherence function is completely different from TD-OCT. With this architecture we are capable to detect something at depth only if $\gamma(d/2) \neq 0$. This lead to a necessity for highly coherent sources in order to map significant regions of space.

2.4.1.1 Drawbacks of FD-OCT.

SAMPLING DISTORTION: the spectrum is usually detected linearly in the wavelength domain. This introduce a distortion after the Fourier transform to map the signal into distance. Grating reflect different wavelength at different angle also based on the angle between the normal to the grating and the impinging angle following the formula[10]:

$$\sin\beta = \frac{m\lambda}{\Lambda} + \sin\alpha$$

Where Λ is the distance between the grating lines, α is the impinging angle and m is the refraction order.
This means that we are require to resample the spectrum in order to not chirp the signal in after applying the Fourier transform.
In Figure 2.10 we can see that having linearly sampled (back lines) the signal it's transform will be affected by broadening reducing the resolution of the images.
So if we pre-chirp the spectral intensity before the FFT (red line) we are able to remove the broadening and hence improve resolution.

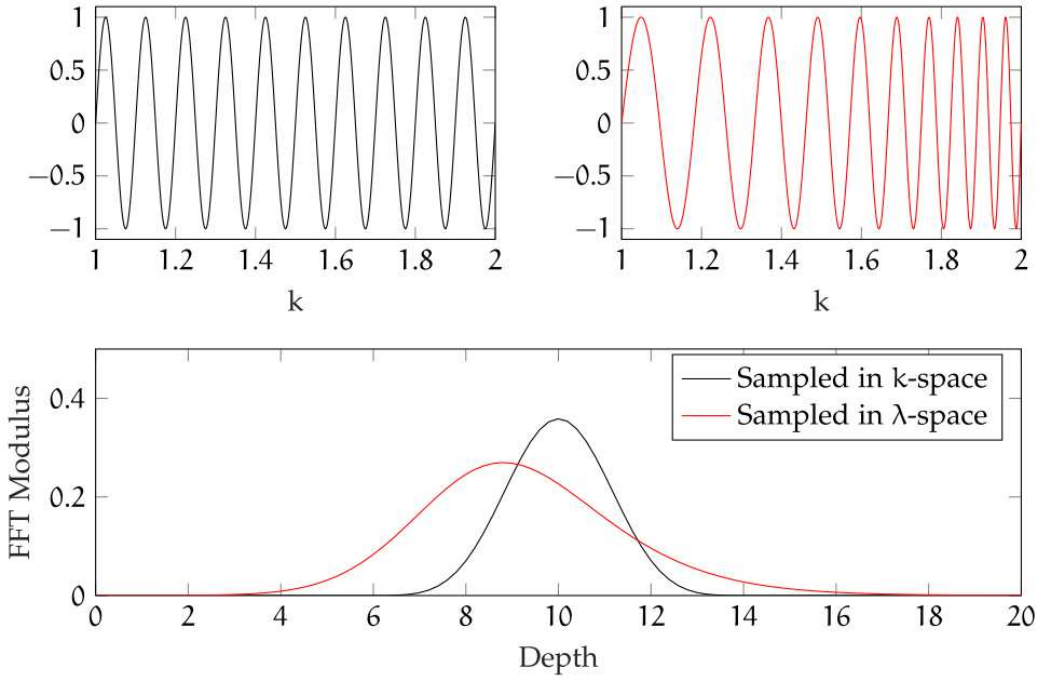

Figure 2.10: example of the chirp introduced by sampling distortions.

SENSITIVITY FALLOFF: the sensitivity is defined as the signal to noise ratio when we sample an ideal reflector.

For increasing depth we find a decrease in sensitivity this is due to the increase in optical path difference for higher frequency hence since Δz is growing we will find lower value of $\gamma(\Delta z)$ resulting in a dampening of visibility fringes. This problem can be further amplified if we locate the reflector in such a way that the interference signal is separated by the grating in such a way that parts of the PSD function are under sampled since parts of the light impinges outside the sensing region[10].

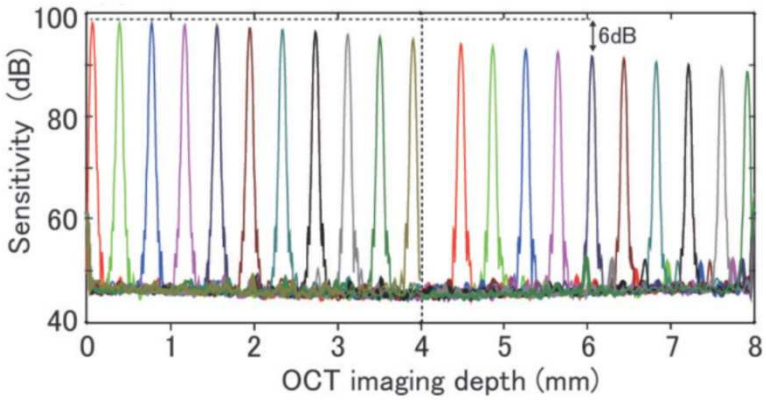

Figure 2.11: shows how the sensitivity drops as we push the reflector further away.

IMMAGING ARTEFACTS: As we already know in SD-OCT we shine a broadband light onto the sample and then we acquire the spectral response of the echoes of light coming from all the point of the sample.
Although receiving information from all point of the sample drastically reduces the time require to acquire A-scan it also causes the introduction of artefacts due to the interaction between lights from different reflectors and also from the Fourier transform property.

The first artefact we will talk about are ***mirror artefacts.*** These artefacts are due to the property of Fourier for which the transform of a real signal is an Hermitian one. Our camera typically registers the power spectral density using real numbers. After the transform we will find Hermitian complex signals. Our images are typically obtained from the modulus of intensity of $I(d)$ function; if we directly map into grayscale the A-scans we would create symmetrical images. The easiest solution is to remove the negative distances from the A-scans before computing the image. While this is a solution to no longer have a mirrored image; it does not remove our problem.
First if we have a reflector really close to $\Delta z = 0$ since the width of the peaks is proportional to the coherence function of the source we could have parts of the mirror artefacts creep into the image. also if there are optical paths differences in length it is possible to have $\Delta z < 0$ that actually contain information if the reference path is longer. In this last case it's possible that by moving closer to the reflectors we could have mirror images fully entering the image[16]. the solution to this problem is to accurately choose the position of the sample.

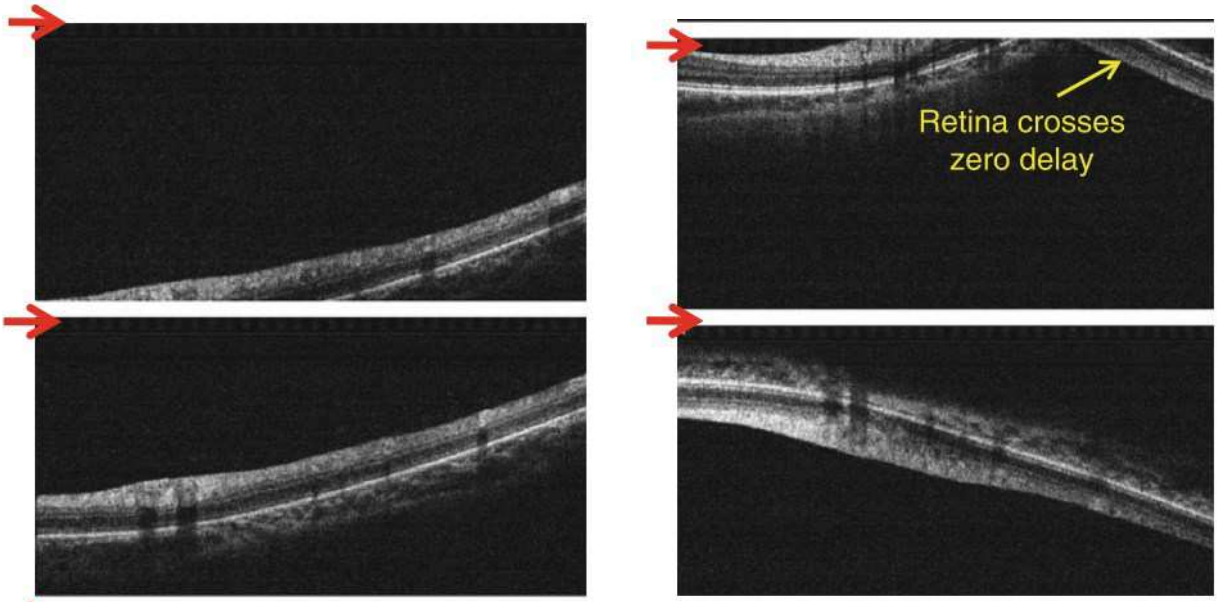

Figure 2.12: example of mirror artefact due to moving the cornea too close to the $\Delta z = 0$

Other artifacts are due to the interaction between the various back scattered lights. Now looking at the transform of the interference we see[18]:

$$I(d) = \frac{\rho}{8}\gamma(z)[R_R + R_{S1} + R_{S2} + \cdots] +$$

$$+\frac{\rho}{4}\sum_{n=1}^{N}\sqrt{R_R R_{Sn}}\left[\gamma[2(z_R - z_{Sn})] + \gamma[-2(z_R - z_{Sn})]\right] +$$

$$+\frac{\rho}{8}\sum_{n\neq m=1}^{N}\sqrt{R_{Sm}R_{Sn}}\left[\gamma[2(z_{Sm} - z_{Sn})] + \gamma[-2(z_{Sm} - z_{Sn})]\right]$$

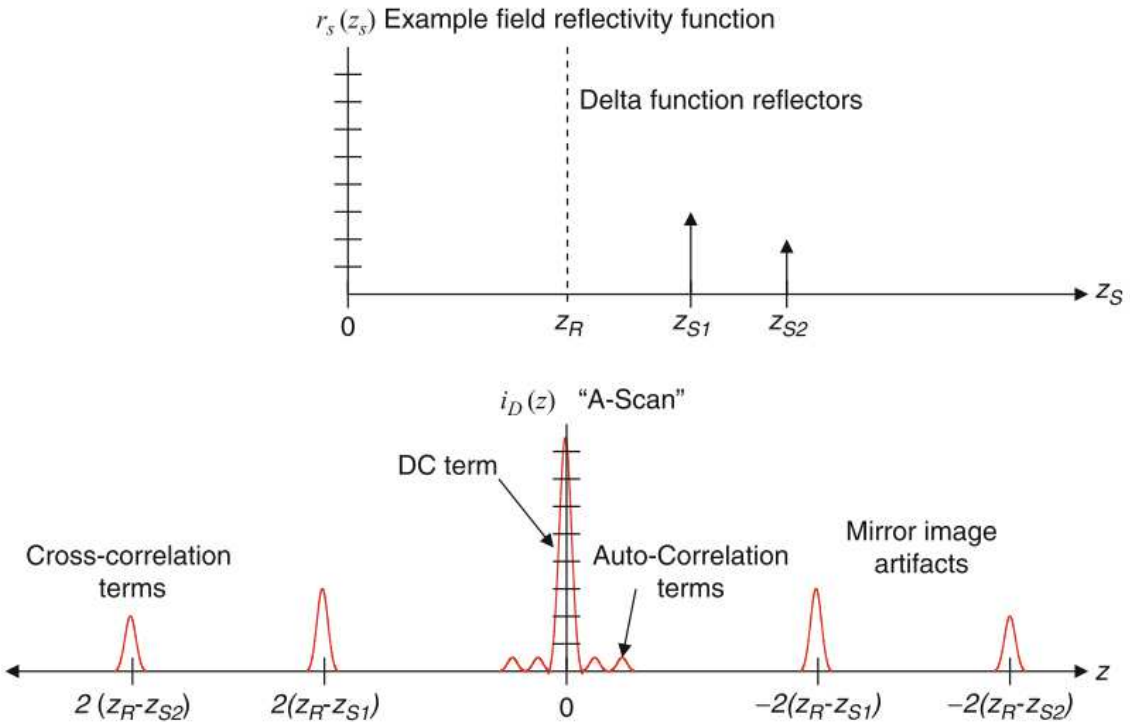

Figure 2.13: example of the Fourier transform obtained from the interference between two reflectors. Here are put into evidence the various components of the interference.

Taking a look to the example in figure 2.13 we can immediately recognize the negative semi-plain containing the mirror artefacts that we talked earlier.

After this immediate acknowledgement we can start talking about the tree terms[18]:

- **DC Component**: represented by the first term, it's a scaled version of the coherence function of the light source used. It's by far the largest component in term of intensity and it's located at the point of 0 optical path difference. It corresponds to the non-interfering light in the Michelson interferometer and receives contribute from all the reflectors. It can be remove by ignoring the region while creating an image since the peak will generate a blind spot to actual reflectors anyway.

- **Cross-correlation**: is the second term and arises from the interference between the reference signal R_R and each of the copies generated by the reflectors. As we know each reflector generates a copy of the reference signal with intensity $\sqrt{R_R R_{Sn}}$ which is then modulated by $e^{j2(z_R - z_{Sn})}$ on the power spectral density. Once we do the Fourier transform the modulation of the copy will be transformed into a shift in space of $z_R - z_{Sn}$ due to the transform property. The shape of the peak is one again define by the coherence function. The corelation function is the most important term on of the interference since the position of its peaks corresponds to that of the reflectors and their intensity is proportional to the reflectivity.

- **Auto-correlation**: similarly to its predecessor it's generated from the interference due to the replicas of the reference signal. The main difference is that this term includes the interferences between the copies whit each other. It usually appear as little peaks since their heigh is proportional to $\sqrt{R_{Sm} R_{Sn}}$ where the two amplitudes are typically smalls so they tend to not be visible. They are located at positions such that $\Delta z = |z_{Sn} - z_{Sm}|$. Usually this component does not require to be filtered since the reflectors have typically low reflectivity and the reflectors tend to be very close to each other meaning that most of these peaks falls in the blind spot of the DC component.

2.4.2 Swept-Source OCT (SS-OCT).

The invention of tuneable laser capable to emit narrowband beams within a wide range of wavelength as allowed a further improvement in the FD-OCT technology.
We had the introduction of Swept-Source OCT SS-OCT. compared to its predecessor SD-OCT we have substituted the wideband source with a new generation source cable to produce light in a cyclical sweep. This means that our source output behaves in time as:

$$f(t) = f_0 + \delta_f \cdot t$$

For $t \in [0, T]$ where T is the period of the source and δ_f is the so called sweep speed and allows for the frequency to change linearly within each period.
The main advantage of this configuration is that we no longer require gratings and photodetectors array in order to capture the spectral density of the echoes. SS-OCT is capable to use a single photodetector to capture the whole spectrum if we take the measurement of intensity at different times within a timeslot of dimension T.
This means that we can write the intensity at the photodetector as[15]:

$$I(t) = I_1 + I_2 + 2\sqrt{I_1 I_2}\cos(2\pi\Delta f t)$$

Where

$$\Delta f = \Delta t \cdot \delta_f = \delta_f \cdot \frac{\Delta z}{c} = \delta_f \cdot \frac{d}{2c}$$

By sampling at the appropriate times we can have $I(k)$ exactly as we had with SD-OCTs; but without the grating and photodiode array combo. We have eliminated the problem coming from sensitivity fall off and also reduced the complexity of the system in term of elements components and alignment problems arising when we have in air sections.

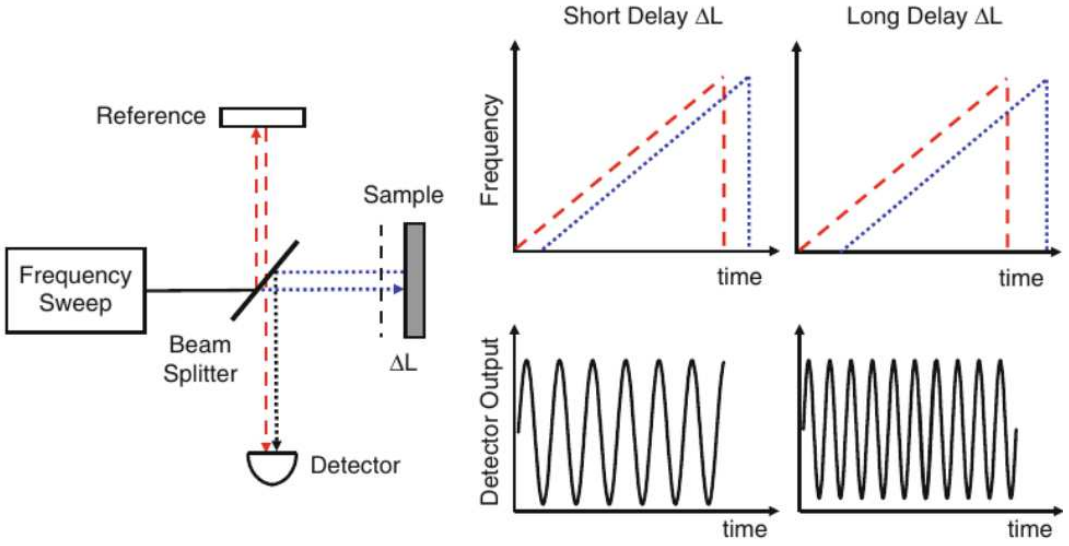

Figure 2.14: SS-oct scheme and plots of source frequency and output frequency with time on the first row while we have the detector outputs on the second row.

2.4.2.1 Drawbacks

NON-LINEAR SWEEP: typical frequency sweep sources are composed by lasers using an active material (usually semiconductor optical amplifier SOA capable of amplify a wide range of frequencies), enclosed inside a resonance cavity that can be manipulated in order to change the central wavelength of the output signal.
An example of these type of sources is a Fabry-Perot resonance cavity in which the mirror position can be controlled by changing the tension at the edge of the mirror. Increasing the tension the mirror distance themselves changing which frequencies can interfere constructively and hence selecting a new output signal.

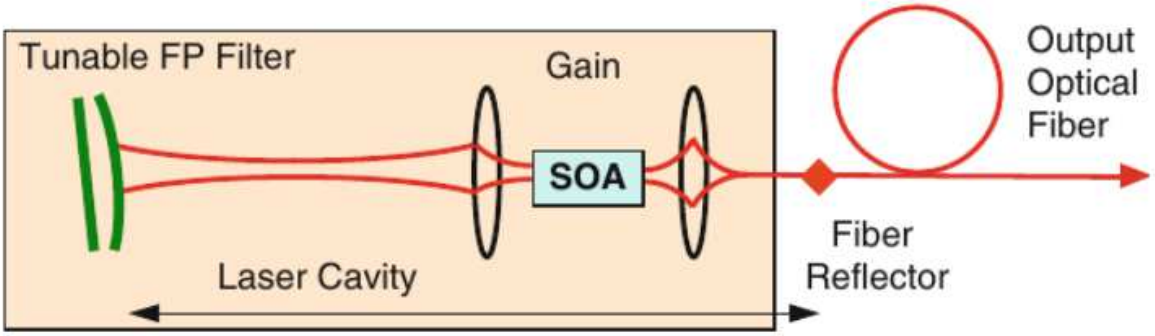

Figure 2.15: SS-oct Fabry-Perot sweep source

The problem of this type of configuration is that the mirror that compose the filter do not change instantly position. Also when we change the selected wavelength we are engaging different energy levels in the material. this mean that there is a transitory time in which we have to change the population of the levels in the active material[15]. These two mechanisms introduce non-linearities in the frequency sweep that becomes:

$$f(t) = f_0 + \delta_f \cdot t + \eta(t)$$

Where $\eta(t)$ is the nonlinearity introduced. In order to fix the effects of nonlinearity it's required to do some post processing as in SD-OCT.
As an alternative in SS-OCT we can remove the requirement of post processing by introducing an hardware solution to the source. This option is the K-clock a sinusoidal signal of variable frequency generated by an unbalance Mach-Zehnder interferometer using part of the source output to detect the nonlinearities. K-clock is used to pilot the DAQ in order to correctly pick the sampling times.

ACQUISITION RATE: in SD-OCT the acquisition rate was completely defined by the specifics of the camera used. Even if SS-OCT are much faster than their predecessor since we have typical A-scan acquisition rate in the order od 100,000 per seconds it is now necessary to accurately evaluate the characteristics of the source in order to determine the correct acquisition rate. The reason why we no longer can make a measurement at whatever frequency our photodetector can sustain is the same we talked on the non-linearities. The active material need some time in order to build up the population at the new energy levels in order to sustain spontaneous emission. When we are introducing a small change in the selected wavelength the "inertia" of the active material manifests as nonlinearities in the sweep.

When we have to restart the cycle for a new sweep we have a long transient time to wait in order for the stimulated emission to be sustained. This means that at every cycle we have to wait some time before starting the acquisition of a new A-scan.

Still even with this new challenge with SS-OCT we have acquisition speeds per A-scans much faster than SD-OCT making SS-OCT the standard for in vivo imaging.

IMMAGING RANGE: As in SD-OCT the imaging range is dependant on the coherence length of the source. We can recall that the coherence length is defined by the optical path distance at which the visibility of the fringes is halved; it can also be expressed as a function of $\delta\lambda$:

$$l_c \sim 0.44 \frac{{\lambda_0}^2}{\delta\lambda}$$

Since with SS-OCT we are still using the Fourier transform we will be affected by mirror artefacts. This means that if we want to use the hole l_c an we have a reflector at distance $\frac{3l_c}{2}$ although technically outside of our imaging range it's mirror artefact will enter the image. this means we are effectively constrained to $\frac{l_c}{2}$ for the imaging range.

If we intend to use a k-clock we are required to do further considerations since the Mach-Zehnder interferometer (MZI) also affect the imaging range. In order to cover a range of $\frac{l_c}{2}$ it's required that the arms of MZI will be at least $2l_c$ long requiring a factor of 4 in length.

2.4.2.3 Axial resolution

Dependent on the tuning range of the source $\Delta\lambda$ defined as FWHM of the output beam.
If we consider a Gaussian spectrum source the FWHM of the peak an ideal reflector generates on our A-scans is given by:

$$\delta z \sim 0.75 \frac{{\lambda_0}^2}{\Delta\lambda}$$

2.4.2.4 New solution to DC component

The simplification to a simple photodetector has allowed a new possible configuration for the acquisition of the interference.
We introduce the **balance detector scheme**. It consist of using a coupler or BS in order to create 2 copies of the interference signal. One of the copies is then introduced to a π delay before reaching the photodetector with his "twin".
The interference of the two copies make it so that the DC component and parts of the exes noise will be deleted while the interference term will sum.
This configuration is useful to remove some of the post processing and reduce the blind region generated by the DC term of the interference.

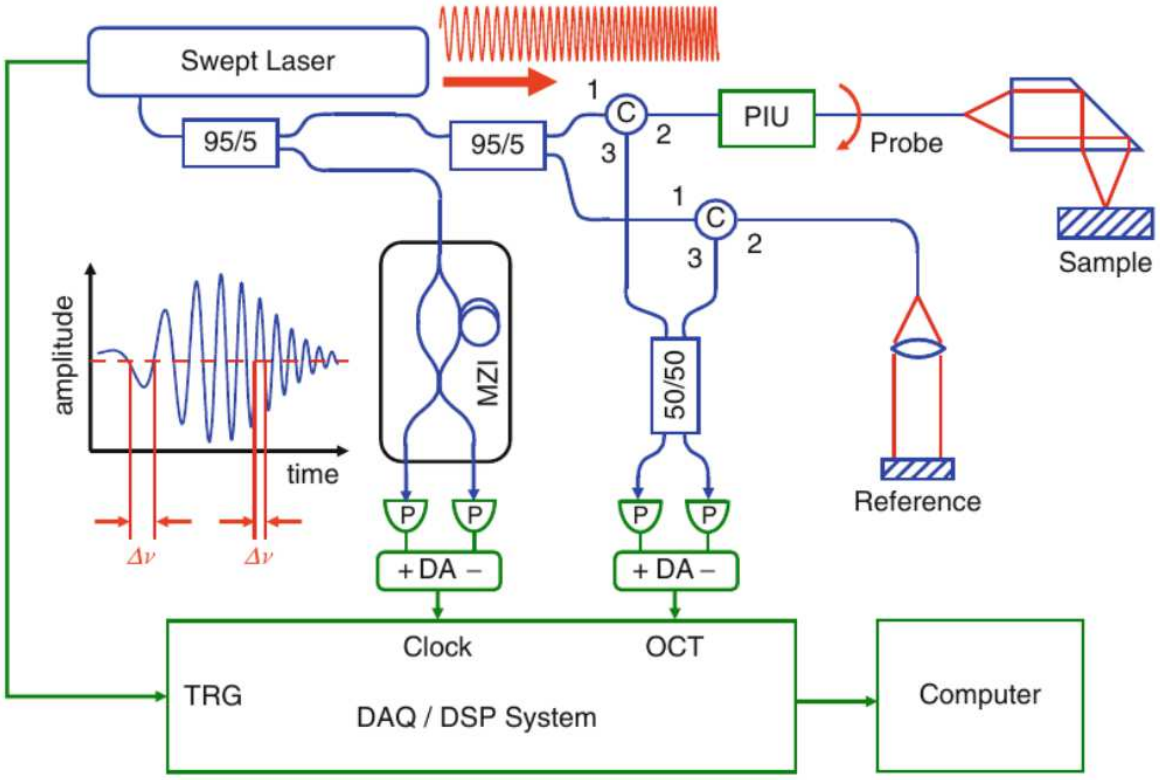

Figure 2.16: SS-OCT implemented with fibers using both k-clock and balance detector.

CHAPTER 3: Set up

In this chapter we will talk on how we implemented the polarization sensitive OCT (PS-OCT).
We will initially talk about the devices used in the realization of our imaging system and how these devices will affect the functioning of our OCT.
After introducing the components we will introduce the scheme we implemented with some considerations.
Finally the post processing program for resolving general problems that affects all SS-OCT set ups and are not unique to the polarization sensitive part of the system will be discuss. The processing and fix applied specifically for the polarization sensing part of our machine will be discuss in chapter 4.
To conclude in this chapter we will cover the aspect of the system that are common to all SS-OCTs.

3.1 Sweep source

The most important component of the SS-OCT configuration is the sweep source since it will define many of the performance of our final product. We will use a SSOCT-1310 by Axsun Technologies. The source is depicted in Figure 3.1; is class 3 laser working at 1300 nm that as the name imply is meant for SS-OCT schemes and in particular for organic tissue due to the central frequency

Figure 3.1: Axsun SSOCT-1310 sweep source

PARAMETER	UNITS	VALUE
Sweep Rate	kHz	100.2
Center Wavelength	nm	1305
Average Power	mW	25.7
Duty Cycle	%	77.3
Sampled Duty Cycle	%	50.5
External Clock Min Frequency	MHz	183.1
External Clock Average Frequency	MHz	307.0
External Clock Max Frequency	MHz	332.1
Sampling Clocks	–	1536

Table 3.1: Producer provided table of specs for Axsun SSOCT-1310

3.1.1 Spectrum

The wavelength range our device is able to cover is an essential parameter. Looking at Table 3.2 we can see that $\lambda_0 = 1305\ nm$ while the bandwidth is $\Delta\lambda = 140.38nm$. It's a good practise to check if the specific are verified by plugging the laser onto a optical spectrum analyser (OSA) to confirm.

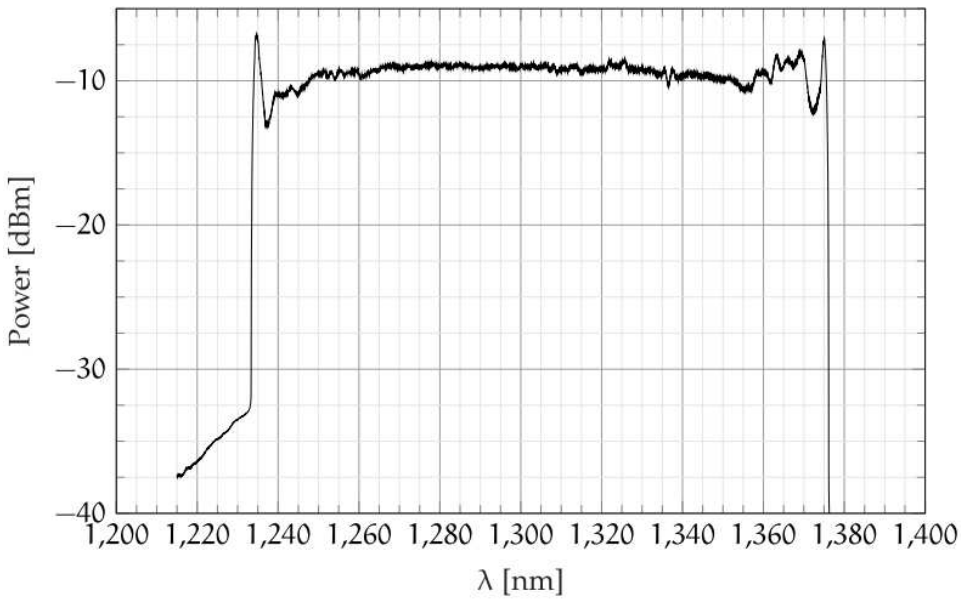

Figure 3.2: OSA analysis of the Axsun-1310 [1]

The test showed edge wavelengths of $\lambda_1 = 1237\ nm$ and $\lambda_2 = 1376\ nm$ so we have $\lambda_0 = 1307\ nm$ and $\Delta\lambda = 139\ nm$.

We can now evaluate the wavelength sweep from the duty cycle $d_c = 0.505$ and sweep rate $f_c = 100.2kHz$

$$\sigma_\lambda = \frac{\Delta\lambda\, f_c}{d_c} = 27.8\ nm/\mu s$$

Remembering the relation $f = c\lambda$ we can define the frequency sweep

$$\sigma_f = \frac{c_0\, f_c}{d_c}\left(\frac{1}{\lambda_0 - \Delta\lambda/2} - \frac{1}{\lambda_0 + \Delta\lambda/2}\right) = 4.9\ THz/\mu s$$

Since the Axsun is capable to give a k-clock we can consider its output as linearly sweeping the band following:

$$f(t) = f_0 + t\sigma_f$$

Where starting frequency is:

$$f_0 = \frac{c_0}{\lambda_0 + \Delta\lambda/2}$$

3.1.2 Axial resolution A-scan

The Axsun SSOCT-1310 is a gaussian source meaning that we can use the formula seen section 2.4.2.3 and the data in figure 3.2 in order to evaluate the width of the peak an ideal reflector would generate. This value will define our resolution in the depth direction.

$$\delta z = 0.75\ \frac{{\lambda_0}^2}{\Delta\lambda}$$

3.1.3 Sweep trigger

The Axsun is equipped with a trigger signal meant to be used in order to synchronise the acquisition of the A-scans.

The trigger signal has a voltage $V \approx [0,1.48]V$

The duty cycle is:

$$d_c = \frac{t_{high}}{t_{high} - t_{low}} \approx 0.97$$

The producer datasheet suggest to start the acquisition when the trigger voltage reaches $V \approx 0.71V$

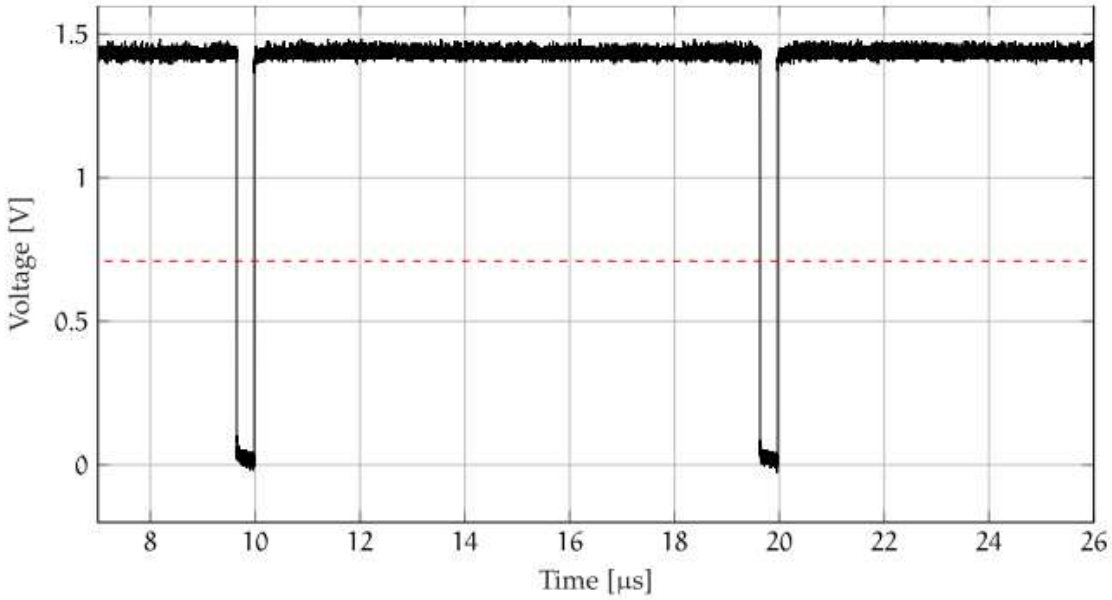

Figure 3.3: the trigger signal captured with an oscilloscope. The red line indicate the voltage at which we should start acquiring A-scan[1]

3.1.4 K-clock

The Axsun is equipped with a MZI in order to generate a k-clock to drive the data acquisition. As we already discuss the k-clock is a sinusoidal signal with variable frequency in time. The frequency of the signal at any given time is defined by the how much the two signals in the unbalance arms of the MZI differ in frequencies.

From figure 3.4 we see that it's voltage ranges in $[0,900]mV$ and averages at $460\ mV$.

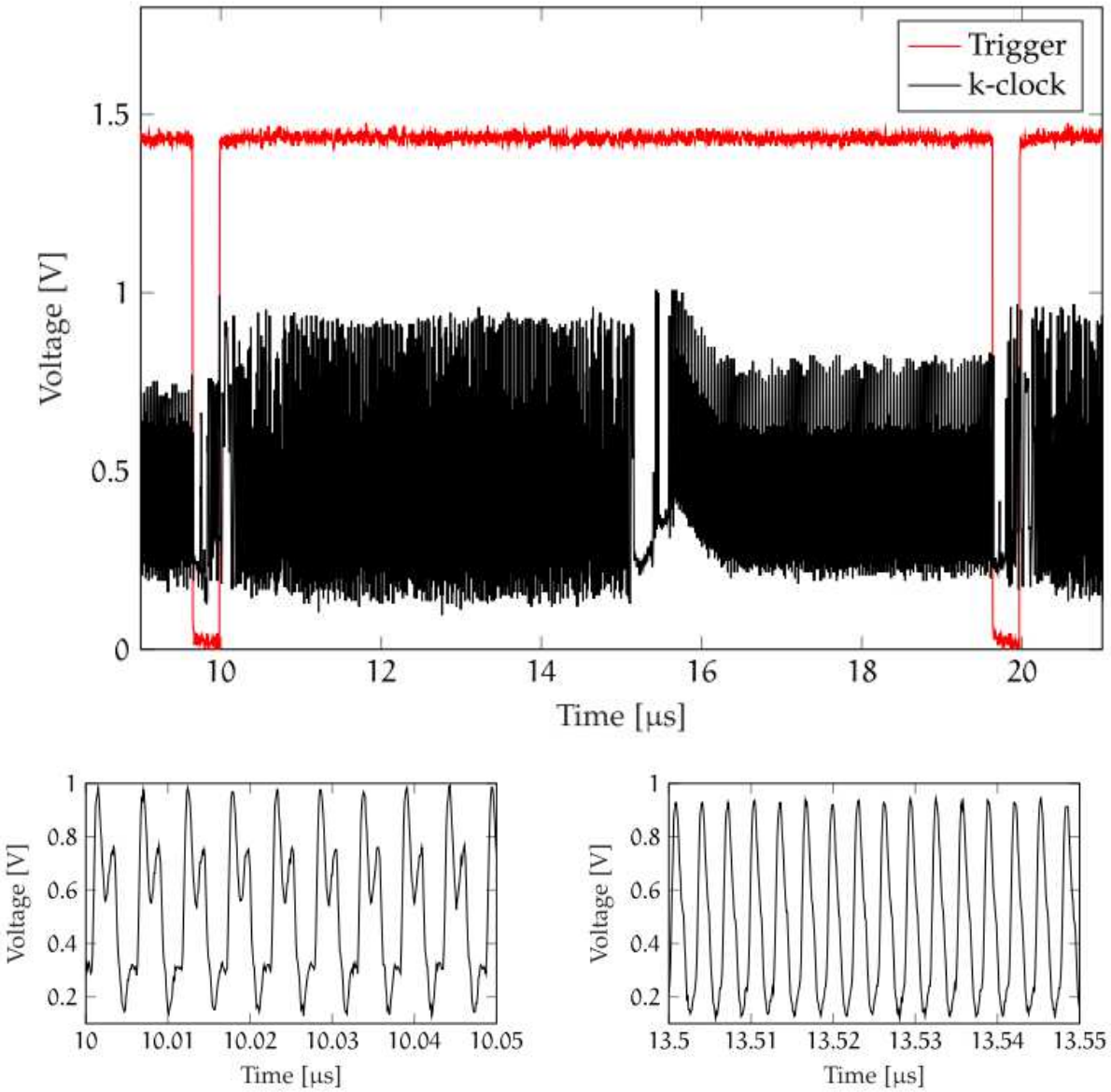

Figure 3.4: top the k-clock overlapped with the trigger signal taken with oscilloscopes. At the bottom we have a zoom in the k-clock at the beginning and end of the time window within two trigger dips[1].

Looking at figure 3.4 we can notice that the k-clock immediately before a trigger dip is different from the k-clock after the trigger. Since the signal is generated by an unbalance MZI with constant path difference; if the frequency sweep was linear the frequency difference of the lights interfering should be constant resulting in a sinusoid with constant. since we have changes in the instantaneous frequency of the k-clock we know there are nonlinearities in the sweep.

We can evaluate the instantaneous frequency change in the signal with the following procedure[1]:

- Subtract the average value of the signal
- Interpolate signal (t, y) to obtain$(\hat{t}, \hat{y})$
- Determine the instants in which the signal $(\hat{t}, \hat{y})$ crosses 0 to create the vector $\bar{I} = [\widehat{t_{\iota 1}}, \widehat{t_{\iota 2}}, \widehat{t_{\iota 3}}, \dots]$
- Subtract consecutive times of 0 crossing to create the vector $\bar{\tau} = [\widehat{\tau_{\iota 1}}, \widehat{\tau_{\iota 2}}, \dots, \widehat{\tau_{\iota N-1}}]$
- The instantaneous frequency is then given by$\widehat{f_\iota} = \frac{1}{2\widehat{\tau_\iota}}$
- Apply a low pass filter for a less noisy signal

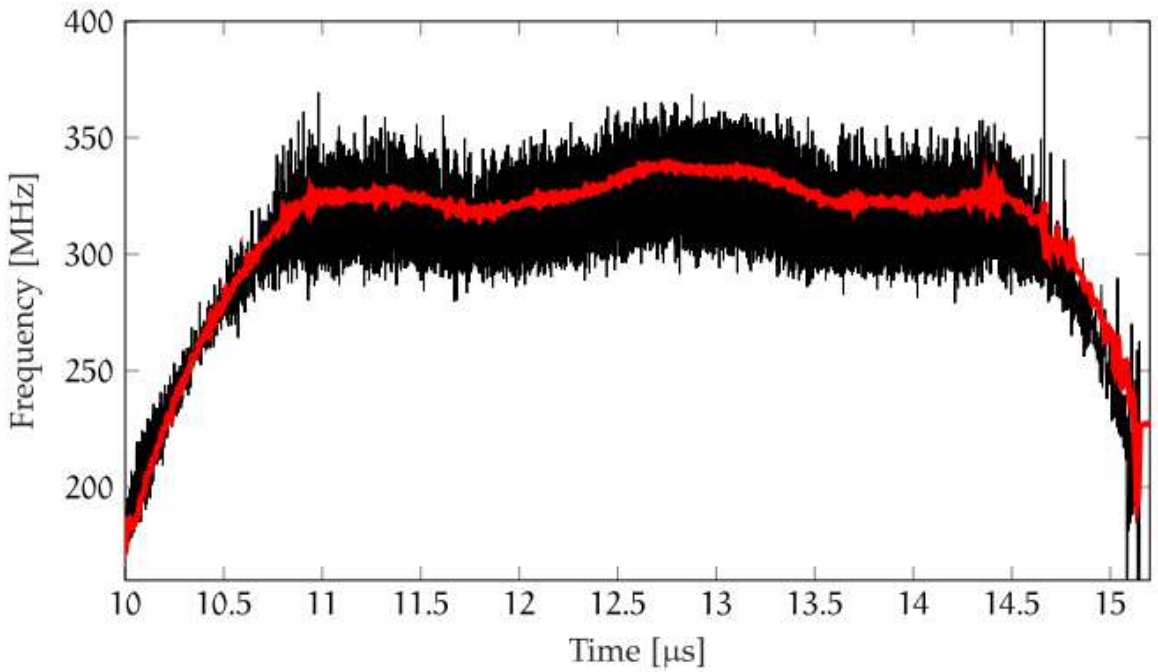

Figure 3.5: black line instantaneous frequencies of the k-clock. Red a filtered version of the k-clock instantaneous frequencies[1]

The true $\hat{f}_{max} = 339\ MHz$ so the true maximum imaging depth is:

$$f_b = \sigma_f \tau$$

Where τ is related to the mismatch of the reference-sampling arm and hence to the sample's layers depth. If we consider the sample as a layered structure of discrete reflectors then:

$$\tau_n = \frac{2n\ d_n}{c_0}$$

Where τ_n is the delay of the n layer, n is the refractive index and c_0 speed of light in the void For Nyquist theorem the maximum beat frequency is:

$$f_{beat}^{max} = \frac{f_{clock}^{max}}{2}$$

Hence maximum depth:

$$d_{max} = \frac{c_0\ f_{beat}^{max}}{2\sigma_f} = \frac{c_0\ f_{clock}^{max}}{4\sigma_f} \approx 5.1\ mm$$

3.1.5 Coherence length

As we saw in Chapter 2 in FD-OCT the coherence length affects the following parameters:

- Axial resolution
- Imaging range

In SS-OCT it also has to satisfy the inequality:

$$l_c \geq 2\ d_{max}$$

The 2 factor takes into account the round trip time. Since we already evaluate d_{max} we have at least:

$$l_c \geq 10.2$$

The actual coherence length has been experimentally evaluated by placing a mirror in the sampling arm and then evaluating the interference signal for different optical path differences [1].

The intensities of the interference signals, normalized by their maximum values, are plot in figure 3.6.

When the path difference is above a certain threshold the coherence function decays exponentially as in:

$$|\gamma(\Delta z)| \propto e^{-\alpha|\Delta z|}$$

We can clearly see this behaviour since we have $|\gamma(\Delta z)|$ decaying linearly in a logarithmic scale (we are using decibels in the plot).

We can now define the coherence length as the path difference for which $|\gamma(\Delta z)| = 0.5$ resulting in

$$l_c = 2 \cdot \frac{\ln 2}{\alpha} = 12.3\, mm$$

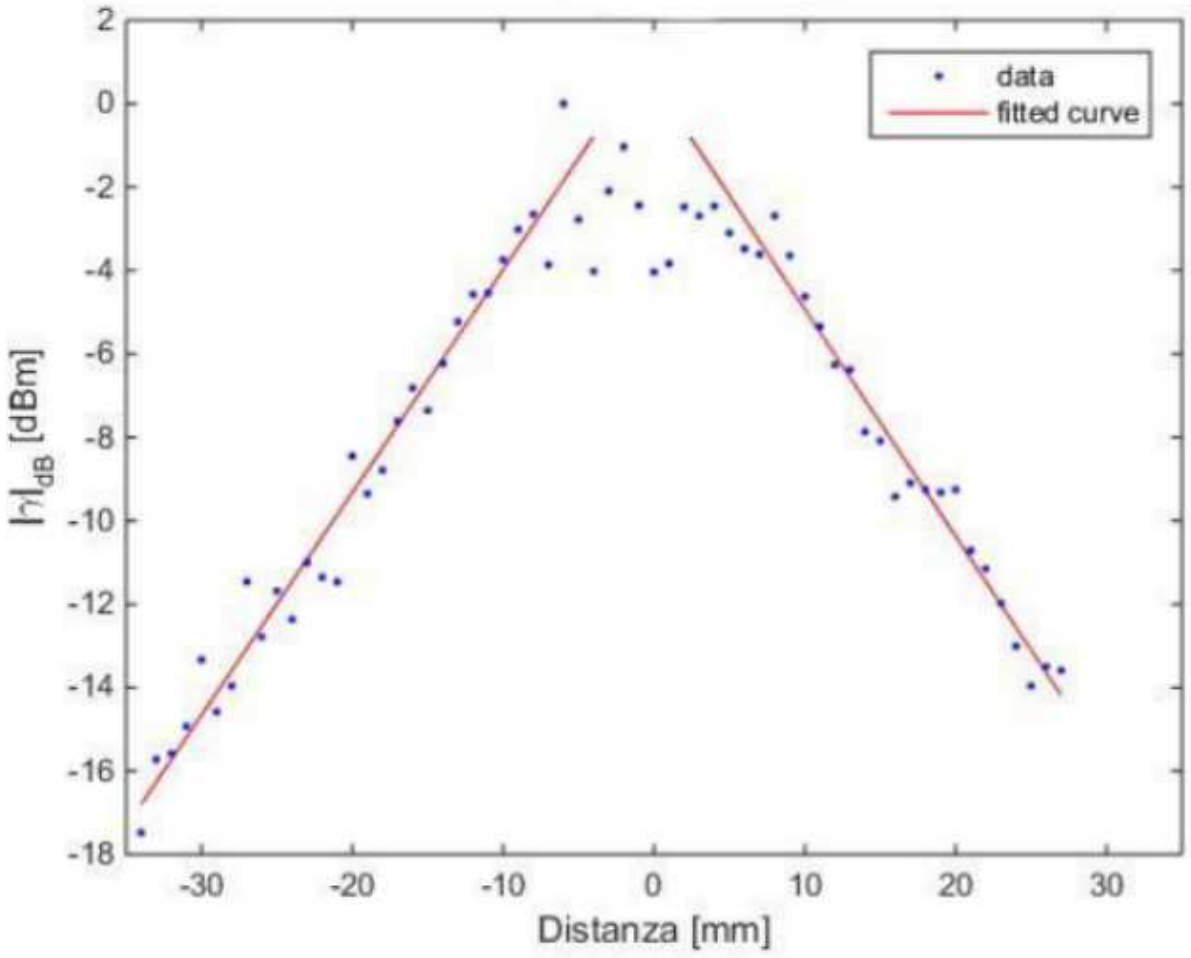

Figure 3.6: normalized coherence function in function of the optical path difference[1]

3.2 Scanning head

The scanning head is the termination of the sampling arm in charge of directing and focussing the light of the sweep source onto the sample. The second role of this apparatus is to capture the back scattered light and guide it to the photodiode.

For us the scanning head is compose by tree devices:

- Fiber collimator
- Galvanometric mirrors
- Focussing lens

We will go over each of them in the following sub-sections.

There is a schematic of our sampling system in figure 3.6.

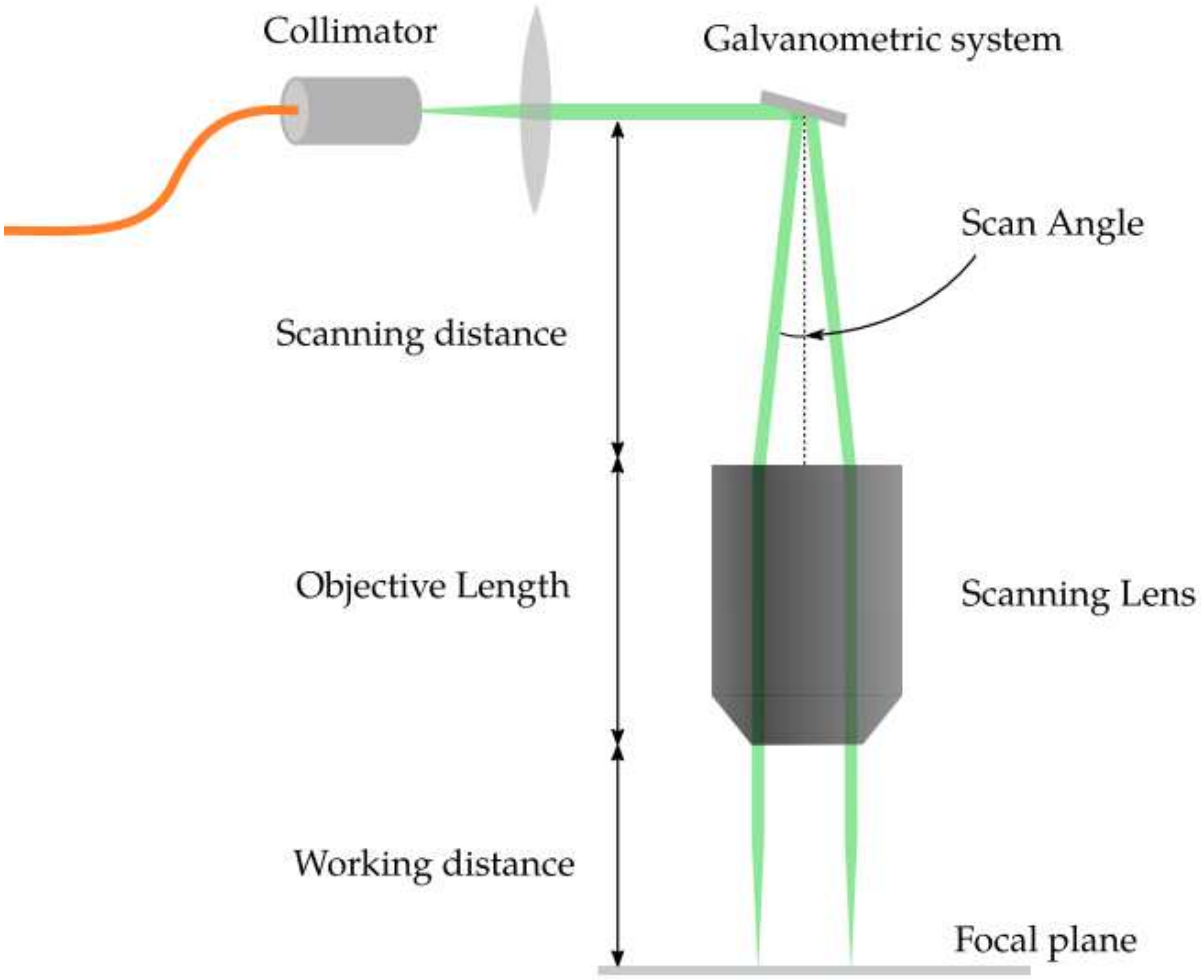

Figure 3.7: schematic of the sampling head [1].

3.2.1 Collimator

The role of the collimator is to take input light from a fibre and couple it into free space. Collimators also do the inverse function of maximising the light coming from free space that is couped into a fiber.

We use in our OCT system single mode fibers in order to eliminate modal dispersion and preserve the Gaussian profile of our sweep source. Since we have a Gaussian beam we can approximate the divergence angle of the collimator with the following formula[1]:

$$\theta \approx \frac{D}{f}\frac{180}{\pi}$$

Where D is the mode diameter and f the focal length of the collimator.

In our sampling head we use a Thorlabs F280APC-C1 meant to work in the 1310 nm range. The specifics are in figure 3.8.

PARAMETER	UNITS	VALUE
Central wavelength	nm	1310
Beam diameter	mm	3.4
Divergence angle	degrees	0.028
Lens numerical aperture (NA)	–	0.15
Focal length	mm	18.67

Table 3.2: Thorlabs F280APC-C1 datasheet.

3.2.2 Galvanometric Mirrors

The galvanometric Mirrors are a system of mirrors how's position/inclination is regulable thanks to a system of sensors and motors capable to pilot the mirrors position and angulature. Galvanometric mirrors (or galvo mirrors) in the sampling head isused to direct the laser beam onto different regions of the sample; enabling the scanning of tissues and hence the creation of B-scans and C-scans by accurately spacing the sampling beams of different A-scans. Galvo mirrors are generally eider a single mirror or a combination of two mirrors. The dimension are to be intended as the number of axes around which we can make a rotation.

Figure 3.8: The Thorlabs GVS002 galvo system used

Above is a photo of the Thorlabs GVS002 galvo system used. It's a two 1D mirror system that can be controlled electronically by modulating the tension on the motors that regulates the mirrors.

3.2.2.1 controlling the mirrors

As we already said the voltage signal at the mirror's motor is what regulates the angle at which the beams will be reflected.
In the Thorlabs GVS002 the maximum angle possible for the mirror is $\pm 12.5\ V$; but it can change if the laser beam width changes or the voltage scaling factor changes.
GVS002 has comes with three possible voltage scaling factors as we can see from figure 3.9

SCALING FACTOR	MAX. VOLTAGE	MAX. SCAN ANGLE
0.5 V/°	±6.25 V	±12.5°
0.8 V/°	±10 V	±12.5°
1 V/°	±10 V	±10°

Table 3.3: voltage scaling factors of Thorlabs GVS002

From simple geometrics we can see that the optical scan angle θ_o, ie the angle seen by the focussing lenses, is twice the angle impressed by the mirrors θ_m.
Using the scaling factor $\alpha = 1V/°$ the maximal optical angle is $\theta_o^{max} = \pm 20°$.
Now we want to discover which voltages we have to use in order to make use of the full angles supported by the lenses.
We will see that the lens support incidence angles of $\pm 7.5°$ leading to a maximum voltage of:

$$V_{max} = \pm \frac{7.5}{2\alpha} = \pm 3.75\ V$$

Larger voltage will introduce distortions since the θ_o will not fall within the range of angles intended for the focussing lenses.

The beam spot in the focal plane is controlled by the angles of the mirrors and the focal length of the focussing lens with the following relations.

$$r(t) = \begin{cases} x(t) = EFL\ tan\left[2\alpha V_x(t)\frac{\pi}{180}\right] \\ y(t) = EFL\ tan\left[2\alpha V_y(t)\frac{\pi}{180}\right] \end{cases}$$

Where $V_i(t)$ is the voltage at time t on the motor of mirror I where i=x or y. α is the voltage scaling angle selected.

3.2.2.2 Image distortion

Moving components of the system will always introduce distortions. In particular the galvo mirrors will introduce these tree:

Pillow-shaped image field: the relative distance between the mirror is dependent on the angles they assumes. This means that the focal plane will be bent since depending on the angle imposed. We can see a representation of this effect on figure 3.10

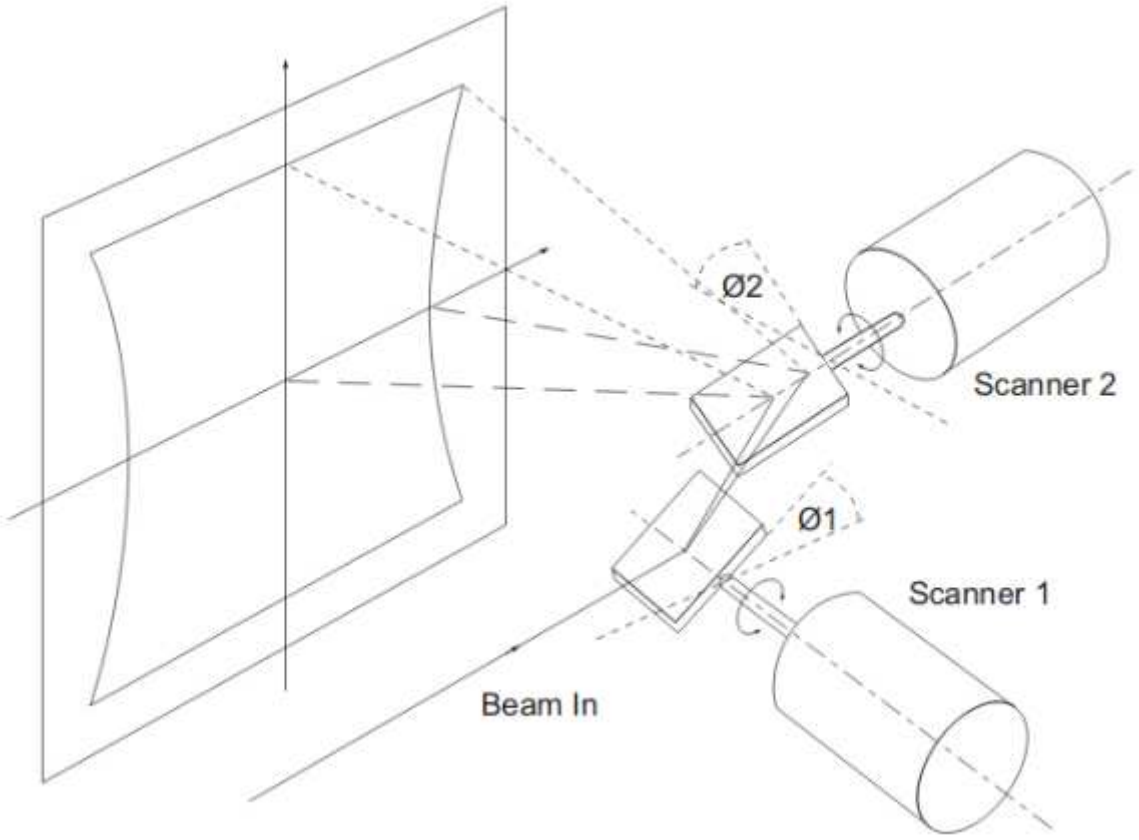

Figure 3.9: representation of pillow-shaped field[1]

Varied spot size: the focus points of a normal lens manipulating a laser beam lies on a spherical surface. This means that when scanning a plane sample the spot sizes on the plane are different at each point. This leads to distortions if the A-scan taken have spots that overlap.

Tangent dependence: from the equation on the beam spot on the focal plane we see that the dependence on the voltage is not linear. This may introduce distortions due to the fact that the

beams are not equally spaced since lower absolute value of voltage will generate smaller angles.

These last two distortion are increasingly more relevant the larger the beam is since the distortion appear if A-scans comes from beams that overlap.

3.2.3 Focal lens

In order to have high resolution images we are required to focus the beams directed by the galvanometric mirrors.
The reason why the focussing is crucial is because the backscattered light contains information about the illuminated area hence smaller spot sizes allow for a more precise sampling capabilities allowing to take in more indipendents A-scans (with independent we intend that there are no common regions acquired by multiple A-scans).
In OCT systems the most common lenses are telecentric scanning lenses, characterized by almost flat focussing planes, making them ideal for our application.

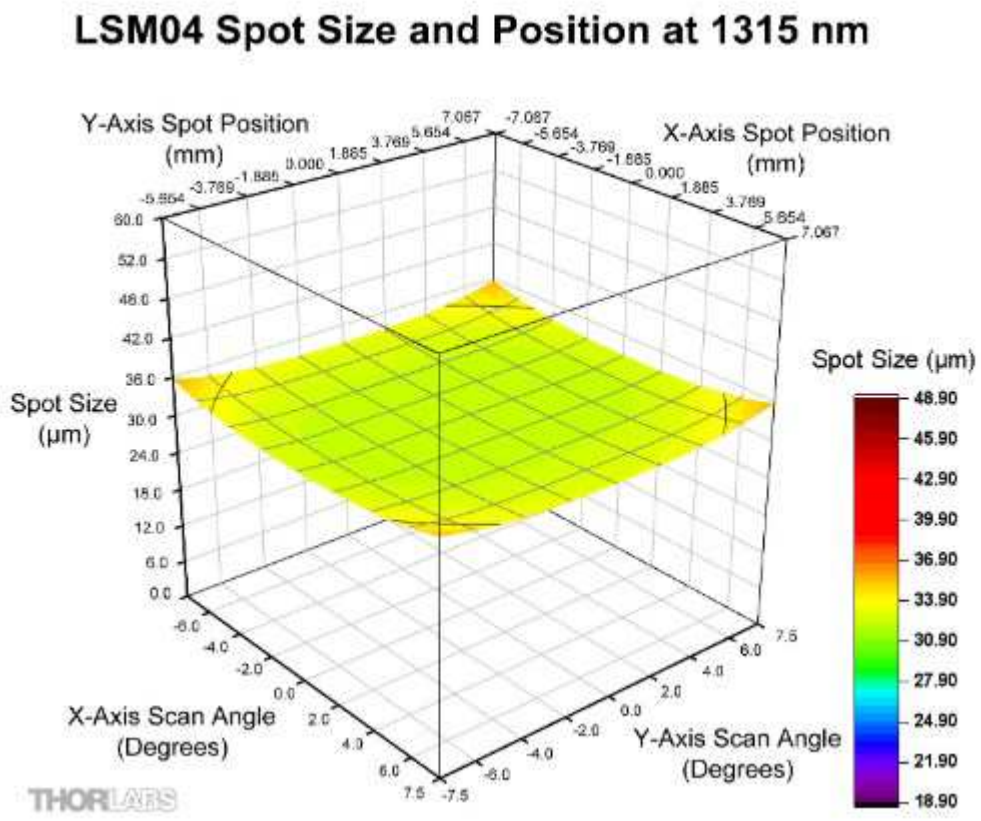

Figure 3.10: focus plane representation and simulation of spot size for different impinging angles.[1]

The main parameters that define telecentric lenses are:

- **Entrance Pupil size (EP):**diameter collimated laser beam that maximise image resolution. If we have a single galvo metric mirror the EP is located at the mirror pivot point. If there are two it is located between the mirrors.
- **Scanning Distance (SD):**distance between EP and base of lens.
- **Scan Angle (SA):**angle between incoming light and optical axes of the light.
- **Working Distance (WD):**distance from the edge of the lens and the focal plane
- **Parfocal Distance(PD):**distance between base of the lenses and focal plane. Equal to WD plus objective lens.
- **Field of View(FOV):**area on focal plane that can be imaged with resolution better or equal to what guaranteed by the lens datasheet.
- **Depth of View (DOV):**distance of the planes where beam spot diameter is $\sqrt{2}$ greater than in the focal plane.
- **Spot size:** the diameter of the beam on focal plane.

The lens we used in this thesis are the LSM04 from Thorlabs. The specifics are on figure 3.12

PARAMETER	UNITS	VALUE
Wavelength range	nm	1250-1380
Effective Focal Length (EFL)	mm	54
Entrance Pupil size	mm	4
Working Distance	mm	42.3
Parfocal Distance	mm	80.8
Scan Distance	mm	18.9
Maximum Scan Angle	degrees	$\pm 7.5 \times \pm 7.5$
Field of View	mm^2	14.1×14.1
Depth of View	mm	0.61

Table 3.4:LSM04 datasheet

3.2.3 Lateral resolution

We can evaluate an estimate of lateral resolution which is determined by the spot size.
For Gaussian beams the formula is[15]:

$$\delta x \cong \frac{4f\lambda_0}{\pi d}$$

Where λ_0 is the central wavelength, f is the focal length and d diameter of the beam at the lens entrance. Using the parameters in figure 3.12 the LSM04 offer a resolution of:

$$\delta x \cong \frac{4f\lambda_0}{\pi d} = \frac{4\lambda_0}{\pi d}\frac{EFL}{EP} = 22.5\ \mu m$$

We have to remember that diameter of the beam exiting the collimator is the one entering the lens so is $d = 3.4\ mm$ not the EP suggested in the datasheet. Resulting in $\delta x \cong 26.5\ \mu m$.
Now we can evaluate the depth of view since it's dependent on the lateral resolution using the formula[15]:

$$b = \frac{2\delta x}{\lambda_0}$$

From the relation we can see that having a smaller spot size is desirable in order to increase the depth of view. The reason why the depth of view or confocal parameter is important is to guarantee a larger region in which the beam radius doesn't change too much avoiding overlapping between regions analysed by different A-scans.

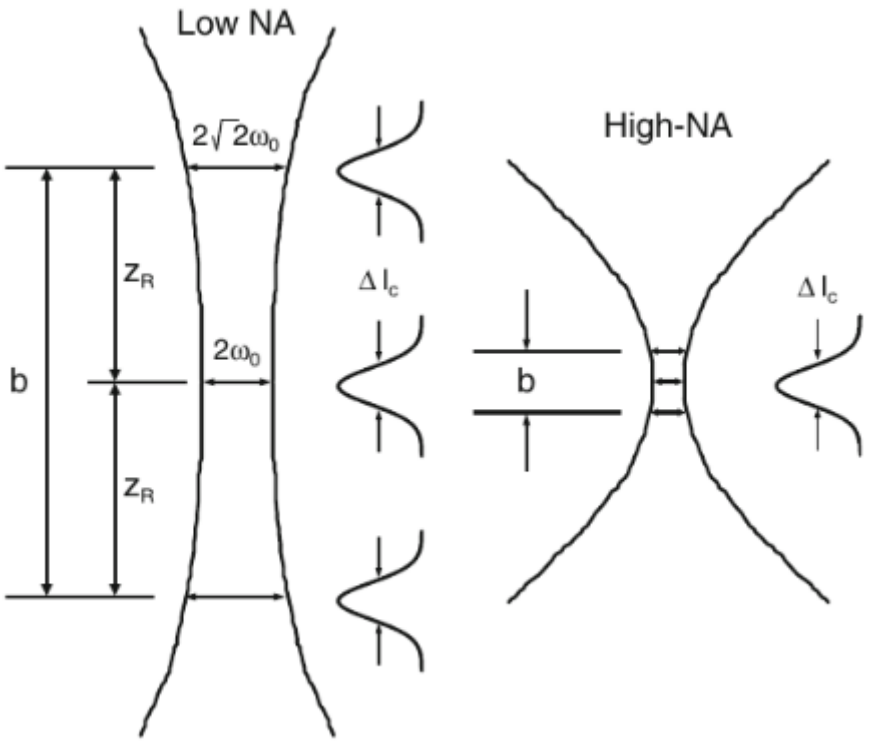

Figure 3.11: rappresentation of a the cone created by a lens focussing a laser beam. It's indicated the depth of view.

3.3 Acquisition board

To capture the and digitalize the interference signal in real time we require highly specialized data acquisition (DAQ) device.

For SS-OCT it's desirable to have a DAQ with configurable acquisition rates and capable of receiving and use a k-clock signal in order to reduce the post processing require to compensate the nonlinear sweep effects and hence enhance the imaging speed.

In our system we will make use of a AlazarTech ATS9350 projected for: OCT, ultrasound and radar application.

The device is a 8-lane PCI Express 2.0 cards with the following spec:

Figure 3.12: AltzarTech ATS9350

- 12 bit sample resolution
- 250Mhz input bandwidth
- 2 input channels each with a dedicated ADC and and separate user define sampling rates between 2MHz and 500MHz. resulting in a maximum throubput of 2GB/s
- User selectable input voltage range, from $\pm$40 mV up to $\pm$4V
- External trigger support
- Variable frequency external clocking
- Ausiliary connector configurable to be either a trigger output or an acquisition start trigger.
- Dual-port 128 Megasamples on-board memory
- On board field programmable gate array (FPGA) for the computation of the fast Fourier transform on one of the input channel.

AltzarTech also gives a software to configure the device with also functionalities for the acquisition and display of the signal. To develop application it's possible to make use of a software development kit (SDK) composed by libraries and header for programming languages such as : C/C++,Python and MATLAB. The DAG has been installed in a Dell Precision T5810 workstation with the specifics:

- Intel Xeon E5-1650 v4 3.6 GHz, 6 cores, 12 threads
- 16 GB of DDR4 ECC RAM at 2400MHz
- 256GB SATA SSD
- NVIDIA Quadro M4000 with 8 GB of DDR5 memory

3.3.1 Data acquisition

The ATS9350 organise the input data into 2 categories. The first one is the so called records. These are a collection of samples that have been acquired immediately after receiving a trigger (is configurable using the libraries of the SDK). For our application records corresponds to A-scans.
The second data structure supported are buffers. In this case they are a collection of records making them equivalent to B-scans. The number of records per buffer are also configurable, but is somewhat dependent on the dimension of the samples since the overall size cannot exceed that of the actual hardware buffer used by the device. The transmission of data in the second acquisition mode is organized as transmitting a hole buffer in a block.
As we somewhat anticipated ATS9350 supports two acquisition modalities.
First mode is **single port mode**: acquire data to the on-board memory and when the acquisition ends it's sent to the PC memory. We lose A-scans triggered during the transmission phase hence this mode will not be used by us.
Second mode is Dual-port mode or **autoDMA**: this modality saves the samples on the on-bord memory while immediately starting to transfer the data on the PC memory. This modality avoids losing triggers and hence it's our chosen mode. In this configuration the DAQ memory is a giant FIFO structure that is constantly being filled at the tailed and emptied from the front of the queue.

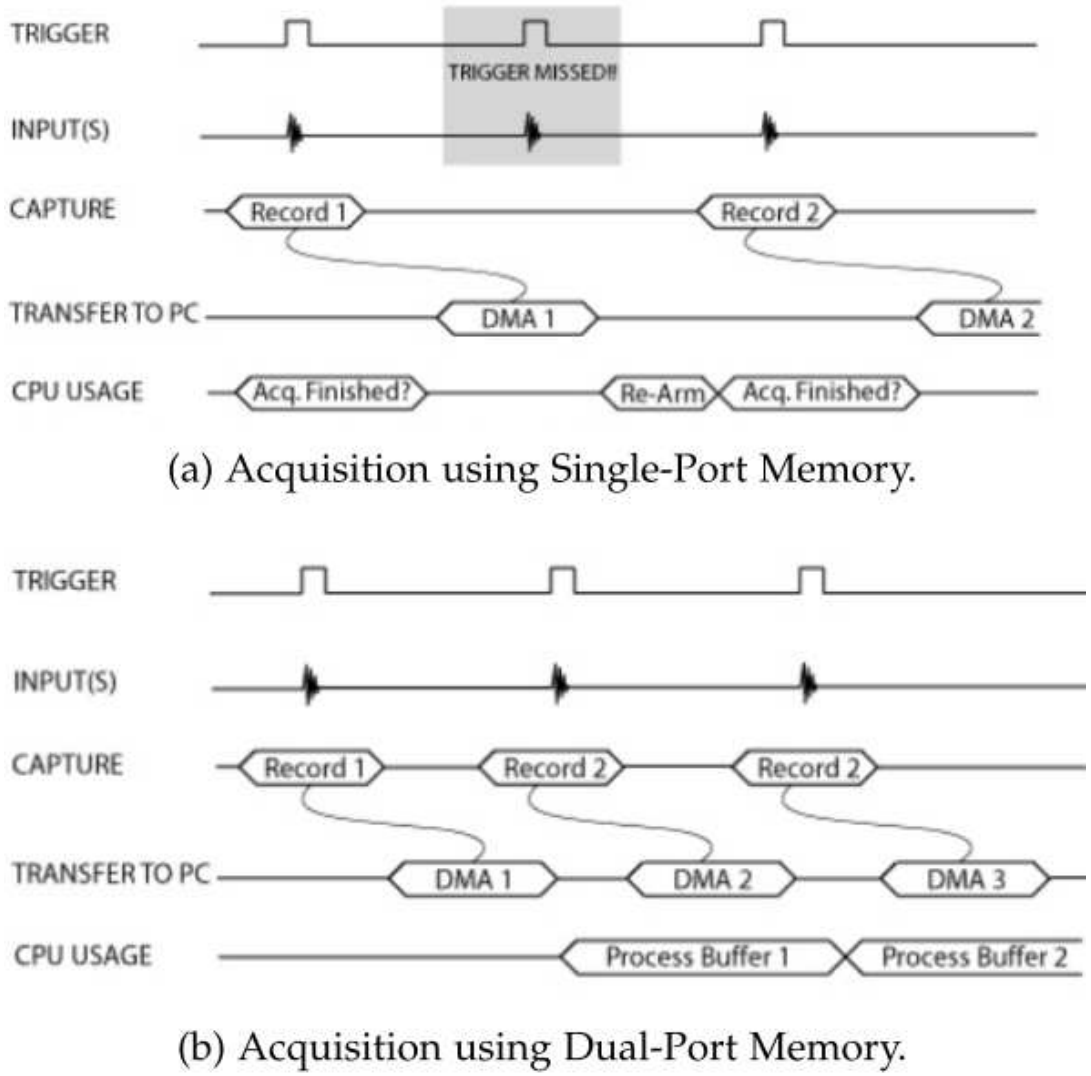

Figure 3.13: a visual representation of the two modalities.[1]

Looking at figure 3.15 we can make some comparison between the modalities.
Single-Port mode the triggers arriving during Direct Memory Access (DMA) are lost since all the CPU cycle are dedicated to the acquisition with no space for processing. In the AutoDMA mode instead no trigger are lost and 90% of the CPU resources are available for data processing.
AutoDMA mode uses hardware circuitry to automatically initialize the data in the memory, freeing the CPU resources. The disadvantage of this mode is the impossibility to freely choose how the data will be configured. This means that the raw data transferred from the DAQ to the PC need to be converted into floats by the PC in order to be processed. Auto DMA also make use of multiple software driver, in order to control one port for the data acquisition and the other for the transmission.
Auto DMA is available in different modalities that will be described.

3.3.1.1 Traditional Auto DMA

Acquire pre-trigger and post-trigger data that are sent to the user as a single buffer each time a trigger event occurs. Buffer contains up to 8192 records; each time a record has been acquired it will be transmitted using a header containing a 40 bit timestamp.
Fast trigger repeat rates are not supported and may create overflow even if we are transmitting data at the maximum sustained rate and the on-board memory isn't filled.

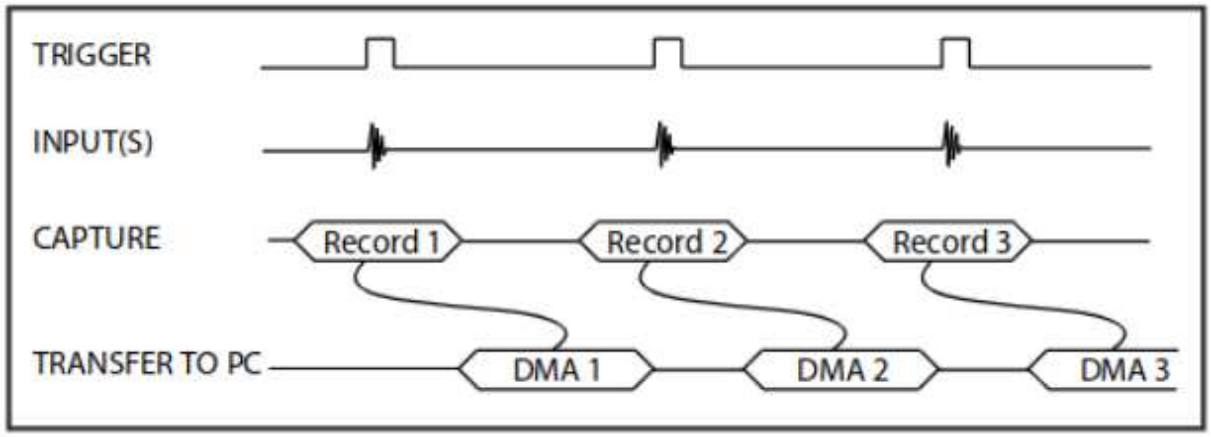

Figure 3.14: a visual representation of traditional auto DMA[1]

3.3.1.2 NPT AutoDMA

No Pre-Trigger (NPT) AutoDMA is projected for applications that don't require information preceding the trigger event. It only stores data after the event; optimizing the memory bandwidth.

It doesn't make use of headers since the data are taken sequentially only when a trigger has been received. Dropping the header and not having the necessity of a constant access to the memory in order to preventively register data for pre-trigger information, allows NPT to handle high trigger rates. The only constrain in acquisition speed is given by the slowest between the PCIe transfer speed or the user application data consumption rate.

This modality has been conceived specifically for : OCTs, ultrasonic scanning and radar application and hence it's the modality we will use.

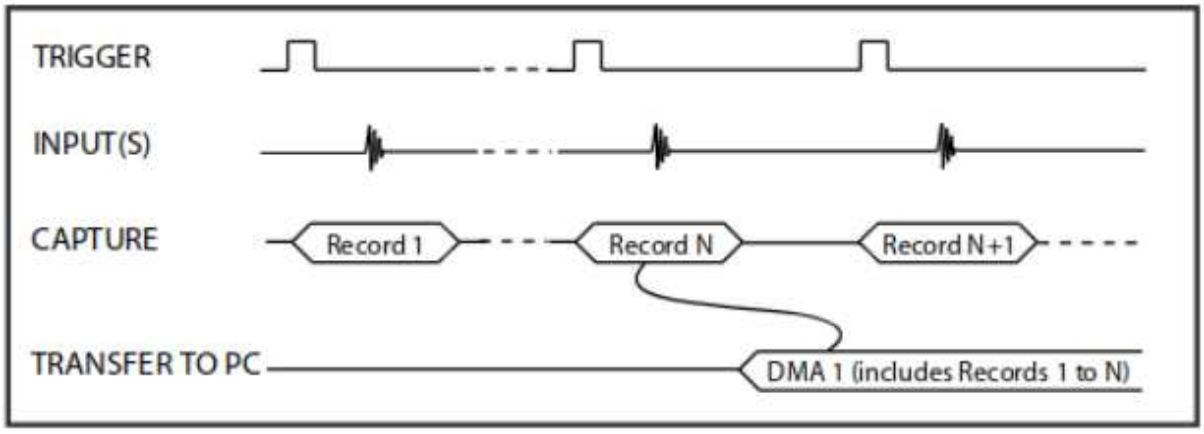

Figure 3.15: diagram of NTP AutoDMA

3.3.2 FFT Module

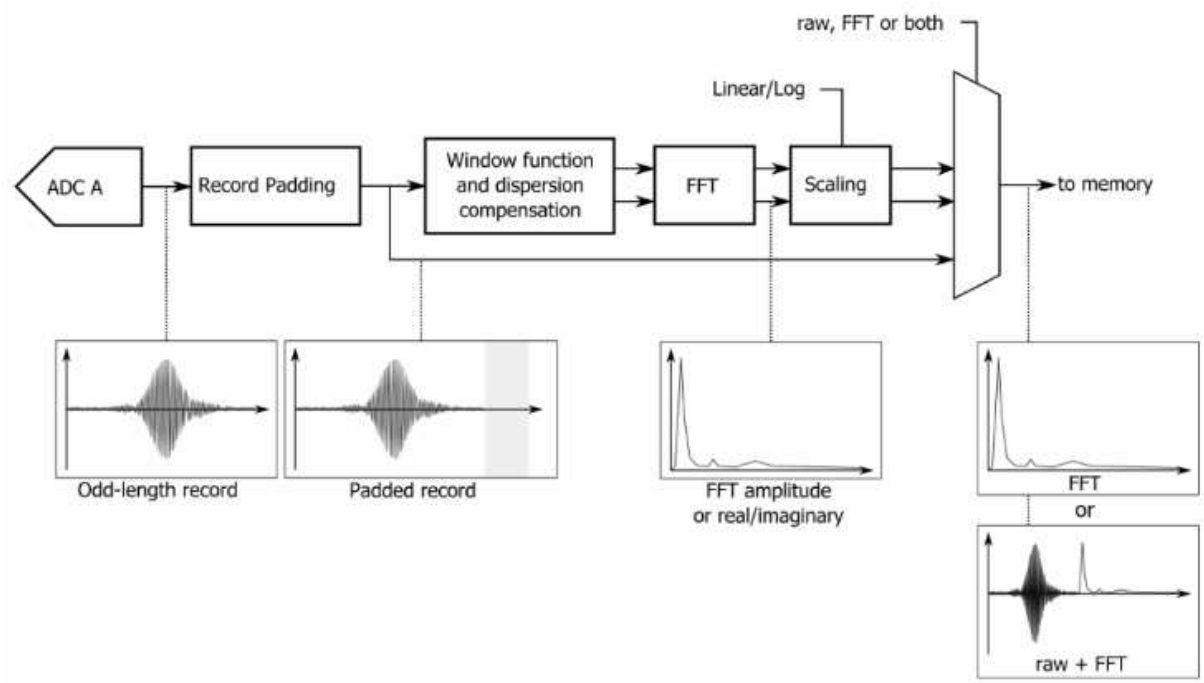

Figure 3.16: diagram of FFT-module[1]

As already said, the ATS9350 is capable to compute the FFT on records acquired thanks to the FPGA module that is integrated.

The module takes input records to zero-pad into a power-of-2 length. It's then multiplied by a complex windowing function and fed to the FFT module. The output of the FFT is then scaled and converted onto logarithmic scale. The process is illustrated in figure 3.18.

The presence of the FFT module is meant to drop the requirement for a GPU on the user hardware. Considering that we will have to make use of the GPU in order to create textures and the evaluation of the Stokes vectors we will not make use of this module and instead delegating the processing of the FFT to the GPU of the PC in which we are running the application.

3.3.3 External clocking

ATS9350 has an SMA input for external clock. This connector can support sinusoidal signals; therefore can be used with the k-clock our Axsun sweep source can produce. The input impedance is fixed at 50 Ω and AC coupling is used.
The DAQ samples on the rising edge of the k-clock, when the crossing of a configurable threshold is sensed. Three operation are supported on external clocks which are:

- 10 MHz Reference Clock
- Slow External Clock
- Fast External Clock

The third is our choice since the Axsun SSOCT-1310's k-clock range is contained only in this modality.
ATS9350 has a dummy clock switchover functionality. This allows the DAQ to switch from the external clock to a internal one for a configurable amount of time after each record. When the dummy clock time ends the ATS9350 will return to use the external clock when a new trigger appear. This feature is useful in between frequency sweep (since as we already explained, when a new sweep starts we have a transitory time in which the output frequency of a sweep-source laser is not stable generating a distorted k-clock).

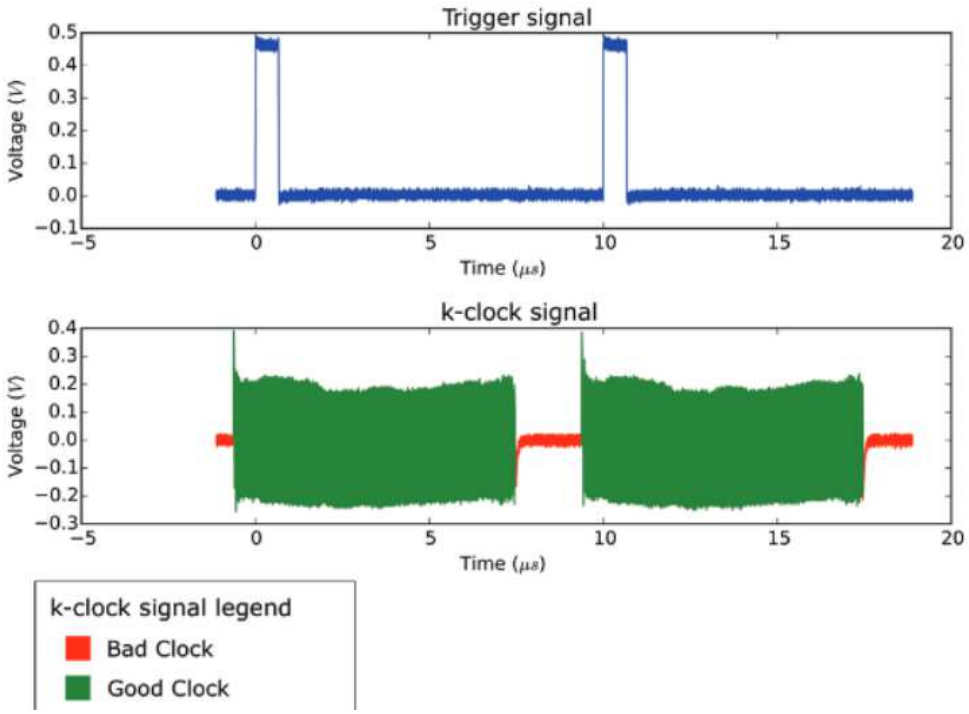

Figure 3.17: example of distorted k-clock requiring a dummy

3.3.4 Triggering

For our application we have to configure the how our DAQ will use the triggering.

1. Set NTP AutoDMA
2. Connect the laser sweep trigger to the SMA port. At each rising edge the DAQ will acquire an A-scan. The A-scan parameter should respect the following constraint:
    - At minimum 256 samples
    - The samples mast be multiple of 32
    - The sample must be less than the maximum number of sampling clocks that the k-clock offer. This means that the number of rising edges that cross the threshold for sampling has to be greater than the number of samples for A-scan. The number of useful clock offered by the Axsun is 1536; this number satisfy the first two rules, but to avoid possible complications due to instabilities it's better to only use 1504 clocks.

The acquisition of a B-scan require the Auxiliary port to be configured as "Trigger Enable In" and a TTL pulse must be supplied. When a pulse is detected on the Auxiliary port it will wait for a certain number of A-scan before sending the hole buffer. The buffer sent corresponds to the B-scan. After the transmission the DAQ will wait another pulse before starting the acquisition of a new buffer.

2.5 Fiber coupler

Since all of our devices (sweep source, acquisition head and photodiode) have fiber ports as Input/Output, we intend to use couplers instead of a BS in order to split the light beams. Couplers main advantages compared to the traditional crystal cube Beam splitter having all input and outputs already in fiber; cubic BS require the use of collimators and can introduce alignment problems hence more losses. A schematics of our couplers is in figure 3.20

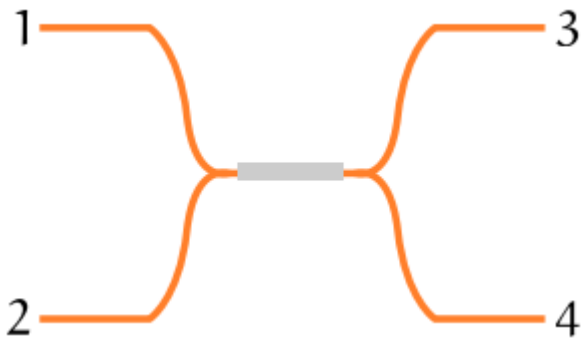

Figure 3.18: 4 ports fiber coupler

Couplers are typically 4 ports passive devices (3 port are also common) used to split the signals arriving to one port onto the two ports on the other side. This means that the pairs 1,2 and 3,4 are isolated. The device is composed by two fibers that are fused together in order to have the cores extremely close to one another. The closeness of the cores allows for a certain percentage of the light to "bleed" into the other fiber obtaining the split. The core closeness defines the parameter ρ^2 which define the percentage of intensity that will stay in the original fiber. The remaining $1 - \rho^2$ will be transmitted onto the other fiber while undergoing a phase shift of $\frac{\pi}{2}$ during the transition.

The property of the coupler can be written as a scattering matrix as below:

$$S = \begin{bmatrix} 0 & 0 & \rho & j\sqrt{1-\rho^2} \\ 0 & 0 & j\sqrt{1-\rho^2} & \rho \\ \rho & j\sqrt{1-\rho^2} & 0 & 0 \\ j\sqrt{1-\rho^2} & \rho & 0 & 0 \end{bmatrix}$$

In our OCT system we used the following couplers:

- 2 Thorlabs TW1300R5A2 50:50 couplers
- 1 Thorlabs TW1300R2A2 90:10 coupler

The 90:10 fiber has been used to separate the light that will go to the sampling arm and the reference one. It's best to send 90% of the intensity to the sampling arm since the backscatter light percentage that will be capture by the fiber is typically extremely low.
The arms of these couplers have different colours in order to more easily distinguish the ports. The colour code is also used to distinguish the direct paths. The white port on the left is direct to the white port on the right while the blue on the left is direct to the red. The path length of all the possible paths is inside the datasheet that Thorlabs gave and are reported on figure 3.21.

	Path length [mm]		
PATH	50-50A	50-50B	90-10
White ↔ White	2102	2098.61	2112.58
White ↔ Red	2108.26	2119.47	2113.86
White ↔ Blue	2101.15	2095.97	2129.02
Blue ↔ Red	2107.40	2116.87	2130.3

Table 3.5: datasheet of the pats lengths.

These data are not so relevant to us since used we used an ODFR to evaluate the length of each arm on the final optical circuit.

3.5 Fiber Based Polarization combiner/splitter

It's a variation to the coupler. It's a 3 port passive optical device. Its design consist of three ports one on one side and the other two on the other.

Figure 3.19: photo of the FBP

The device accept a generic beam from the "isolated" fiber and split the incoming light into the two port on the other side depending on the polarization of the EM wave. It can also be used to combine two orthogonally polarized beams into a single one.
Ports are one on one side and the other two on the other as illustrated in Figure 3.23.

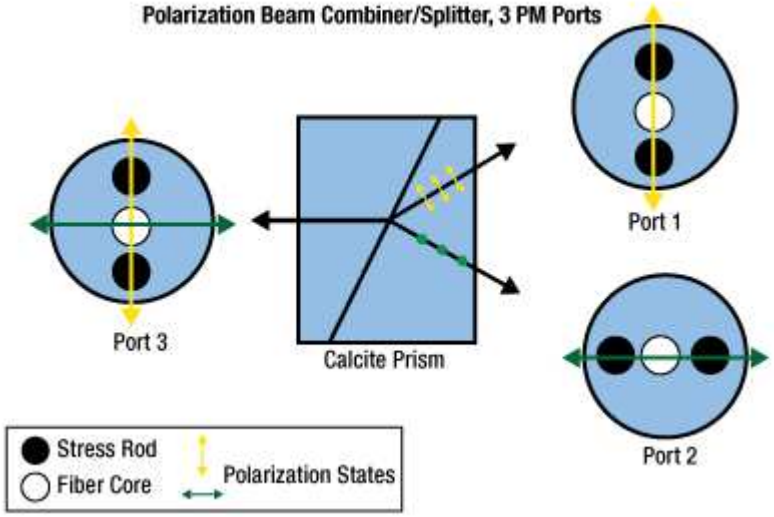

Figure 3.20: scheme of a FBP reporting the slow axes of the fibers and the angles at which different polarization are transmitted.

The device is made of three polarization maintaining fibers and a calcite prism. The prism is the key component since it's able to change the direction of propagation of light base on its polarization. The role of the fiber is to be correctly located in order to receive the beam with the slow axes align to the polarization of the light that will reach them in order to not manipulate the state of the incoming wave.

3.6 Fiber Polarization Controller

We use a manual fiber polarization Controller (FPC) with two loops. It's a Thorlabs FPC025 meant to work for light in the range of $\lambda\ \varepsilon[1260\ ,\ 1625]\ nm$ and is illustrated in Figure 3.24.

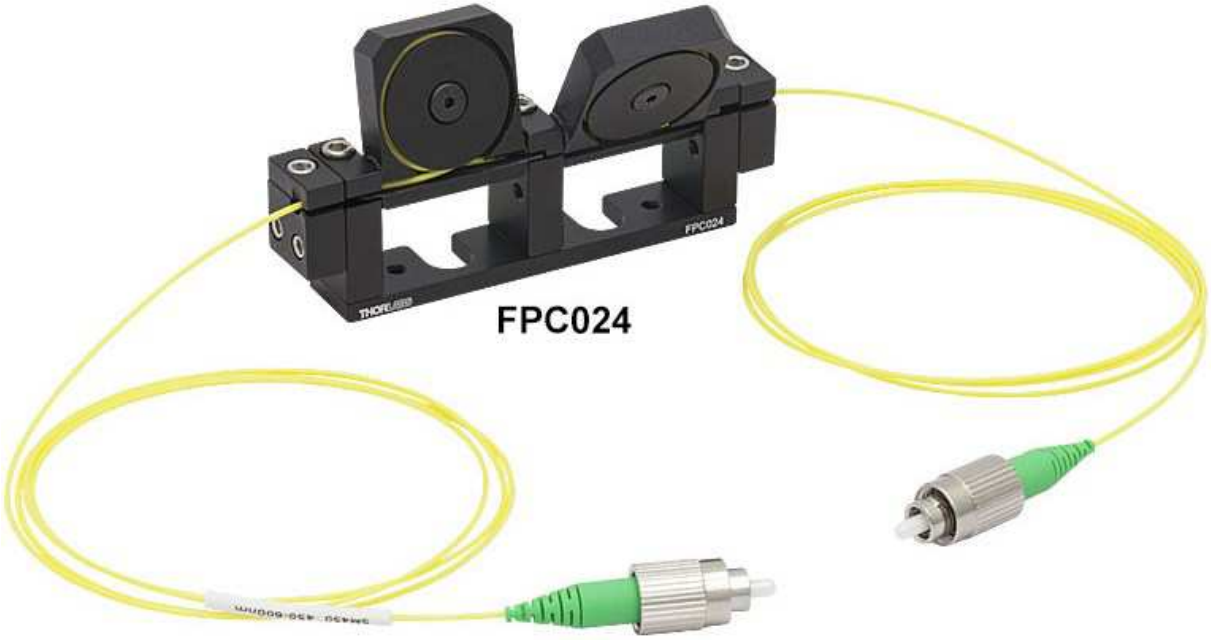

Figure 3.21: image of a two loops Thorlabs FPC024 the only difference with the FPC025 is the radius of the loops that determine the wavelength range.

The device is the black structure that encase the fiber. The device require to insert a fiber and fix it using the screws; we should avoid excessive pressure on the fiber. Once we have locked in the fiber we can twist it by changing the angle between the loops or stretch the waveguide in the loops by regulating the radius using the black screws at the centre of the circles.
The general idea is that causing mechanical stress onto a fiber we will change its Eigen states. Changing the principal polarization of the fiber will induce a change in the polarization of light emerging after the transmission. The problem whit manual FPC is that the end polarization is not easily controllable.

3.7 Balance Detector

The detector is composed by two balanced photodiodes and an ultra-low noise, high-speed transimpedance amplifier. The detector are matched in order to increase the noise rejection. As we said in the SS-OCT section the purpose of the Balance detector is to subtract the two copies of the interference signal generated by a BS in order to cancel common mode noise and the contribution of the first term of the interference.
We are using 2 PDB440C produced by Thorlabs.

Figure 3.22: PDB440C

The main features of this model are:

1. Bandwidth up to 2.5GHz
2. Four central wavelength available:
    - 320-100 nm
    - 800-1700 nm
    - 900-1400 nm
    - 1200-1700 nm
3. >20dB Common Noise Rejection Ratio
4. FC Fiber inputs
5. Switchable power supply

3.8 Optical circuit

The realization of the optical circuit for our polarization sensitive OCT (PSS-OCT) has been developed in two steps to ease the detection and correction of signals deformation due to various phenomenon.
In this chapter we will cover the first step of our system implementation. The second step consist in a simple modification of the circuit in order to separate different light polarizations for the evaluation of Stokes vectors. Since the second phase of development is fully focussed on the polarization sensitive part of the OCT it will be discuss in Chapter 4.

3.8.1 First step: Simple OCT Circuit Implementation

To start we focussed on implementing a functioning SS-OCT with no polarization sensitive capabilities.

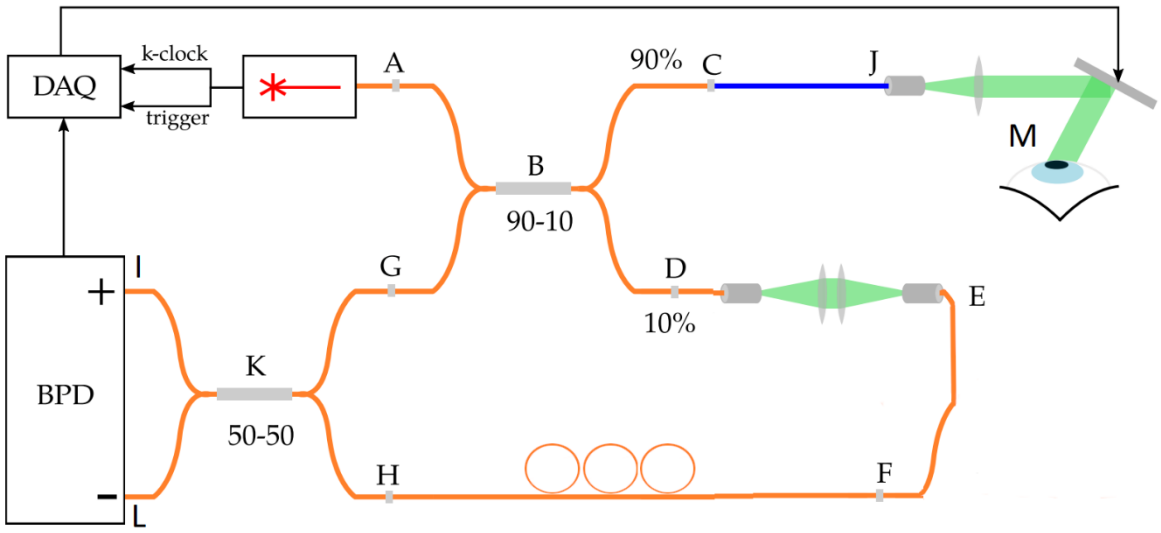

Figure 3.23:Diagram of optical circuit implementing a simple SS-OCT that will be the base for the realization of a PSS-OCT objective of this thesis.

We can immediately notice that at this step only one of the BPDs connected to the DAQ is receiving a signal. This choice has been intentionally made in order to have only one functioning channel to test the software that will elaborate the data. Once we are convinced that all the elaborations are functioning we will create channel B.
To conclude the lack of a second channel is not relevant at this phase since for a intensity image there is no needs for comparisons between different channels.

3.8.1.1 transmission or reflective reference arm

The main design choice to make is whether we are going to have a reference arm with a transmission or reflection configuration. These two option have some advantages that we will briefly cover.

Reflective arm

This solution for the reference arm make use of a single collimator and a mirror. The main advantage is that it uses less optical components; reducing the number of alignment and collimation operation needed. Decrease of intensity loss due to incorrect alignment should ideally improve the final image quality.

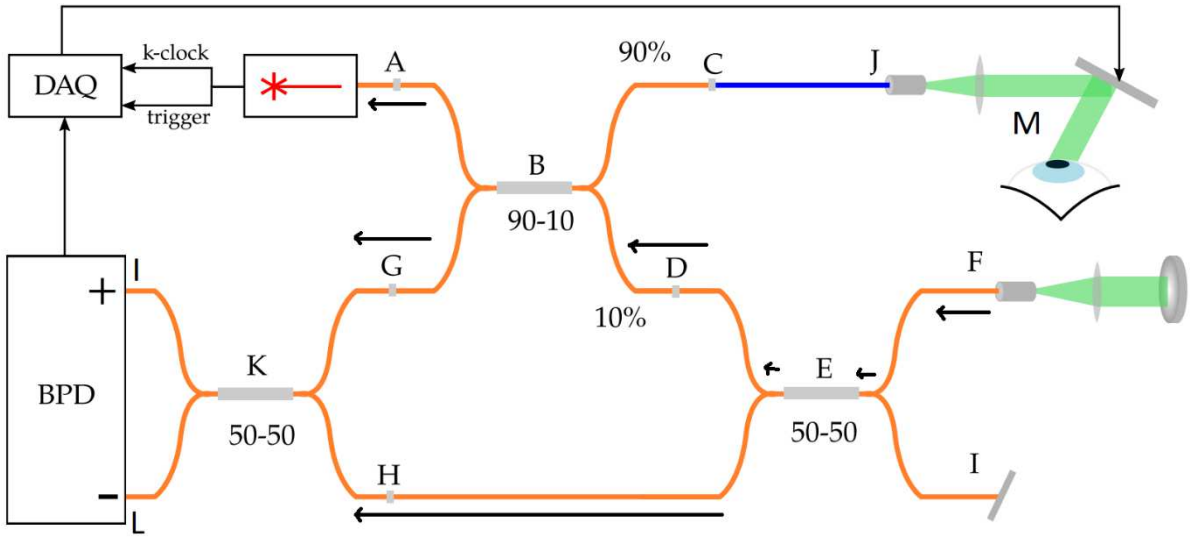

Figure 3.24: reflection reference arm configuration with the "spurio" component reaching the BPD

The drawback of this solution comes from the path the backscattered light will follow. As we can see from the arrows the reflected light is coupled back into the fiber reaching the coupler identified as 3. At this point half of the intensity will be correctly guided to the FPC while the other half will return to the first coupler reaching the laser and the BPD.
The presence of a copy of the reference light that will not undergo the polarization change is bound to produce errors when we will implement the polarization imaging functionalities. Also increasing the amount of light that will return to the laser may cause damage if the intensity increases to much (unlikely to happen in our case, but still not ideal).

These problems may be avoided making use of a circulator before the in air transition
As shown in Figure 3.28.

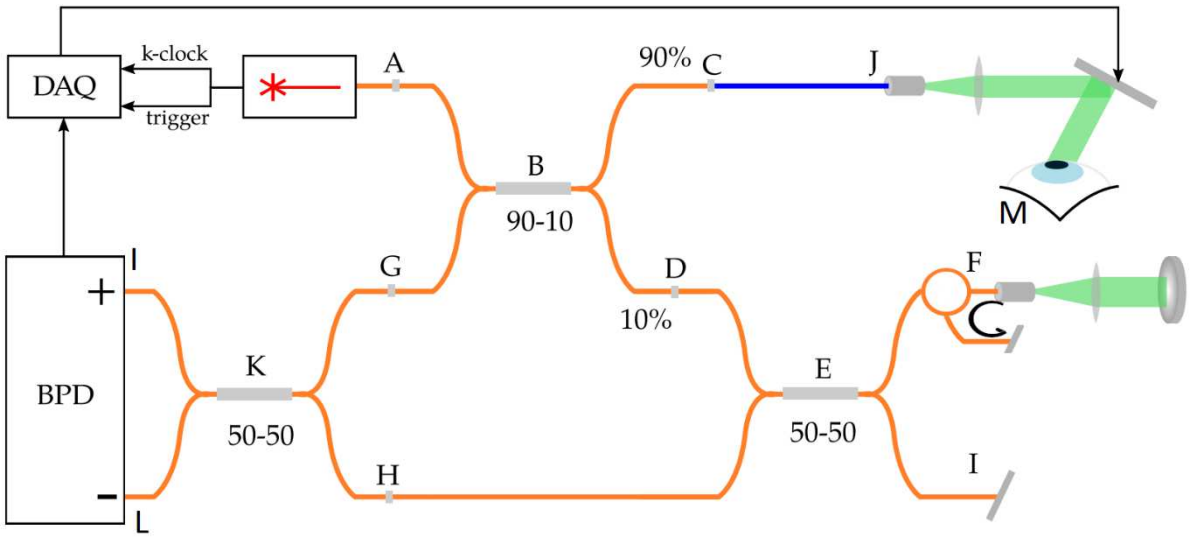

Figure 3.25: reflection reference arm configuration with circulator to avoid the "spurio component"

Transmissive arm

This is the configuration we picked for the reference arm. To realize the in air section, we need to make use of two collimators, to maximise the percentage of light intensity that is correctly sent through open air and coupled back into the fiber. Since we are making use of multiple collimators, it's more likely that we will not be able to collimate the light beam perfectly, hence significantly increase the loss of intensity during the transmission. The main advantage offered by this solution is that all the light directed to the reference arm will be guided to the FPC or completely loss. No copies of the reference signal are propagating into the sample arm. We do not need to worry for "spurio components" to affect the evaluation of Stokes vectors.

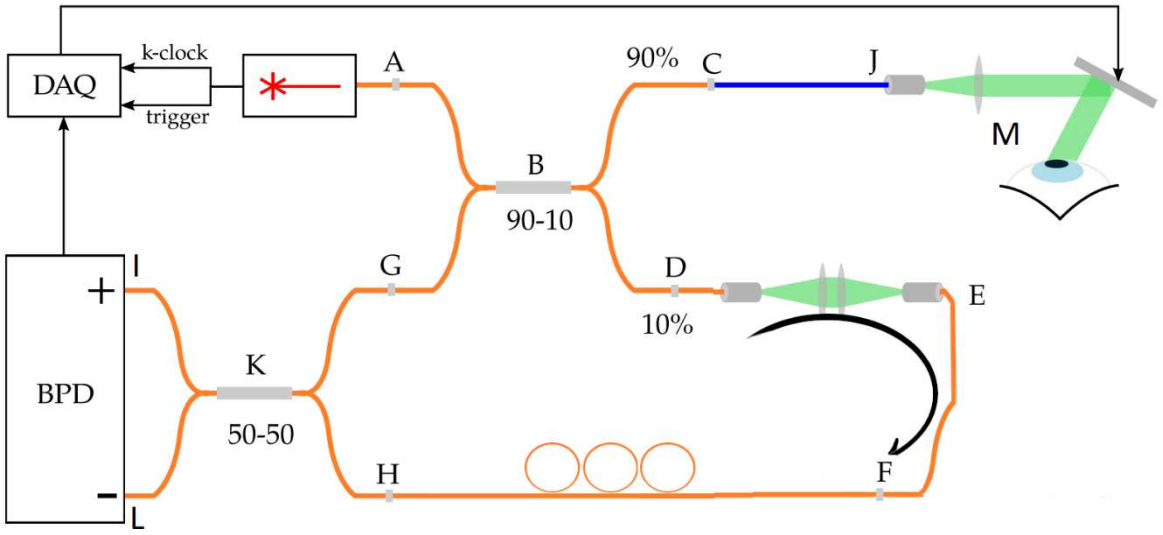

Figure 3.26: our transmission set up for OCT with arrow indicating the path of reference signal.

3.8.1.2 Balancing the optical paths

As we discuss in chapter 2 two beams of light from the same source will interfere only if their path difference is smaller than the coherence length. In the same chapter we also saw how the information for SS-OCT is encoded in the transform of the power spectral density of the interference image. We can conclude that it's essential that the optical path length difference (OPD) allows for the interference to take place($OPD < l_c$). If $OPD = 0$ that would lead to maximum visibility (section 2.2.4) which translate to a more define power spectral density profile and final image.

After the realization of the optical circuit in Figure 3.26, we can start taking measurements. Before starting we have to identify which segments will lead to OPD changes. Measuring the path before the reference and sampling beams are separated is pointless since it's common path.
The fiber segment to measure are:

- CJ: section of the sample arm traversed two times by the light;
- EH: section of the reference arm after the in air section;
- BD: section of reference arm before the transmission in air.

The other fiber segments belong to the couplers so the length can be recovered from the datasheet that Thorlabs provided.
The in air segments are:

- JM: in the sampling path space between the collimator that's the input of the sampling head and the actual sample. This has to be counted two times since there is also the reflection on the sample to consider.
- DE: is the in air segment between the collimator. It has to be counted only one time.

To evaluate 2M we have to take a look at the sampling head datasheet to recover the focus plane distance (this plane is the optimal location for samples to be located). We also have to consider the internal distances between mirrors and collimator.
2M components are:

- Parfocal distance: focus plane distance including the lens width.
- Pupil distance: distance between first mirror and collimator.
- Scanning distance: distance between the mirrors+ distance second mirror and focussing lens.

$$2M = d_{parafocal} + d_{pupil} + d_{scanning} \cong 17\ cm$$

While 3A3B is best to be kept variable in order to compensate possible path differences in the fiber sections.

For evaluating fiber segments length, we used an OFDR. This device sends a sweep source signal into the fiber and then listens to the backscattered light in order to produce a plot of backscattered intensity over distance (in the fiber). From the OFDR's plot we can recover the lengths by recognising the position of connectors and other component whenever strong reflections are found.
Using the OFDR in different position on the optical circuit we recovered the distances in Table 3.3.

Label	Refr. Indx	Meas. Geom.
AD	1,466	2,217
AC	1,466	2,217
AJ	1,466	3,25
JM	1	0,17
ADEK	1,466	6,546
DE	1	0,1
ADEK-DE	1,466	6,3994
AB	1,466	1,125
IKBJ	1,466	5,463
IKB	1,466	3,343
IK	1,466	1,095

Table 3.6: Table reporting the length of the segments and their refractive indexes.

The first column has the name of the point through which we are measuring. The second column has the reflective index of the segment; 1 if it's in air and 1.466 if in fiber. The last column has the length of the segment in meters.
Now that we recover the measurement we can first calculate the length in fiber of the two optical paths.

$$l_{sampling\ arm}^{fibber\ section} = 2 \cdot \overline{AJ} - \overline{AB} + \overline{IKB} - \overline{IK}$$
$$l_{sampling\ arm}^{air\ section} = 2 \cdot \overline{JM}$$

$$l_{reference\ arm}^{fibber\ section} == \overline{ADEK} - \overline{DE}$$
$$l_{reference\ arm}^{air\ section} = \overline{DE}$$

We can now evaluate the optical path difference with the following formula:

$$l_{sampling\ arm} = l_{sampling\ arm}^{fibber\ section} \cdot 1.466 + l_{sampling\ arm}^{air\ section} \cong 11.5153\ m$$
$$l_{reference\ arm} = l_{reference\ arm}^{fibber\ section} \cdot 1.466 + l_{reference\ arm}^{air\ section} \cong 11.5119\ m$$
$$OPD = \left| l_{reference\ arm} - l_{sampling\ arm} \right| \cong 0.0034\ m$$

The optical path difference we obtained is $3.4\ mm$ which is shorter than the coherence length $l_c = 12.3\ mm$.
We can now ensure that the two signals will interfere.

3.8.2 Implementation of software for OCT

Before starting we recall that the software piloting the DAQ for the acquisition of samples and transmission to the PC memory has been taken from the work of Marcon[1]. The only change we made is to the acquisition input range that have been changed to $\pm 400mV$. This variation has been made to increase the range of voltage levels used by the BPD's signals.
Also the GalvoControls software has been taken from the work of my predecessors Marcon and Calabrese.
Finally the graphic interface has been develop from visiaui.cpp that also comes from the works done in previous thesis. The interface has been adjust to enable the insertion of new parameters and functionalities.

The coding language used is C++. Since OCT applications have the necessity to use GPUs in order to allow real time generation of images, it has been required to study and use the CUDA libraries made by NVIDIA. These libraries allow the access to GPU's memory registers by allocating regions of memory in which we can copy data from the CPU's memory and vice versa. Another functionality of these libraries is the computation of Fast Fourier Transform (FFT) in a thread form; greatly reduce the computation time of this resource intensive operations.

Now we will cover the computation needed to obtain A-scans and B-scans from data acquired by the BPD associated to the A-channel.

3.8.2.1 transforming bits to useful data

The buffers we receive from the DAQ driver are arrays of ints that require to be converted to a more practical format. We will call the transfer data as Raw-data and they require to be converted into float values that describe the voltage level of the BPD's signals.

To start we have to know how the voltage levels are assigned. No matter the range selected the voltage levels will always be decoded into 16 bits. So the each sample received by the DAQ is described by a 2 bite binary number belonging in the range $[0, 2^{16} - 1] = [0{,}65535]$. Now we have to take into account the BPD setting in use. Recalling that the chosen for the output signal is $\pm 400\ mV$; this means that each voltage sampled will be encoded into the energy level n if it's contained in the range:

$$V_{BPD}\ \varepsilon \left(V_{level\ n} \pm \frac{400}{2^9}\right)\ mV = \left(n \cdot \frac{400}{2^8} \pm \frac{400}{2^9}\right)\ mV$$

Where $V_{level\ n}$ is the central voltage of the level and $\frac{400}{2^9} = \left|V_{level\ n} - V_{sampled}\right|$ is the maximum difference for a value of tension to be encoded in the n level.
Knowing this relation we can now convert the Raw-data into floats. We read the receive buffer in groups of 2 bites. We convert each group of 16 bits into its decimal counterpart in order to obtain an array of ns with:

$$n\ \varepsilon[0{,}65535]$$

Finally we have to convert each n into a float in order to recover the sampled tension $V_{sampled}$ using the formula:

$$V_{sampled} = (n - 2^8) \cdot \frac{400}{2^8} - \frac{400}{2^9}$$

Now we converted the Raw-data buffer into a buffer of floats that can be easily used.

We recall now that due to the DAQ software: each buffer (B-scan) is an array composed by 1250 records (A-scans), each composed by 1504 samples (this data comes from our analysis in the DAQ section at triggering subsection). This means that every buffer is composed by 1880000 samples (hence floats).
We will need to keep in mind this structure while making the elaborations on the single A-scans.

3.8.2.2 apply windowing and FFT

As we saw in chapter 2 in FD-OCT the information is encoded in the Fourier transform of the signal so it's necessary to evaluate the FFT.
Before doing so we have to remember that each buffer has to be subdivided into its record components. Luckily this subdivision can be easily been taken care of by the CUDAfftPlan object. the role of this object is that when using CUDAFFTR2C in order to evaluate the complex Fourier transform of a real signal, CUDA will be capable to correctly sections of the buffer containing samples belonging to the same record; this allows for the correct computation of A-scans.
CUDAfftPlan require as inputs the dimension of the buffer and that of the records in order to fragment the buffer during the FFT and rebuild it with the results of the FFT as its components.
Once we have verified the evaluation of the transform we decide to implement a windowing function to apply before the FFT will take place in order to improve the quality of the transform. To do so we added to the interface a drop down menu in which we can select which windowing function we intend to use. Once we select an option we will initialize a memory buffer in the GPU containing 1250 (number of records composing a buffer) times the selected windowing function composed by 1504 samples (same number of samples composing a record). If the windowing buffer has been initialized the program will automatically apply a cell per cell multiplication between the windowing buffer and the received buffer. In figure 3.30 there is an image of the drop down menu with the available windowing function.

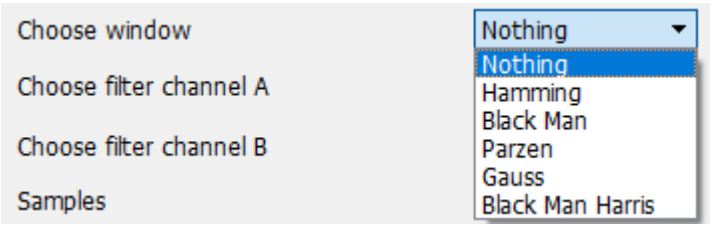

Figure 3.27: image of the windowing function drop down menu in the program interface.

The effect of the windowing function are minimal on the final images that will be produced. an example of an image with and without the windowing function will be available in figure 3.32 in section 3.9.2.3 in which we will also show how an image without compensation of various phenomena appears.

3.8.2.3 Creation of the image

Once we applied windowing, the FFT and dropped the negative frequencies. we have to evaluate the modulus of each of the complex number that identify the samples to obtain a float array describing the A-scans.
The last remaining step is to create the image. In order to do so we will use C++ texture methods.
Before starting the grey scale conversion, we have 2 sliders at the centre of the left column of the interface. These sliders are meant to set the minimum and maximum value of voltage (and hence intensity since it's proportional) in the A-scans that will correspond respectively to the pure black and white RGB.

Figure 3.28: sliders for the range of grey scale conversion.

Once set the values for which the colour will saturate, we can start the conversion. First we check for any value outside the range between the sliders. If any are found we will overwrite the cells with the upper threshold if the value is greater than the value of the max slider or with the lower threshold if the cell contain smaller values than that selected.
Finished this preliminary passage we can translate all the values of the buffer to a number between 0 and 1. This is archive by subtracting at each cell the lower threshold and then dividing the result by the difference between the thresholds.

For the creation of the texture we are once again making use of code made by Calabrese. His code generates a texture with heigh equal to the number of A-scans and length equal to the number of sample for A-scan (which is now 752 since we dropped the negative frequencies). The creation of the texture also needs to receive three 1250x752 matrix of 8 bits ints. Each matrix corresponds to a one colour between: red (r), blue(b) and green(g). Each cell has value between 0 and 255 indicating the intensity of the colour corresponding to the matrix considered. We will use these matrixes to assign at each of the pixels how much of each of the three colour they have to display.

Recalling that black in rgb correspond to r=0, b=0 and g=0 while bright white is r=255, b=255 and g=255. We can now produce the three colour matrix needed by Calabrese's code using the normalized buffer we produced and multiply it by 255. We will use a copy of the obtained

matrix for each of the colour matrix since we are interested in a grey scale image and in RGB grey is given by r=b=g.

Example of the images are in figure 3.32. We recall that we do not have any post processing for compensation of dispersion and other phenomena jet. The signal is highly degrades and so the image quality. Hence the image is not legible.

Figure 3.29: left image of single reflector (mirror) obtained without any chromatic compensation. On top there is the version with windowing apply; below without. As we said in subsection 3.9.2.2 the difference is barely visible; there are some noticeable differences at the edges of the image.

3.8.3 Chromatic dispersion

In figure 3.32 we see what a B-scan of a single mirror is for our system.
In theory each A-scan should be a single peak at the distance were the reflector is located; but we are seeing a series of peaks located near the reflector position.
We can attribute this degeneration of the signal to the various dispersions due to the propagation in fiber.
If we consider a plane EM wave propagating at the entrance of an optical fiber. it's formula is given by[4]:

$$\bar{e}(t) = \sum_{n=0} c_n \overline{E_n}\, e^{-j\beta_n(\omega+\omega_0)z}$$

Where the various term of the sums describes different propagating modes and z=0.
At the exit after propagating for a length l it's formula can be written as[4]:

$$\bar{e}(t) = \int_{-\infty}^{\infty} \sum_{n=0} c_n \overline{E_n}\, e^{-j\beta_n(\omega+\omega_0)l} e^{j\omega t}\, df$$

The term $\beta_n(\omega + \omega_0)$ can be develop in Taylor series as:

$$\beta_n(\omega + \omega_0) \approx \beta_{n,0} + \beta_{n,1}|\omega$$

Using this form of the β_n we reach the form[4]:

$$\bar{e}(t) = \sum_{n=0} c_n \overline{E_n}\, e^{-j\beta_{n,0}l}\, a(t - \beta_{n,1}l)$$

This form highlight the **Modal Dispersion.** This phenomena is due to the presence of multiple light modes propagating in the fiber core. Each of these modes are different replicas of the signal arriving at different times. The modal dispersion term is described by $\beta_{n,1}$.

The modal dispersion is already handled by the set up since we are using single mode fibers. these waveguides are characterised by having a core with such a small diameter that only the zero mode can exist within it. We know than this effect is not affecting our measurements.
If we further develop β (only one mode no need for pedicel) we have:

$$\beta(\omega + \omega_0) \approx \beta_0 + \beta_1|\omega + \frac{1}{2}\beta_2|\omega^2$$

The new coefficient β_2 is called: **Chromatic dispersion**. It is an effect characteristics of broadband signals and can be intuitively explained by subdividing the main broadband signal in multiple narrowband signals. Since the refractive index is wavelength dependent, each narrowband component has a different propagation constant and hence different delays. The effect of chromatic dispersion are dependent on the form of the signal and the band occupied. In our case since we will be looking on the spectral power the effects due to different propagation times is the decomposition of the original peaks in the true location of the reflector into multiple smaller peaks around the original position.
Chromatic dispersion is the culprit of the anomalies we saw in figure 3.32. To solve it we could use multiple approaches.
The first is to make use of chromatic dispersion compensating fibers. These special fibers have a negative β_2 and should be inserted on the different arms in order to cancel out the delays introduced by the normal fibers. The main advantage of this solution is that it doesn't require extra computations. This solution is dependent on the length of the normal fiber used hence if we need to modify the fiber paths we will need to re-evaluate the lengths of compensating fibers required to cancel the distortion. Since we intend to modify the set up in order to introduce the ability to measure the intensity based on the polarization state of the light this solution isn't ideal.

The second approach is a software solution to compensate the delays that the different frequencies face. we will now explain how we implemented this "filter".
First we have to remember that in SS-OCT each sample of an A-scan is sampling the interference of the sample and reference signals at a specific wavelength. Each sample contains information belonging to all the points of the object hit by the beam. We can then consider each A-scan as composed by 1504 channels each using a different wavelength and hence affected by different delays. Samples in different A-scans in the same position share the same delay.
We know that the effects in the spectral power density is a translation of the peak. From the property of the Fourier transform multiplying a signal by a factor $e^{-j\vartheta n}$ before using the FFT is equivalent to translate the transform. So in order to compensate the translation of the different peaks we need to modulate each sample using a factor $e^{-j\vartheta_n n}$ where the n index indicates the position of the sample inside the A-scan. Since each sample represent the interference signal for a specific λ_n; multiplying the a sample in position n by $e^{-j\vartheta_n n}$ will cause it's Fourier transform to translate the peak associated to a new position (ie wavelength/distance).

We need to find all the 1504 factors $e^{-j\vartheta_n}$ required to align the different peaks.

The step taken for the evaluation of the different $e^{-j\vartheta_n}$ are as follow:

1. We saved all the 1504 sample that compose an A-scan before applying the FFT on a file.
2. Load the file on MATLAB obtaining the vector $\bar{s}(k)$.
3. Apply the FFT to the loaded samples to obtain $\bar{S}(z)$.
4. Set to zero the negative positions and the first 50 sample in base band to cancel the non-interference term.
5. Find the position of the maximum. This will be the location in which the reflector is located.
6. Set to 0 each sample of $\bar{S}(z)$ with amplitude lower than 15% of the maximum. This step is meant to cancel the noise. Now we have obtained a filtered analytic signal.
7. All the samples of the analytic signals are complex numbers; so they can be written as $\rho_n e^{j\varphi_n}$ where n is the position index. We create a vector containing all the φ_n.
8. The phases of the samples are given by the formula:

$$\varphi_n(k) = \beta_0 + \beta_1|(kc) + \frac{1}{2}\beta_2|(kc)^2$$

   Where $k = \frac{2\pi}{\lambda_n}$ with $\lambda_n = \frac{2\pi nc}{df}$ the wavelength of the sample and $\frac{c}{df} = d\lambda$ is the difference of wavelength between two consecutive samples.

   We use the polynomial fit tool of MATLAB on the $\overline{\varphi(k)}$ in order to obtain an estimate of $\frac{1}{2}\beta_2 = \beta'_2$.
9. Now we calculate a vector $\overline{\vartheta(k)}$ with:

$$\vartheta_n(k) = \beta'_2(kc)^2 = \beta'_2\left(\frac{2\pi nc}{df}\right)^2 = \vartheta_n(n)$$

   Using our knowledge of df given by our configuration of the sampling clock; we are able to make an estimate of the phase shift each sample has received due to chromatic dispersion from the position of the sample inside the A-scan.
10. Now we can build our "filter" as a vector $\overline{h(k)}$ whit n component given by:

$$h_n = e^{-j\vartheta_n}$$

11. We now evaluate the analytic signal $\bar{H}(z)$ by doing the FFT on $\overline{h(k)}$ an then removing the negative positions.

12. Finally we move $\overline{H}(z)$ in baseband and then return to the original domain obtaining the final vector $\overline{h'}(k)$ which is our filter.

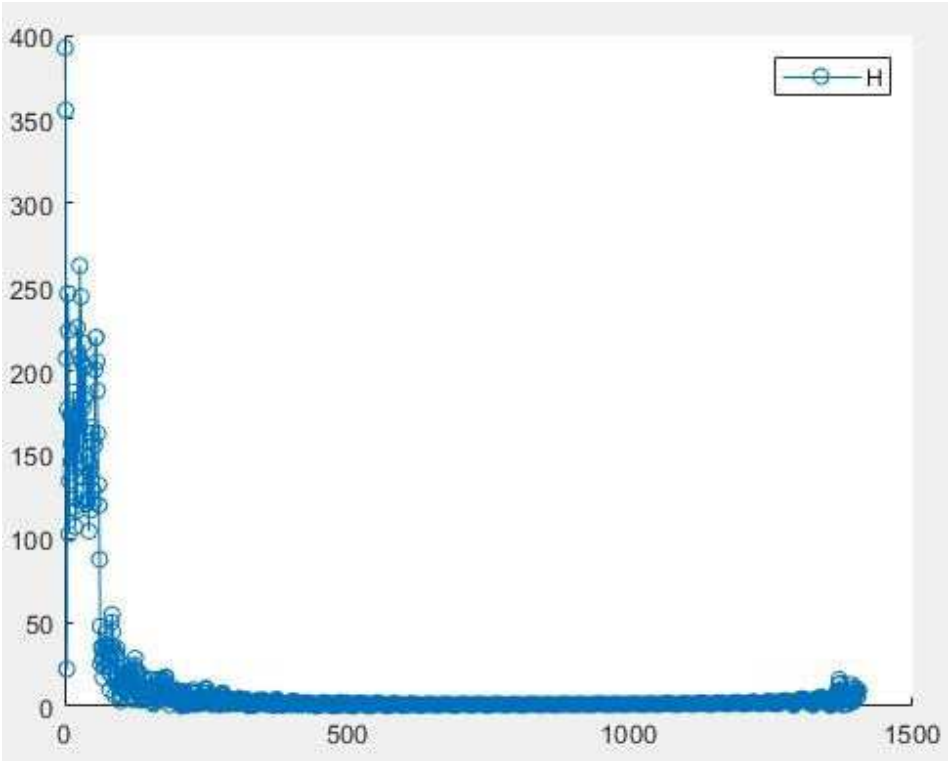

Figure 3.30: image of $\overline{H}(z)$ shifted in baseband.

We now have to test if our "filter" is correct by multiplying $\bar{s}(k)$ by the vector $\overline{h'}(k)$ before applying the FFT. Then apply the FFT in order to obtain $\overline{S'}(z) = FFT(\bar{s}(k)\overline{h'}(k))$
And confront $\overline{S'}(z)$ and $\bar{S}(z)$ in order to see if we manage to overlap the peaks.

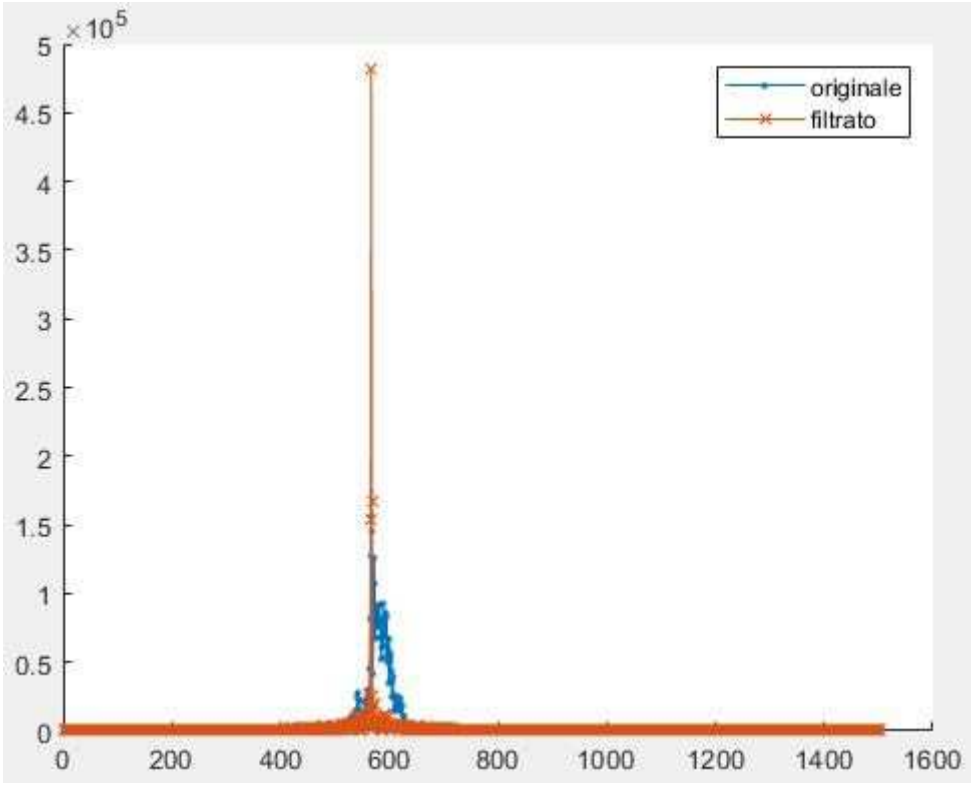

Figure 3.31: image of $\overline{S}(z)$ original transform of the samples and $\overline{S'}(z)$

As we can see our filter is a success since each h_n when multiplied to its corresponding s_n is able to compensate the phase shift introduced by the chromatic dispersion. The result after the FFT is the alignment of the peaks at the same position as we can see in figure 3.34.

We now save $\overline{h'}(k)$ on a file that needs to be load into the OCT's program by using the buttons on the left side of the UI.

Figure 3.32: buttons for loading the filter for channel A and B. it also shows the checkbox for applying the filters which is located at the very bottom of the column.

We have two buttons to choose a filter file, one for each of the channels. Once loaded we can use the check box in order to multiply all the received A-scans by the loaded $\overline{h'}(k)$ corresponding to the channel.

Here the final image obtained using the filter to cancel chromatic dispersion.

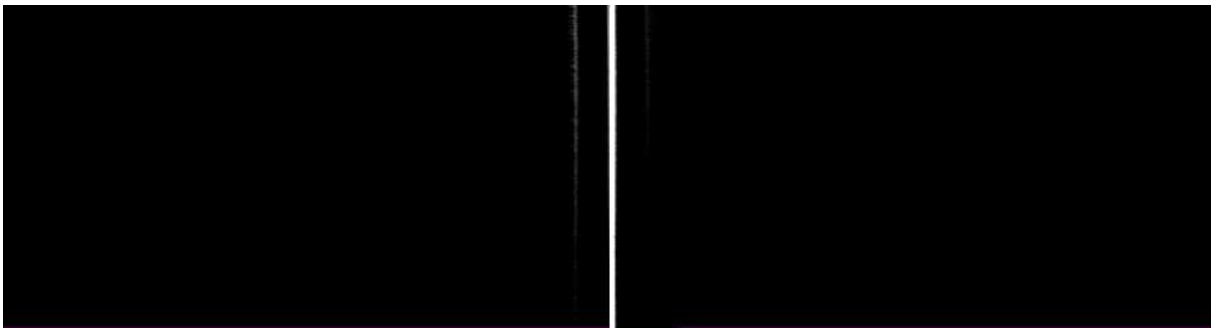

Figure 3.33: B-scan of a mirror applying chromatic compensation.

3.8.4 Galvanometric mirror correction

As we can see from figure 3.36 the surface of the reflector seems to be bent. This effect is caused by the change in path due to the mirrors changing inclination between A-scans to generate meaningful B-scans.
In order to correct this defect we will first explain how the mirrors are piloted. Then analyse the effects of having only one mirror moving at the time.
During all the analysis we assume the sample to be a perfectly flat mirror parallel to the focussing plain of the lens.

3.8.4.1 how the mirror are controlled

We first take a look to the galvocontrol programmed by Marcon interface in figure 3.37.

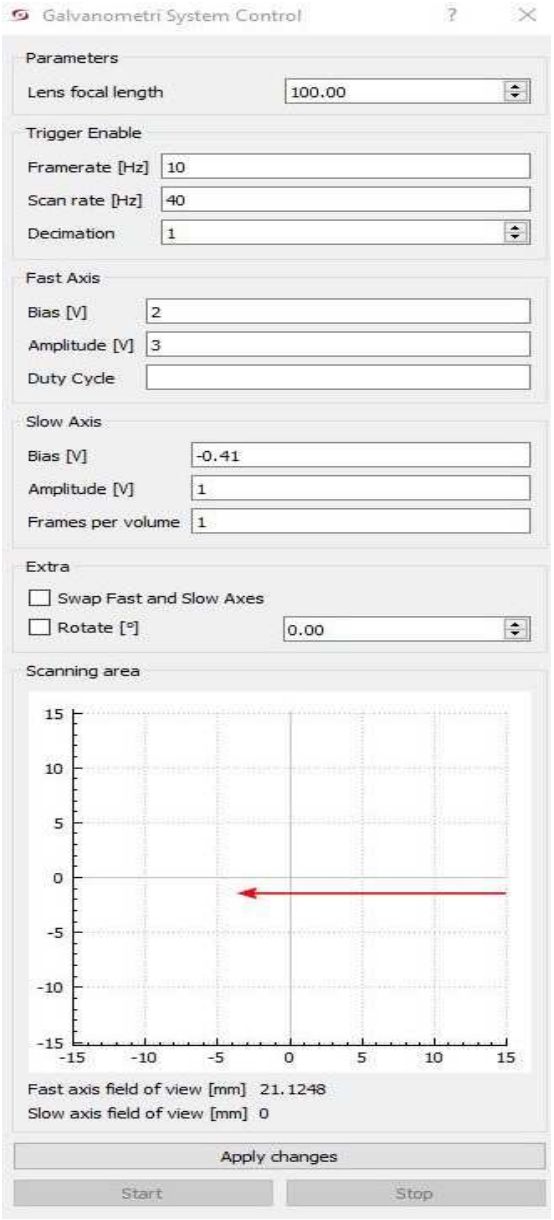

Figure 3.34: Galvo Control interface

As we can see each mirror has a Bias and an Amplitude voltage. Bias tension is normally at 0 V and is always applied to the mirror defining it's central position. Amplitude instead is defined as the maximum voltage that will be subtracted or added to the bias, defining how wide the scanning sweep is.

The voltage applied during the n^{th} A-scan on mirror $i = 1,2$ is given by:

$$V_{i,n} = Bias_i - Amplitude_i + Amplitude_i \cdot \frac{2n}{1250}$$

Where 1250 is the total number of A-scans for B-scans.

To conclude the tension on the first mirror defines the position on the y axes of the focal plane. While the tension on the second will define the position on the x axes. If we set $Bias_i = Amplitude_i = 0V$ we have an horizontal or vertical scanning. In all other cases the beam will move diagonally on the focal plane. If all the amplitudes are to 0V we will always acquire the same A-scan for 1250 times which is to avoid. The scanning direction appears in the plot at the foot of the interface visible in figure 3.37.

It's important that $|V_{2,n}| \leq |3.75|V$ since, as we saw in section 3.2, at these tensions we have the maximum impinging angle of the beam on the focussing lens for which the lenses do not introduce further deformation to the final image.

3.8.4.2 Only second mirror moves during acquisitions

In this scenario we have $Amplitude_1 = 0V$ so the position to which the beam impinges onto the second mirror (M_2) is the same at each acquisition.
Assuming that M_2 inclination changes are the only variable that determines the reflection angle, we can analyse the path variation within the acquisition of a single B-scan.
In figure 3.38 we have a schematics of how the scanning beam moves in time.

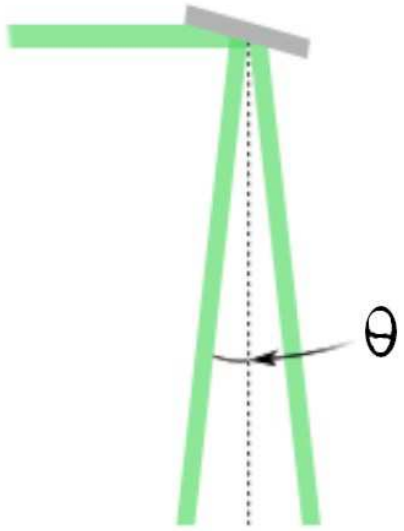

Figure 3.35: A schematic of the triangle space scanned by the beam between the second mirror and the focussing lens.

While the beam is scanning the sample to acquire a B-scan, it traces a triangle with heigh h.
We can immediately say that the A-scan acquired while M_2 is directing the light along h will have the minimum optical path.
From trigonometry we know that the hypotenuse a is given by the formula:

$$a = \frac{h}{\cos\theta}$$

Where ϑ is the angle between h and a. From this formula we can easily predict how the optical path length changes once we define h and θ. Both the parameter are easy to recover and we will discuss it on the implementation section.

3.8.4.3 Only first mirror moves during acquisitions

In this case $Amplitude_2 = 0V$ and the light beam will impinge in different points of M_2 at each acquisition time.
A schematic is presented in figure 3.39.

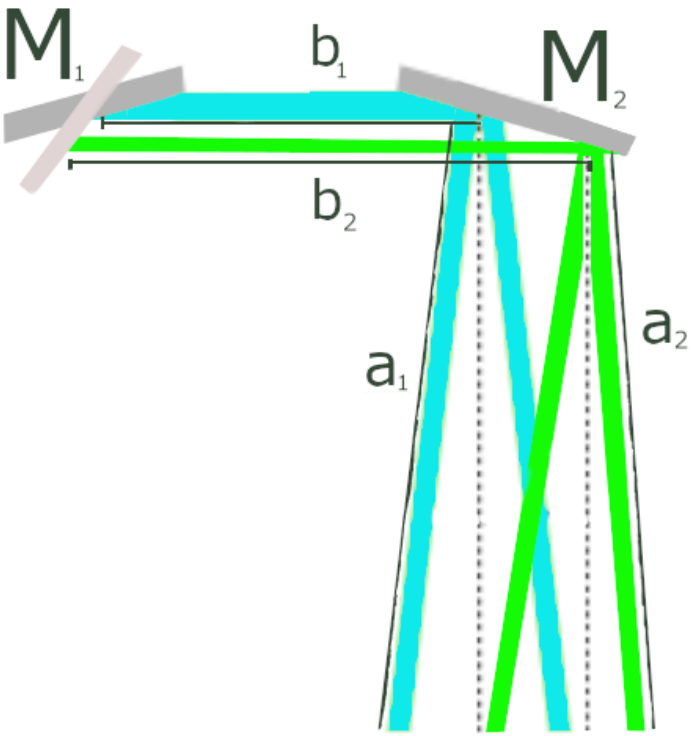

Figure 3.36: illustration on how the optical paths inside the sampling head changes as M_1 changes.

In the above image we can see that as the first mirror (M_1) tension changes, also the distances a and b will change.
In this case for two different A-scans composing the B-scan the optical path inside the sampling head has increased/decrease. So for any couple formed by the A-scans at position $i\ and\ j$ with $i \neq j$ the equation:

$$a_i + b_i = a_j + b_j$$

Is not necessarily respected creating a different type of curvature compared to the previous case.
This scenario is quite complex so using some approximations will be required. Our approximation is: changing M_1 inclination will leave θ mostly unaffected, hence we will consider it constant since $Amplitude_2 = 0V$.

Now we can take a look to figure 3.40 which is another representation of the model focussing on the distances.

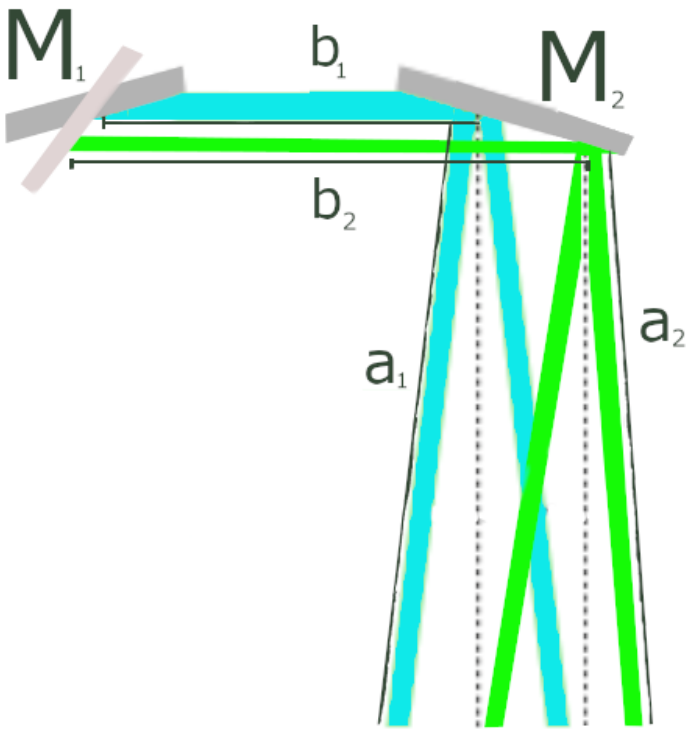

Figure 3.37: illustration on how the distances of the mirror changes as M_1 inclination evolves in time.

Assuming that the scanning has as its first A-scan the red beam and last the blue one.
We can show (using the same trigonometric rule of the previous sub-section) that for the n A-scan the distances will be given by:

$$b_n = \frac{B + D \cdot \frac{(1251 - n)}{1250}}{cos\varphi_n}$$

$$a_n = \frac{A + K \cdot \left|\frac{(1251 - n)}{1250} - 1\right|}{cos\theta_n}$$

Where B is the minimum distance between the mirrors and A is the minimum distance M_2 and the focussing lens. $K$is the maximum variation of $M_2 - lens$ distance while D is maximum variation of mirror distances.
Looking at the formulas we can see that as the A-scan index increases b_n will grow as a_n will decrease. The trade-off between the two optical paths is not enough to keep the overall optical path constant. We will make an estimator using MATLAB and some experimental data in order to predict the evolution of the parameters: $A, B, K and\ D$.

3.8.4.4 All mirrors moving during acquisition

In this case we will use the superposition of effects in order to estimate the optical path difference. First we use the model in 3.9.4.3 to estimate b_n and $A + K \cdot \left|\frac{(1251-n)}{1250} - 1\right| = h$. After this step we will apply the formula in 3.9.4.2 using as h the $M_2 - lens$ distance estimated by the previous step.

3.8.4.5 Implementation of the models in the program

At first we need to apply the chromatic dispersion to the A-scans in order to visualize the "bent" surface of the reflector. Once the image has been created we will use the horizontal pointer to select the A-scan at the centre of the curvature. At this point on the left column there is a drop down menu on which we have to select the Automatic option.

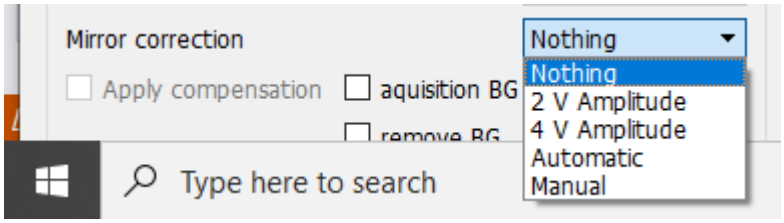

Figure 3.38: mirror correction menu.

The effect of the automatic option are as follow.

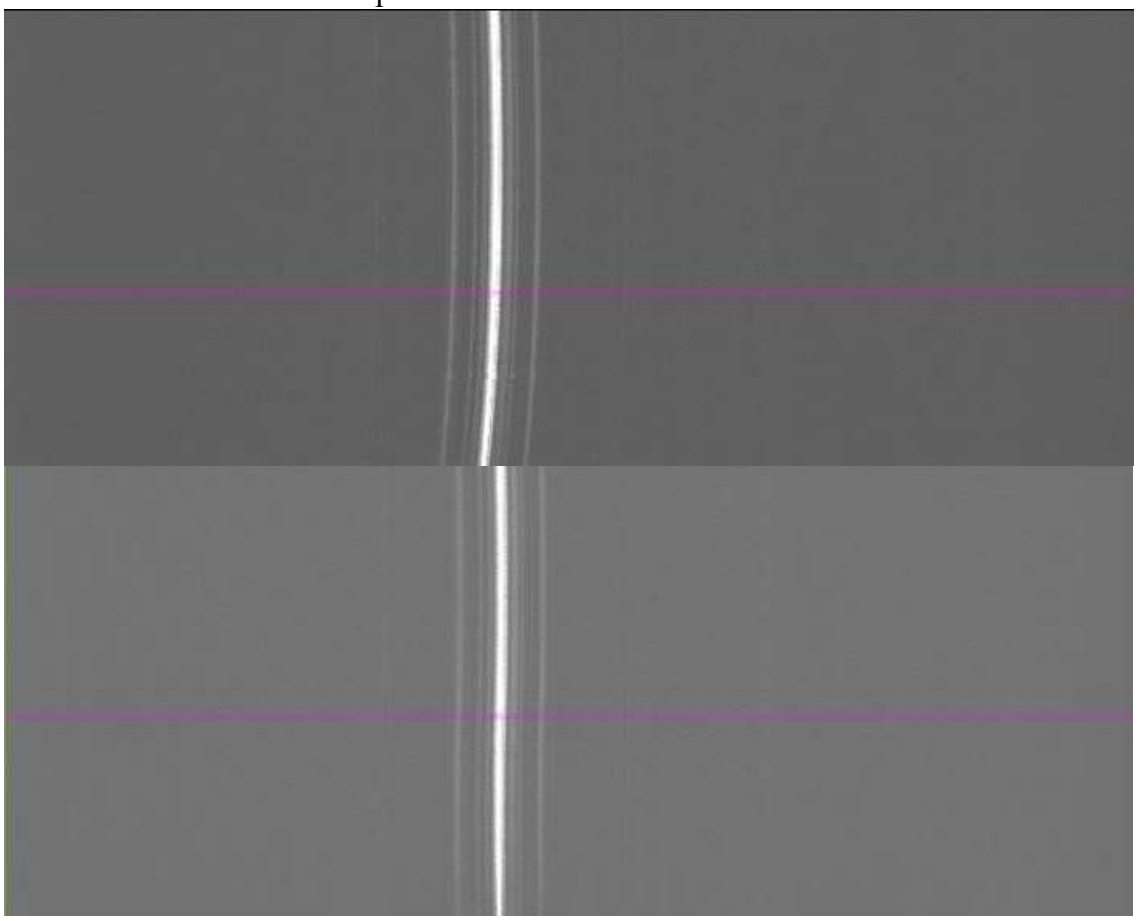

Figure 3.39: before (top) and after (bottom) the correction of the mirror curvature using the automatic option

We will now discuss what elaboration have been made by the program.

First the program controls the amplitude of M_1.

If it's zero we are in the **3.9.4.2 case**. In this scenario we only consider the M_2 amplitude since it will define the angle between the first and the last beam of the sweep.

$$sweep\ angle = \gamma = 2 \cdot Amplitude_{M_2}\ V \cdot 1\ {}^{\circ}/_{V}$$

Now using the A-scan pointer we set, the index of the selected A-scan can be recovered.

From this index we can evaluate h in pixels by looking for the position of the maximum amplitude in the selected A-scan.

Having the index of the curvature centre (n_c) we can evaluate the angle difference between the curvature centre and all the other A-scans. This allow us to evaluating how the mirror distance (in pixel) changes.

For the generic A-scan in position n the distance is given by:

$$a_n = \frac{h}{\cos\left(\frac{\gamma \cdot (n - n_c)}{1249}\right)}$$

So the distance variation in pixel is given by:

$$\Delta a_n = a_n - h$$

Now use the function round on Δa_n in order to decide how many pixel to the right (if positive left if negative) we have to shift each A-scan.

Below we have a plot created on MATLAB. To generate this plot we have saved the image before applying the mirror correction and loaded it into MATLAB. At this point we create a vector containing the position of the maximum amplitude for each A-scan. Feed the vector to a polynomial fit in order to approximate how the mirror distance actually change in function of the A-scan index. Once obtained the fitted vector we subtract to each cell the minimum value in the vector in order to evaluate of how many pixels the maximum moves in each A-scan. We now load the vector produced by our C++ code that estimate the pixel shift required (before the round step) and plot the two vectors. On the x-axes the A-scan index; on the y-axes the shift required in pixels to align all the maximum amplitudes.

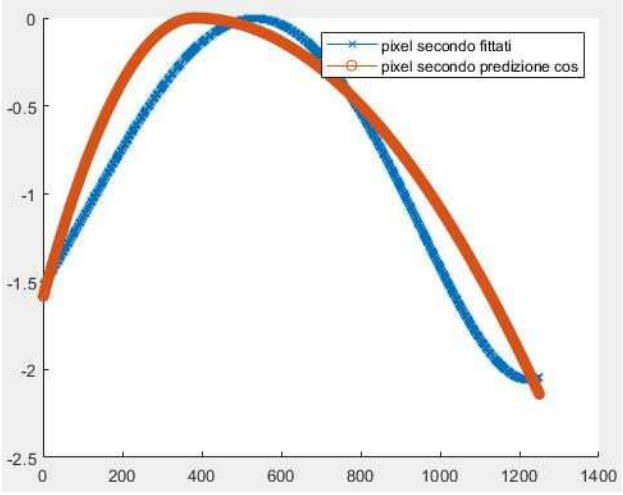

Figure 3.40: orange pixel shift estimated in C++; blue actual variation in pixel of the maximum found on the original B-scan

From the figure 3.43 we can see that the error in our Automatic function estimated shift and the actual shift of the maximum position recovered using MATLAB is within 1 pixel. To conclude this scenario can be handled without leaving noticeable curvatures.

In the case the amplitude of $\boldsymbol{M_1}$ **is non zero** we first apply the m**odel in section 3.9.4.3**.
In this case by using the information we have we can recover:

- Using coefficients estimated on MATLAB with the tensions amplitude and bias of the mirrors we can estimate B and A.
- Using the tensions on M_1 we can recover all the angles φ_n for each A-scan
- Using the tensions on M_2 we can recover all the angles θ_n for each A-scan

Now we check if amplitude M_2 is zero. If it is the reflection angle on the second mirror θ can be consider constant for all the A-scans.
In order to evaluate D and K we have to take the following step:

1. From the first A-scan evaluate: $b_1 + a_1 = d_1 = \frac{B+D}{cos\varphi_1} + \frac{A}{cos\theta}$
2. From the last A-scan evaluate: $b_{1250} + a_{1250} = d_{1250} = \frac{B}{cos\varphi_{1250}} + \frac{A+K}{cos\theta}$
3. using the values estimated for B and A and calculating φ_n and $\theta_n = \theta$ from the tension applied to the mirrors at the time of acquisition, only D and K are unknown. We have a two equation system with two unknowns
4. Solve the system and recover K and D.

Now we have all the parameter: $A, B, D\ and\ K$ (in pixels) we just need to apply the formulas for $b_n + a_n = d_n$. Once we evaluated all the d_n and insert them into $\bar{d}$.We subtract the minimum value d_{min} to all the element of the vector $\bar{d}$. We apply the round function to all the elements of $\bar{d}$ obtaining the amount of pixel shifts required to align the maximum.
If amplitude M_2 is not zero we can repeat the previous step and change $\theta \rightarrow \theta_n$. The main difference in this case is that the error in the estimation of the shift is larger especially if the tensions modulus on M_1 are above 4V.

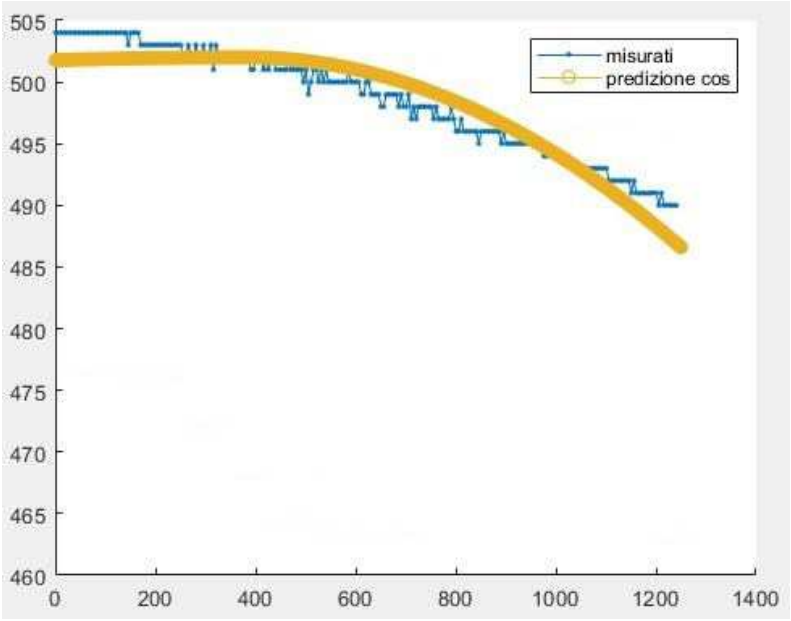

Figure 3.41: blue the position of the maximum in each A-scan evaluated on MATLAB. Yellow our prediction of the maximum position. In this image we have for M_1 amplitude 1V bias 2V while M_2 has amplitude 2V bias 2V.

The Automatic option in mirror correction is recommended when eider M_1 amplitude is zero or the tensions piloting M_1 does not exceed 4V. as for the tensions on M_2 it should not have a modulus above 3.75V otherwise the lenses will also introduce a curvature due to the incident angle being outside the acceptance cone.

Due to Automatic option on the mirror correction not completely compensating the curvature in some cases the Manual option has been created.
This option require the use of a MATLAB external program called *mirror_detection.m* and two support files: *mirror_detection.oct* and *mirror_correction.txt*.
If when selected the option Manual mirror_detection.txt does exist the file will be loaded to create a vector containing the pixel shift for each A-scan. after loading the file it will be cancelled. If *mirror_detection.m* can't be found, the program will save the A-scan in a file called *mirror_detection.oct*. at this point we have to run the MATLAB code manually in order to generate *mirror_detection.txt*.
What the MATLAB code does is:

- Load the data in *mirror_detection.oct*.
- Find all the maximum position for each row and save the positions in a vector.
- Subtract to the vector it's minimum value.
- Save the vector in *mirror_detection.txt*.
- Delete *mirror_detection.oct*.

The Manual option is always effective but require some seconds for the loading of the files and require the user to actively run the .m code.

The other option in the mirror correction menu are to correct common settings for the galvanometric mirror. These options will load txt files containing shift vectors created by using *mirror_detection.m* to which we change name. these file exist to avoid the need of using Manual and having to run *mirror_detection.m* each time or using Automatic and be required to slide the A-scan cursor to the centre of the mirror curvature.

3.8.4.6 Mirror correction coefficient evaluation.

The coefficient used in the Automatic function have been obtain using MATLAB and elaborating multiple images acquired from the OCT on a single mirror.

Before starting it's important to clarify that when we take an A-scan from the single mirror images; the position of the maximum (ie the distance of the mirror) is the optical path difference (OPD) between the arms. This means that when the path inside the sampling head increases then the optical path difference actually reduces hence the mirror will appear closer. The distance in pixel in the pictures is actually inversely proportional to path length inside the head of the device.
Since the mirror distance (in pixel) in the n A-scan is actually given by:

$$OPD - \Delta b_n - \Delta a_n$$

When we consider the images we have to remove the OPT part. To correct the curvature we are interested in tracking only the second and third component since these are dependent on the mirrors inclination. In order to correctly estimate coefficients for predicting Δb_n and Δa_n is essential that all the images have the same OPD component; to ensure that, we fixed the reference arm distance and the heigh of the sampling head for all the images taken.

First step is to estimate OPD. This has been done by acquiring an A-scan while all the tensions and the bias are zeros. In this scenario the in air section of the sampling arm is ensured to be $17\ cm$ as reported in the datasheet of the sampling head and our estimation in section 3.9.1.2. this image will not present any curvature since the mirror parameters are null. Using any A-scan from this picture we can obtain $OPD = 504\ px$. Now we can isolate the important components. For an A-scan n taken the OPD variation due to the mirror inclination is given by:

$$OPD - (OPD - \Delta b_n - \Delta a_n) = \Delta b_n + \Delta a_n = \Delta d_n$$

Evaluation of the coefficient for case 3.9.4.2. In this scenario only M_2 is changing inclination during the acquisition of the B-scan.

Our assumption are three:

- reflection angle changes are only dependent on M_2 variations of inclination.
- The changes $\Delta b_n + \Delta a_n$ are to be attributed to a change of h which is the distance between the focussing lens and the point of M_2 with the impinging light. This means that all the ΔD variations will be absorbed in the ΔH estimated.
- When 0V are applied to M_2 the reflected beam is normal to the lenses.

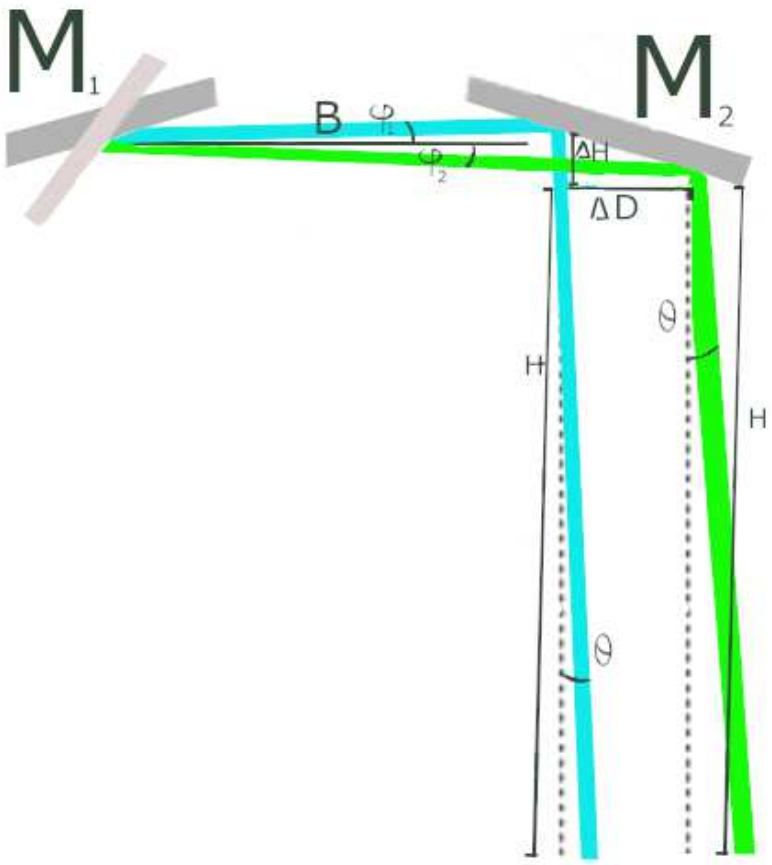

Figure 3.42: how h evolves as M_1 inclination changes

We can estimate θ defined as the angle between the heigh of the triangle and the beam direction used for the n A-scan with the formula:

$$\theta_n = V_n \cdot \alpha$$

Where $\alpha = 1\ °/V$ the degree per volt inclination applied to M_2.

We have to evaluate H height of the scanning triangle when bias M_1 is 0. To do so we use a B-scan with the following tension:

- Bias $M_2 = 0V$
- Amplitude $M_2 = 3.75V$
- Bias $M_1 = 0V$
- Amplitude $M_1 = 0V$

During the first and last A-scan on M_2 the tensions is $\pm\ 3.75V$ (corresponding to maximum acceptance angles for the focussing lens). Since the range of tensions used in the B-scan contain 0V there is an A-scan with $\Delta b_n + \Delta a_n = \Delta d_n = 0$ and is the central one ($n_r = 625$).

$$\theta_{1/1250} = \pm\ 3.75V \cdot 1\ °/V = \pm\ 3.75°$$

From the first A-scan we evaluate $\Delta d_1$and using the model formula in section 3.9.4.2:

$$H = \Delta d_n \cdot \cos\theta_1$$

We repeat the procedure used to evaluate H using 6 images. Assuming that the image used in position i has for settings:

- Bias $M_2 = 0V$
- Amplitude $M_2 = 3.75V$
- Bias $M_1 = (i-3)1V$
- Amplitude $M_1 = 0V$

Repeating the procedure should have given us 6 h_i whit $i = 1,2,..,6$. We evaluate now:

$$\Delta h_i = h_i - H$$

We use the Δh_i and their associated Bias M_1 to create a polynomial fit to estimate how h evolves for different tension on M_1. The coefficient have then been copy into the C++ mirror correction methods. From experimental test it results that estimation of h purely on Bias M_1 are enough to correct the curvature as long as the tensions apply to the mirrors at any given time are within $\pm\ 3.75V$ as the focussing lens require. We can stop here for this simplified case.

Consider now the **case 3.9.4.3.** Only M_1 is moving during A-scans. The assumption are:

- reflection angle changes are only dependent on M_1 variations of inclination.

- The changes $\Delta b_n + \Delta a_n$ are to be attributed to a change of h and to an increase of ΔD due to the inclination of M_2. To conclude the distance between M_1 and the plane orthogonal to the focussing lens and containing the heigh h is given by:

$$B + \Delta D_n = B + \frac{D(n-1)}{1249}$$

  Where D is the maximum ΔD between two A-scans belonging to the acquired B-scan
- When 0V are applied to M_2 the reflected beam is parallel to h.
- When 0V are applied to M_1 the reflected beam is parallel to B.

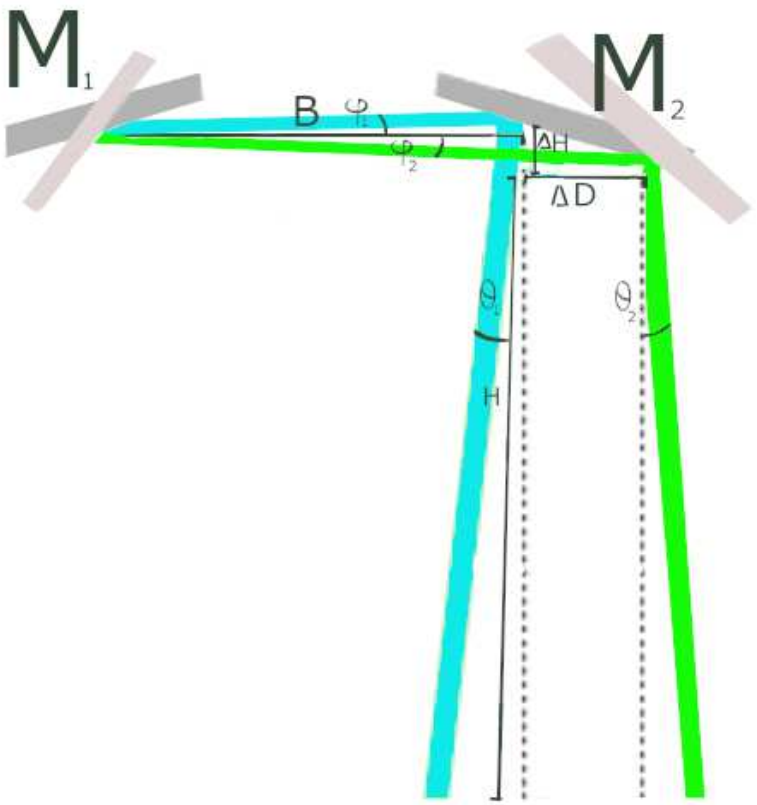

Figure 3.43: how h *and* $B + \Delta D_n$ evolves as M_2 and M_1 inclination changes.

To evaluate a predictor for B we will need a multiple images each identified by an $i = 1,2, \dots ,7$. The tensions used in the image i are:

- Bias $M_2 = (i - 4.75)V$
- Amplitude $M_2 = 0V$
- Bias $M_1 = 0V$
- Amplitude $M_1 = \pm 4V$

The angle φ_n angle between the segment B and the direction of b_n. Can be calculated as:

$$\varphi_n = V_n^{M_1} \cdot \alpha$$

While $\theta_n = \theta_i$ is constant for all A-scans belonging to the i^{th} B-scan. And is calculated as:

$$\theta_i = \theta_n = V_n^{M_2} \cdot \alpha$$

For each of the images we will follow these steps:

1. Evaluate θ_i.
2. Evaluate φ_1 and φ_{1250}.
3. From the first and last A-scan recover $d_{i,1}$ and $d_{i,1250}$
4. Using the coefficients calculated for case 3.9.4.2 (the previous model) evaluate h_1 and h_{1250} using as tensions $V_1^{M_1}$ and $V_{1250}^{M_1}$.
5. We can now estimate $a_{i,n} = \frac{h_n}{\cos\theta_i}$ hence recover $b_{i,1}$ and $b_{i,1250}$ from the formula:

$$b_{i,n} = d_{i,n} - a_{i,n} = d_{i,n} - \frac{h_n}{\cos\theta_i}$$

6. Evaluate $D_i = \left| b_{i,1250}\cos\theta_{i,1250} - b_{i,1}\cos\theta_{i,1} \right|$;
7. From $b_{i,n}$ we can evaluate B_i using the formula:

$$b_{i,n} = \frac{B_i + \Delta D_{i,n}}{\cos\varphi_n} = \frac{B_i + \frac{D_i(n-1)}{1249}}{\cos\varphi_n}$$

8. Save B_i in a 7 cell vector in position i.

Once we gathered all the B_i we use them with $V_i^{M_2}$ as inputs for a polynomial fit. The resulting coefficients are transcribed into the C++ code for the mirror correction. This last series of coefficients are used to produce an estimate of B_i starting from $V_i^{M_2}$.

Now we will use the last scenario to simulate what the Automatic mirror correction function does in MATLAB.

We will refer to the coefficient used to estimate h as :c_0,c_1, c_2, c_3, c_4 so:

$$h_n = c_0 + c_1 V_n^{M_1} + c_2 V_n^{M_1{}^2} + c_3 V_n^{M_1{}^3} + c_4 V_n^{M_1{}^4}$$

We will name w_0,w_1, w_2, w_3, w_4, , w_5 the coefficients used to evaluate , B:

$$B_n = w_0 + w_1 V_n^{M_2} + w_2 V_n^{M_2{}^2} + w_3 V_n^{M_2{}^3} + w_4 V_n^{M_2{}^4}$$

First step estimate h_1 and h_{1250} by using:

$$V_1^{M_1} = Amplitude_{M_1} + Bias_{M_1}$$

$$V_{1250}^{M_1} = Bias_{M_1} - Amplitude_{M_1}$$

Estimate K maximum variation of h between two A-scans so that:

$$K = h_1 - h_{1250}$$

$$h_n = h_{1250} + \frac{K(1250 - n)}{1249}$$

$$a_n = \frac{h_n}{\cos\theta_n}$$

We now have to estimate D. We calculate the position of the maximum in the first A-scan d_1 and in the last d_{1250} then we recover D from:

$$b_1 = d_1 - a_1 = d_1 - \frac{h_1}{\cos\theta_1} = \frac{B}{\cos\varphi_1}$$

$$b_{1250} = d_{1250} - a_{1250} = d_{1250} - \frac{h_{1250}}{\cos\theta_{1250}} = \frac{B + D}{\cos\varphi_{1250}}$$

The angles φ and θ evaluated from the mirror tension at the time of A-scan acquisition as done in the previous cases. B is evaluated using the w coefficients with $V_1^{M_2}$ (maximum tension for the A-scans on M_2). Once we recover D we can now write b_n as:

$$b_n = \frac{B + \frac{D(n-1)}{1249}}{\cos\varphi_n}$$

We can now estimate the pixel shift required for the A-scan in position n to align its maximum to the maximum of the referment A-scan in position $n_r$doing:

$$\Delta d_n = d_n - d_{n_r}$$

Since the Δd_n is usually decimal it will be required to apply the round function.

$$p_{shift,n} = pixel\ shift\ required = round(\Delta d_n)$$

We can check the results by evaluating the actual pixel shift required to align the maximum.

We first create a vector containing all the positions of the maximum of each A-scan. Then we subtract to each cell the value contained on the cell with index n_r. We have now a vector $\overline{p_{actual}}$. Then we compile the estimated $p_{shift,n}$ into a $\overline{p_{shift}}$. We plot the two vectors and then we plot $\overline{p_{actual}} - \overline{p_{shift}}$ to have an estimate of the errors.

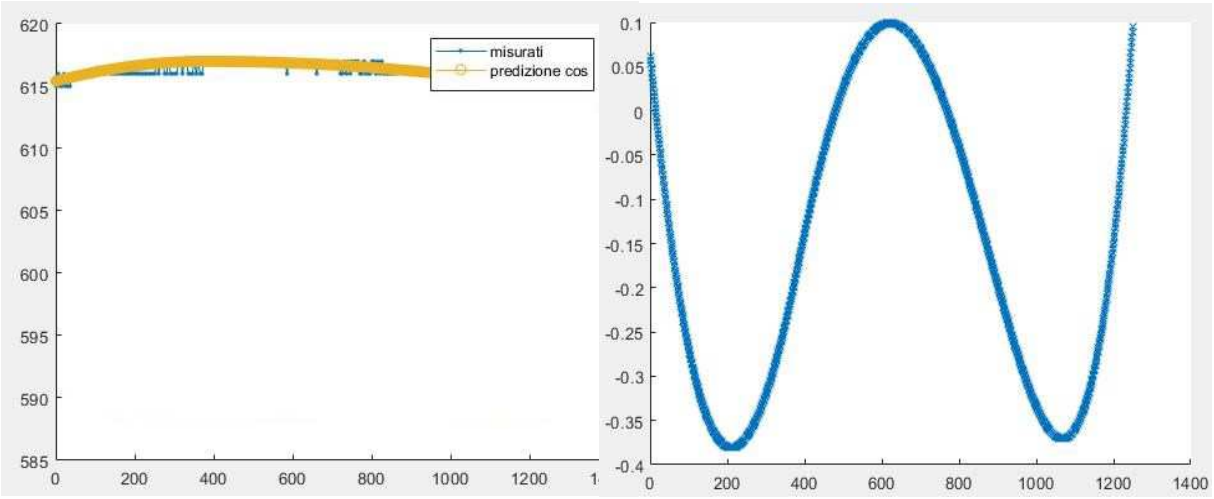

Figure 3.44: plot reporting actual maximum position and estimated ones on the left. At their side plot of the difference between the two functions on the left to visualize the error in the taking.

3.8.5 Background removal

As in all signal processing the removal of background noises will help to increase the image quality since it reduce the contribution of environment components.
In our program we introduce two functions for the implementation. Each of these functions are associated to a checkbox on the bottom of the left column.

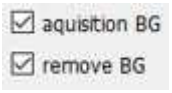

Figure 3.45: Background acquisition and removal checkbox.

The first method is **background acquisition**. When the checkbox is checked the program will save the B-scan in signal form currently display before the FFT take place, but after the application of: windowing, chromatic filter, mirrors and channels alignment frequency shift (this is a functionality implemented in chapter 4).
Once the B-scan is acquired we simply evaluate the average A-scan that will be saved in a new background register in the GPU.

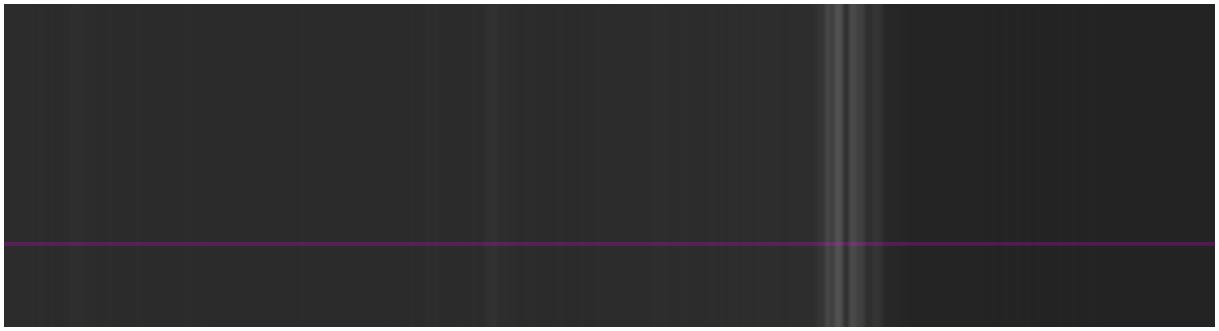

Figure 3.46: average A-scan repeated 1250 times in order to create the average B-scan noise image. it's just a visual way to evaluate whether the average A-scan has been correctly calculated

Finally the last method is **background removal**. When the checkbox is activated the program, after the acquisition and filtering of each A-scans collected, will subtract the background register.

To recap these checkboxes have to be used after the configuration of all other filters: windowing, chromatic filter, mirrors and channels alignment frequency shift.
Once we picked all other parameters and applied them (compensation checkbox active) we can activate the acquisition box and then the removal box. Only at this point we can place an object under the sampling head in order to correctly generate images.

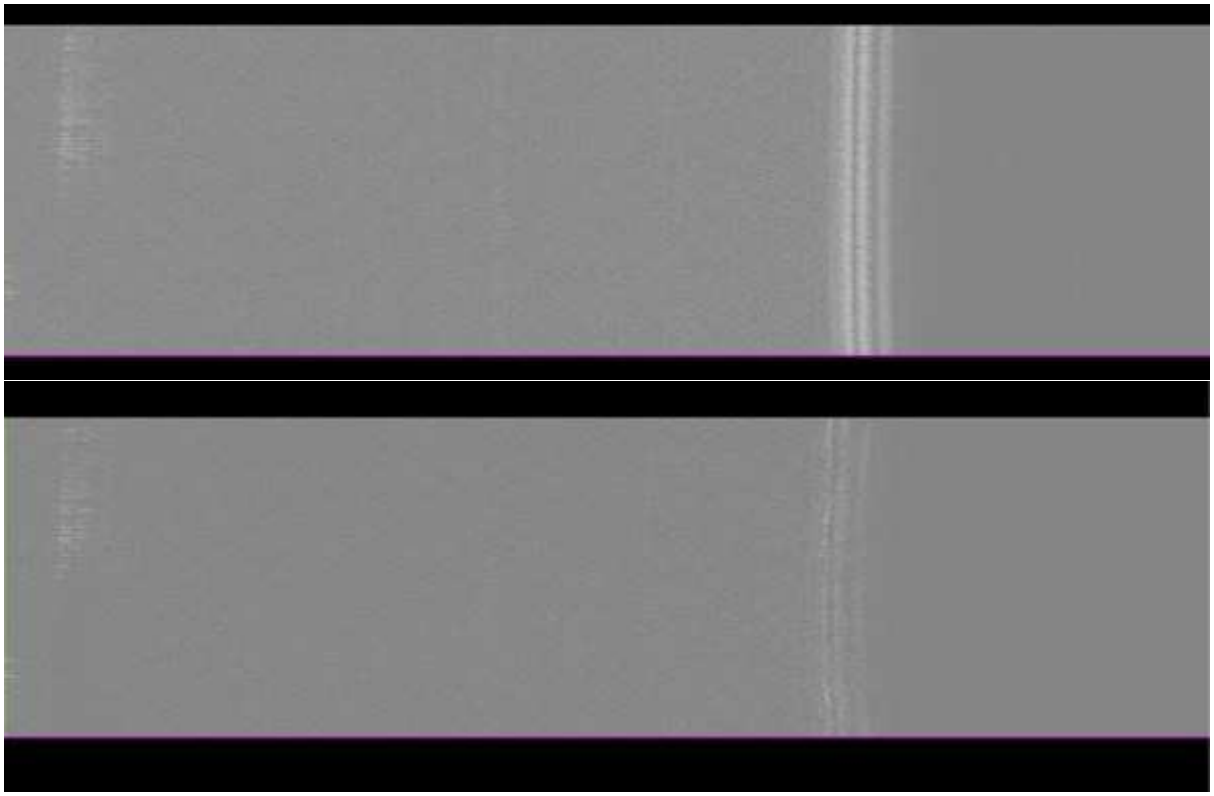

Figure 3.47: image from the OCT with nothing under the sampling head. top image display the image before background removal while bottom image is after.

As we can see the background noises are not completely solved, but still much less noticeable.

CHAPTER 4: Polarization sensing

4.1 Light polarization

In general the polarization of a wave is the direction in which the oscillation take place. Since in EM waves we have two orthogonal waves the polarization is given by the direction of oscillation of the electric field.

The polarization of EM waves is called linear if it oscillates in only one direction. If the direction of oscillation changes at a constant rate; it's either a left hand side polarization (counter-clock-wise) or right hand polarization (clock-wise).In the case of clock/counter-clock polarization we can further divide the two categories[5]:

- **Elliptically polarized**: if the amplitude of the electric field changes during the rotation.
- **Circularly polarized**: if amplitude stays constant.

Any other cases is eighter partially or completely unpolarized.

4.1.1 Polarization ellipse

For fully polarized light we can draw an ellipse by collapsing on the transverse plane all the positions occupied in time by the electric field $\bar{e}$.

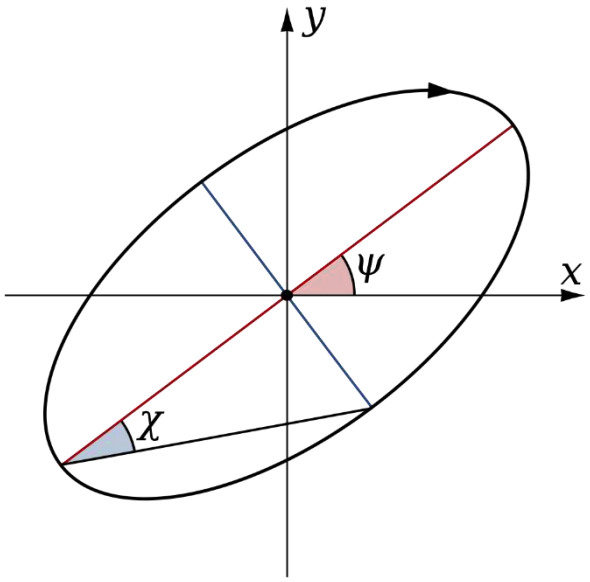

Figure 4.1: polarization ellipse generated by the rotation of $\bar{e}$ on the transverse plane.

The parameters that define the ellipse are[5]:

- $\boldsymbol{\psi}$ **orientation angle**: angle between the x axes and the major axes.
- $\boldsymbol{\varepsilon}$ **ellipticity**: ratio of the major to minor axes.

Another possible parametrization can be given whit[5]:

- **eccentricity**: $e = \sqrt{1 - \varepsilon^{-2}}$
- **ellipticity angle**: defined as $\chi = \tan^{-1}\frac{1}{\varepsilon}$

this later parametrization is important for the Poicarè sphere as we will see. Linear polarization correspond to $\varepsilon = \pm\infty$. Circular polarization is found for $\varepsilon = 1$ while

$$\chi = \begin{cases} 0° & right\ handed \\ 45° & left\ handed \end{cases}$$

4.1.2 Jones vector

In general for a completely polarized transverse EM waves to evaluate the polarization we consider the plane on which the electric and magnetic waves lays. On this plane we take two orthogonal direction and we evaluate the fields $\overline{E_{//}}$ and $\overline{E_{\perp}}$ projections of $\bar{E}$ on the selected directions. With these fields we can define the Jones vector which describes the polarization of the light[26].

$$\bar{e} = \begin{pmatrix} E_{//} \\ E_{\perp} \end{pmatrix} = \begin{pmatrix} a_{//} e^{i\vartheta_{//}} \\ a_{\perp} e^{i\vartheta_{\perp}} \end{pmatrix}$$

Where $a_{//}$ and $a_{\perp}$ are the amplitudes of the fields while $\vartheta_{\perp}$ and $\vartheta_{//}$ are their phases. Multiplying $\overline{E_{//}}$ and $\overline{E_{\perp}}$ by any complex number with unitary modulus we would obtain a different Jones vector representing the same ellipse (ie polarization). Jones vectors can be also evaluated using clock-wise and counter-clock-wise as the orthogonal fields.

Jones vectors are usually normalized in order to easily determine the polarization.

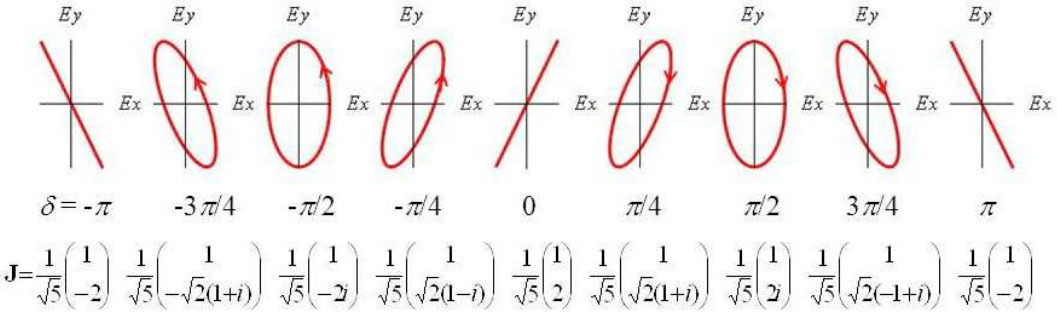

Figure 4.2: examples of normalized Jones vectors and their polarization ellipse.

4.2 Stokes vector

Stokes vector is a 4 components vector how's components are referred to as stokes parameters. The notation has been invented in order to easily describe the state of polarization of light even if it's not completely polarized. The Stokes vector is defined as[25]:

$$\bar{S} = \begin{pmatrix} S_0 \\ S_1 \\ S_2 \\ S_3 \end{pmatrix} = \begin{pmatrix} I \\ Q \\ U \\ V \end{pmatrix} = \begin{pmatrix} I \\ Ip\cos 2\psi \cos 2\chi \\ Ip\sin 2\psi \cos 2\chi \\ Ip\cos 2\chi \end{pmatrix}$$

Where I is the light intensity; p is the degree of polarization defined as the percentage of light that is polarized. The parameters ψ and χ are the same defined in the polarization ellipse.

it's common to refer as stokes vector the normalized 3 component version used for the Poincarè sphere.

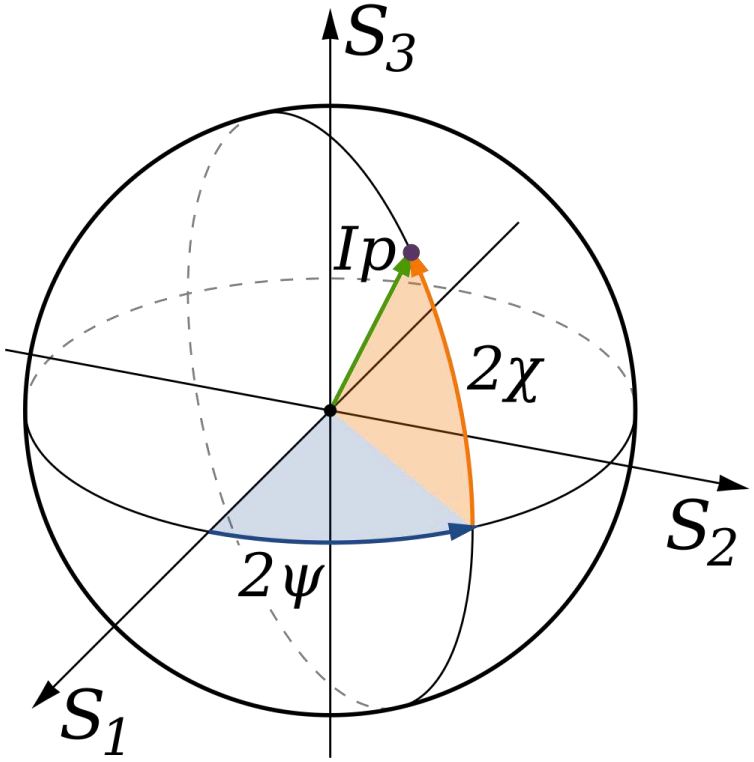

Figure 4.3: representation of the Poincarè sphere[27].

On the Poincarè sphere we map the normalized version of the Stokes vectors[27]:

$$\bar{S'} = \begin{pmatrix} S'_1 \\ S'_2 \\ S'_3 \end{pmatrix} = \begin{pmatrix} p\cos 2\psi \cos 2\chi \\ p\sin 2\psi \cos 2\chi \\ p\cos 2\chi \end{pmatrix}$$

The main advantage of this graphical representation is that similar polarization are represented close together. This allow to define some “special regions”:

- **North hemisphere**: right handed polarizations.
- **South Hemisphere**: left handed polarizations.
- **Equator**: linear polarizations.
- **Poles**: circular polarization.

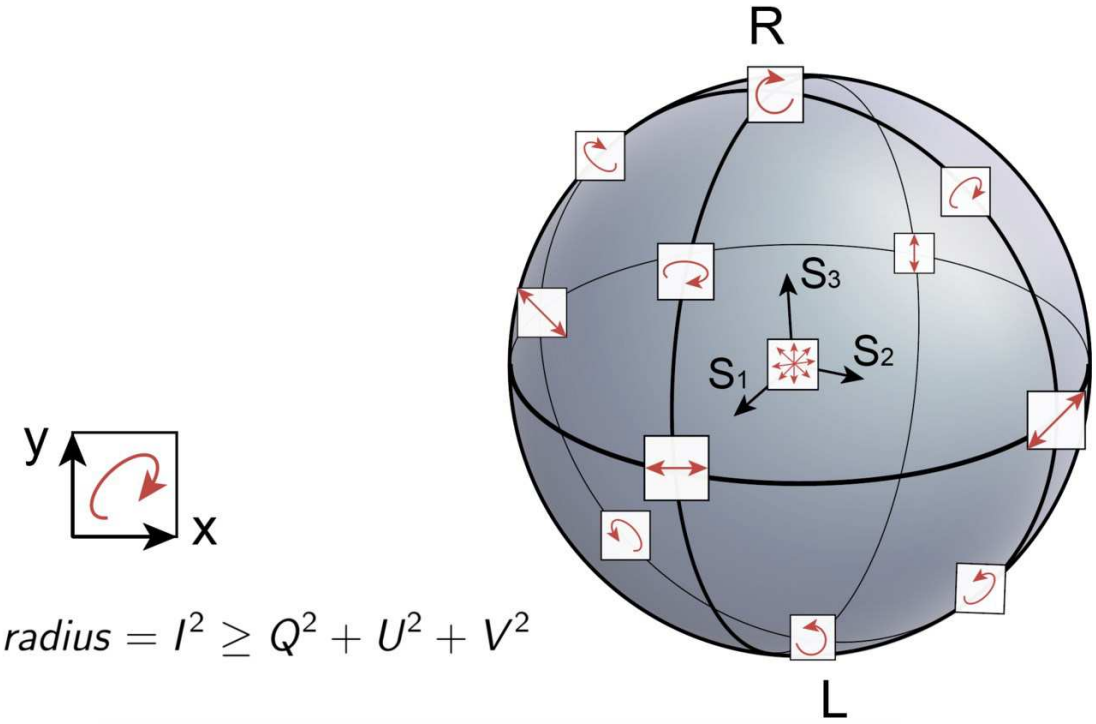

Figure 4.4: representation of the Poincarè sphere reagions[27].

It’s possible to evaluate the Stokes vector starting from the orthogonal components used for the Jones vector. Using the formula[25]:

$$S_0 = I = \left|E_{//}\right|^2 + |E_\perp|^2$$

$$S_1 = Ip\cos 2\psi \cos 2\chi = \left|E_{//}\right|^2 - |E_\perp|^2$$

$$S_2 = Ip\sin 2\psi \cos 2\chi = 2E_{//}E_\perp \cos(\vartheta_\perp - \vartheta_{//})$$

$$S_3 = Ip\cos 2\chi = 2E_{//}E_\perp \sin(\vartheta_\perp - \vartheta_{//})$$

From these formulas we understand that in order to evaluate light polarization we are required to measure the orthogonal components.

4.3 Birefringent materials and stokes vector

Birefringent materials are a class of substances which presents an optical axes. Light that passes through the material should be decomposed into $E_{//}$ orientated along the optical axes and $E_{\perp}$ with polarization perpendicular to the substance axes.
The birefringent presents different refraction indexes based on the polarization of light.
Due to this peculiarity the $E_{//}$ component will have propagation constant $k_{//} = \frac{2\pi n_{//}}{\lambda}$, while $E_{\perp} = \frac{2\pi n_{\perp}}{\lambda}$.
This velocity difference introduces a phase difference in the two components changing the polarization of the light[27].
Recalling the Jones vector form explained in section 4.1.2 the light emerging from a birefringent material is described as:

$$\bar{e'} = \begin{pmatrix} E'_{//} \\ E'_{\perp} \end{pmatrix} = \begin{pmatrix} a_{//} e^{i(\delta+\vartheta_{//})} \\ a_{\perp} e^{i\vartheta_{\perp}} \end{pmatrix}$$

Where δ is the phase delay introduced by the velocity difference between the components. This phase difference will alternate the Stokes parameter. In particular the new S'_2 and S'_3 are:

$$S'_2 = Ip \sin 2\psi' \cos 2\chi' = 2E_{//}E_{\perp} \cos(\vartheta_{\perp} - (\delta + \vartheta_{//}))$$
$$S'_3 = Ip \cos 2\chi' = 2E_{//}E_{\perp} \sin(\vartheta_{\perp} - (\delta + \vartheta_{//}))$$

Solving the two formulas as a system we can find the new elliptical angles for the emerging light: χ' and ψ'. We can finely conclude that the delay introduced between the components corresponds to a manipulation of the light's polarization state.

The manipulation to the polarization state introduced by birefringent are of two types[27]:

- **Diattenuation**: arises from the different absorption coefficients that the material has for the $E_{//}$ and $E_{\perp}$ components. The emerging light doesn't have the same component ratio than when entering.
- **Birefringence**: is the phenomena discuss earlier of different velocities introducing changes in the elliptical angles.

Both phenomena are generally happening at the same time; but it's common that one of the two is extremely dominant.

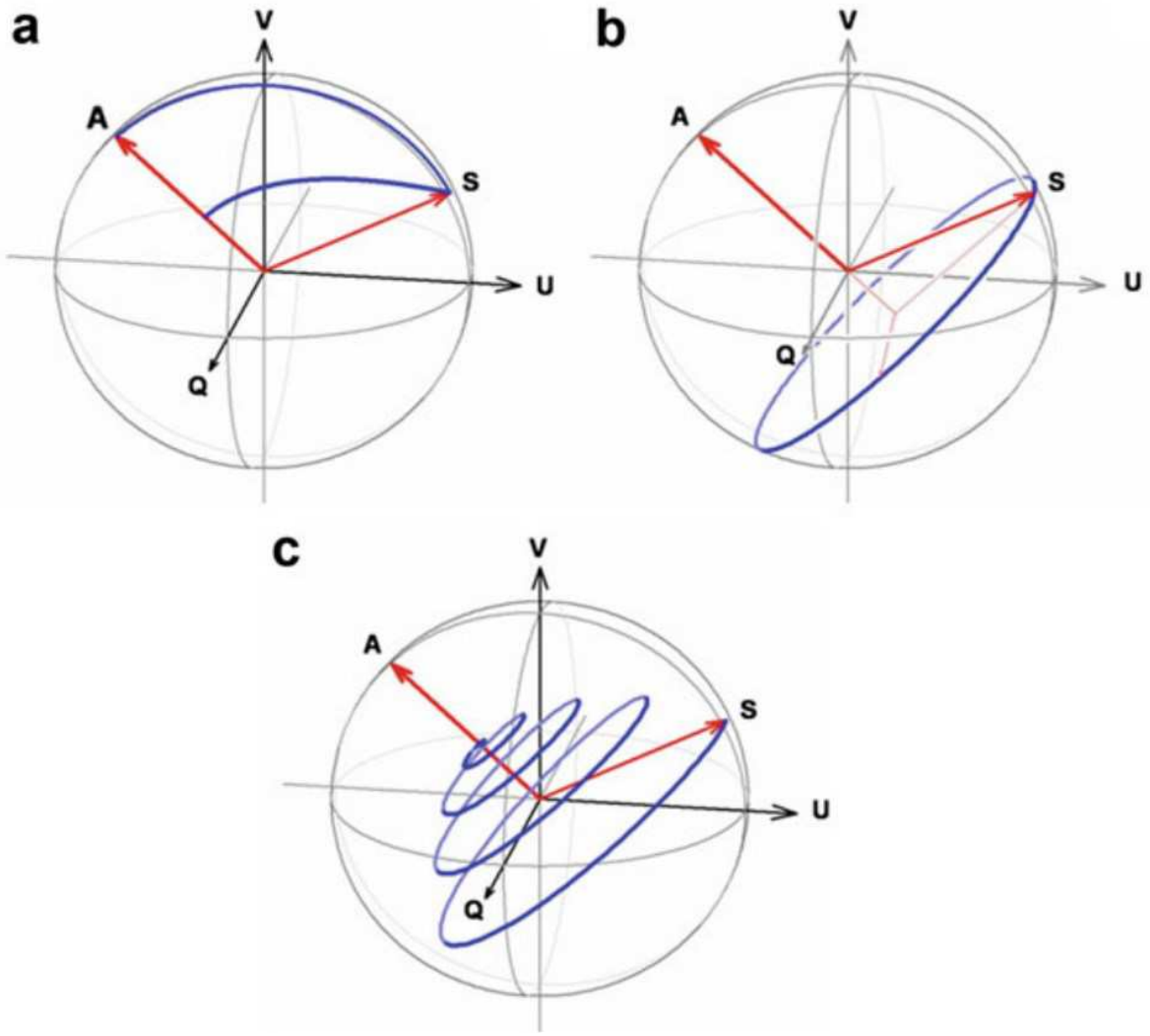

Figure 4.5: A)depiction of the diattenuation phenomena on the Poincarrè sphere. B) representation on the sphere of birefringence phenomena. C) how the polarization evolves when both diattenuations and birefringence take place.

Birefringence and diattenuation arises when the material has an organized molecular pattern that is maintained for large regions of it's volume. This leads to a different interaction rate between the electric field and the molecules depending on the orientation of the light; generating the different refractive indexes for the components.

Typical birefringent are. crystals, and amorph materials that have been strained by mechanical forces.

4.4 Set up changes for polarization sensing

Our system at the moment sends all the interfering light to the photodiode associated to channel A. We have to modify the optical circuit by removing the BPD in figure 3.14 in order to have the two interreferences copies free. In figure 4.4 it's shown the new section of the circuit that has to replace the BPD.

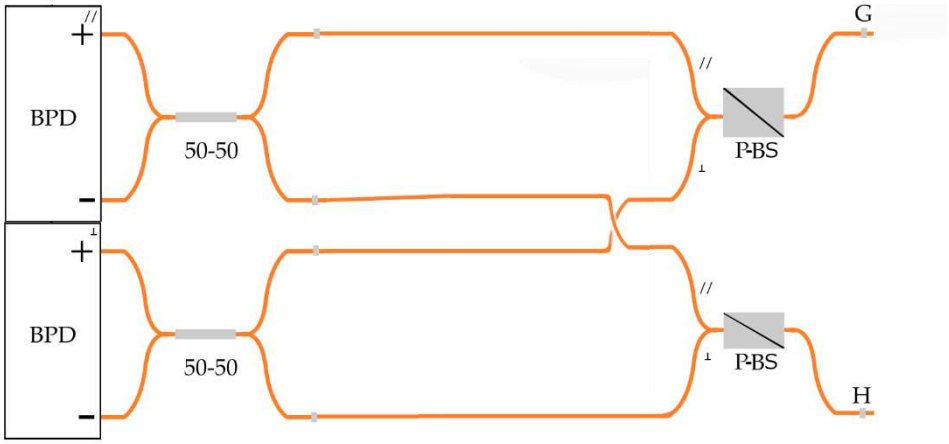

Figure 4.6: the two interferences now are sent to two polarization splitters (P-BS). The component with the same bases that are the output of the PS are then mixed with the use of 50/50 BSs before being fed to two BPD.

The interferences are now spitted into their bases. The signals with the same Base are then fed to the BPDs. Now the $E_{//}$ component of the interference is registered on channel A while the $E_{\perp}$ component to B. the new configuration can register the components separately allowing us to evaluate the Stokes parameter.

Below a scheme of the final set up.

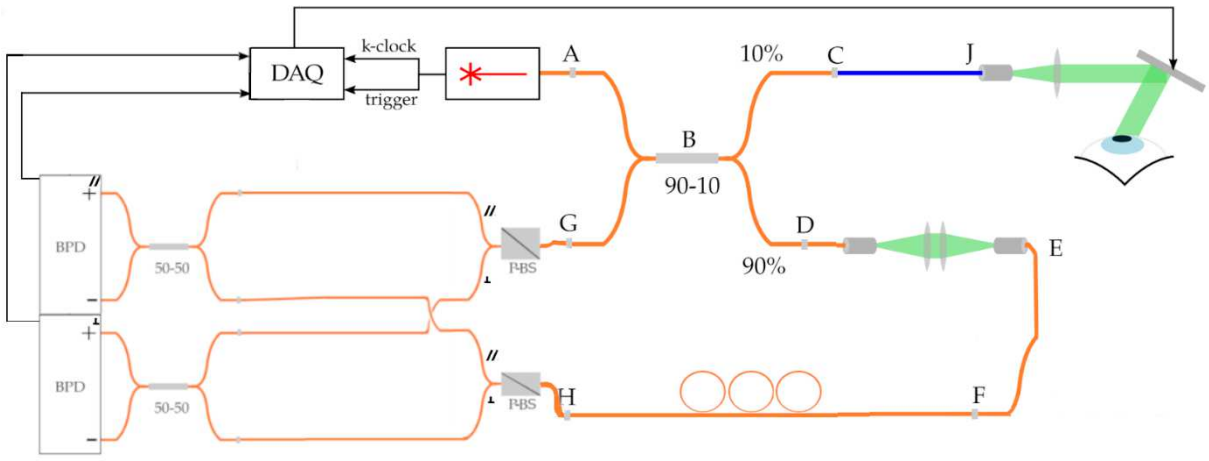

Figure 4.7: The final set up for the realization of our PSS-OCT

4.5 Optical Path differences between channels

On the datasheet provided by Thorlabs the two PS and BS inserted should have the same lengths. When we tried to run the methods for the generation of the classical "OCT" images on the two channel separately, we have noticed that the mirror surfaces do not appear at the same distances. There are tiny path differences between the channels that are causing miss-alignments. In order to correctly evaluate the Stokes parameter it's essential that the two channels are align.

To fix this problem we had to add a new method. This new method receives two numbers (o_A, o_B) from boxes that have been added in the interface. These numbers are used to evaluate the offset required to align the channels.

$$offset_A = o_A \cdot \delta\lambda$$
$$offset_B = o_B \cdot \delta\lambda$$

Where $\delta\lambda = \frac{1}{\delta k}$ with δk is the wavenumber change in between two consecutive samples. δk is calculated by the program when we configure the sampling rate of the DAQ. $offset_A$ indicate how much the channel A has to be shifted to the left; $offset_B$ indicates how much the channel B has to be shifted to the right.

In order to apply the shift we used the modulation property of the Fourier transform:

$$F\left(x(t)e^{-it\,offset}\right) = X(f + offset)$$

In our case we have a discrete signal $x(n\delta k)$ which is the A-scan. The formula becomes:

$$F\left(x(n\delta k)e^{-i\,n\delta k\,offset}\right) = X(n\delta\lambda + offset)$$

Where n is the sample index within the A-scan and $offset = offset_A$ for channel A while it's $offset = -offset_B$ for channel B.

The introduction of these shifts will cause the loss of the samples at the edges of the channels. When we will evaluate the Stokes parameters we will not be able to correctly evaluate them at the right and left edges of the image due to the shifts.

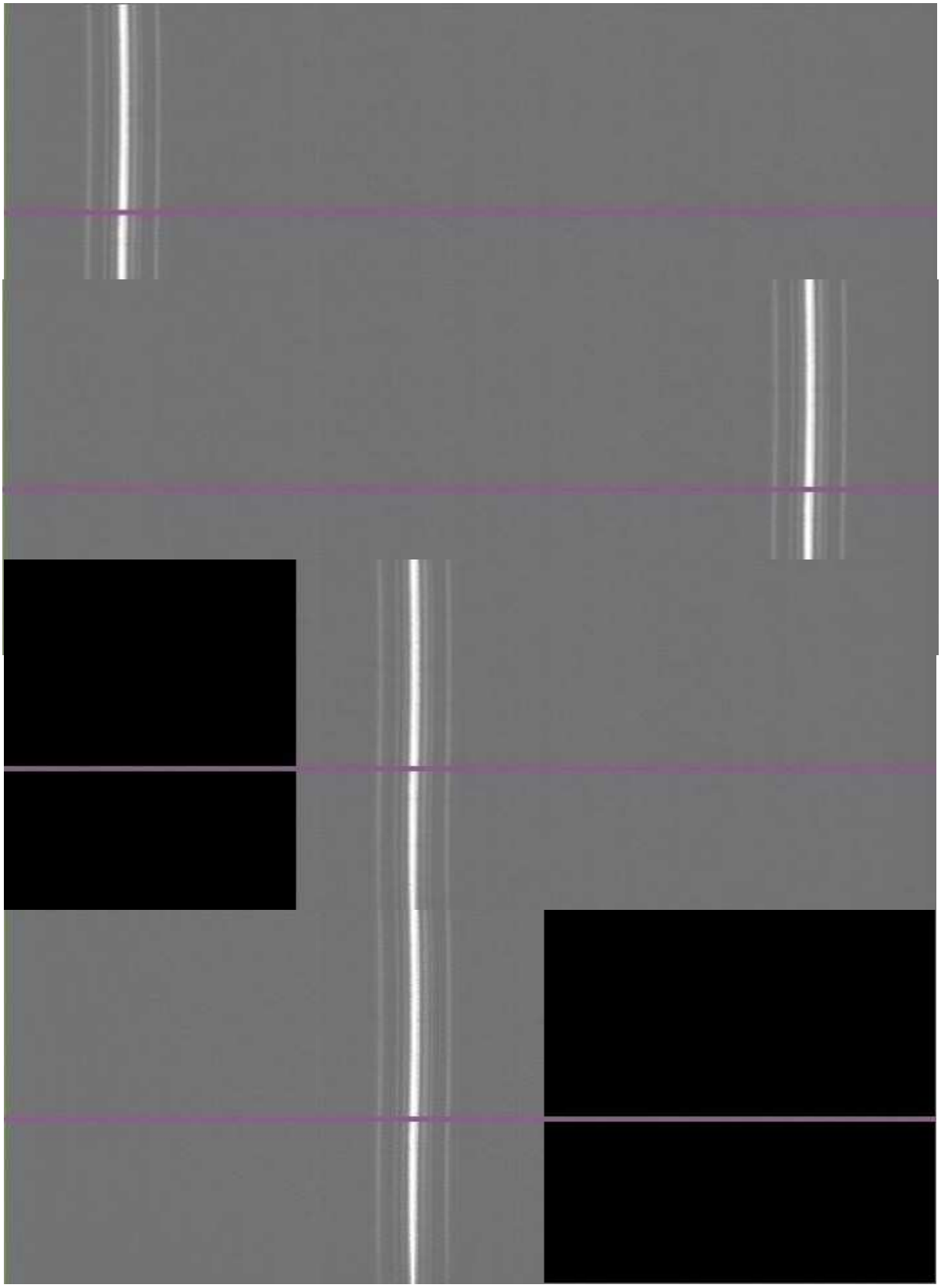

Figure 4.8: the two channel before the shift take place. on the top. Below the channels after the shift. The dark areas at the sides of the channel are due to the shifts that introduce 0-samples at the opposite edges of the movement.

4.6 Stokes Parameter evaluation

Now to evaluate the stokes parameter we configure four new buffers with the dimensions of a B-scan. These buffers will save the Stokes parameters. After the configuration we load the B-scans of cannels A and B which contain the values of $E_{//}$ and $E_{\perp}$ respectively. Using the formulas in section 4.2 we can easily evaluate all the parameters S_i with $1 = 0,1,2,3$. The parameters evaluated by applying the 4.2 formulas cell by cell .The results are used to fill the corresponding buffer for the parameter.

4.7 Single Stokes Parameter images

Once we evaluated the Stokes parameters for each cell we have to translate them into images.

First image aims to represent the $S_0 = I$. This parameter tells us the overall light intensity arriving from the region mapped without considering the polarization. For this reason we can simply use the greyscale method described in Chapter 3. It could be interesting to visualise only the light with a particular polarization. To do so we use once again the greyscale method using at as inputs the buffers containing the B-scans from channels A and B.

It's now possible to choose if we want to see the overall intensity or the intensity coming from a specific channel. To select which image we are interested into we have introduced a dropdown menu on the left column of the UI.

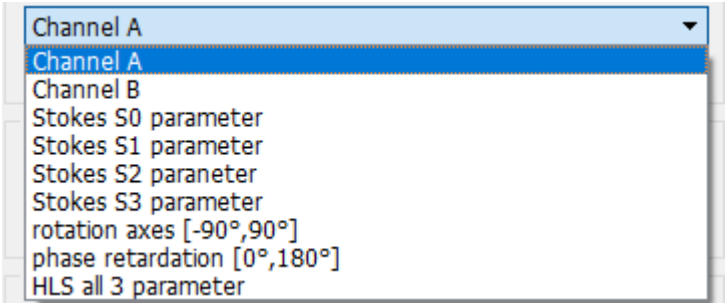

Figure 4.9: dropdown menu to select the which image to visualise.

Second parameter image is to display $S_1 = \left|E_{//}\right|^2 - |E_{\perp}|^2$. This parameter can't use the greyscale as the previous cases. S_1 can be negative so we have to use multiple colours.

For the realization of this new type of texture (image) we decided to use the following convention:

- **Red:** for positive values
- **Green:** for negative values
- **White:** for zero.

The method is similar to the greyscale described in Chapter 3.

To generate the image we first take the following steps:

- Three matrixes for the RGB colour are generated (all cells are NULL).
- Take in input the lower and upper thresholds from the sliders (same slider of grey scale)
- Consider now the buffer containing all the S_i parameters ($i = 1$ in this case). To each cell (identified by the indexes m, n) we will make the following calculations:
    1. If positive we mark a Boolean flag as true.
    2. We overwrite the cell with the modulus of the value contained in it.
    3. We subtract to the cell the lower threshold. If the result is negative we set the value to 0.
    4. We divide the result by the difference between upper and lower thresholds. If the result is above 1 we set it to 1.
    5. We will call the content of the cell at this point as c.
    6. If the flag is true we give the value 255 at the cell in position m, n in the red matrix; otherwise we set to 255 the corresponding cell in the green matrix.
    7. The non-initialized cell in position m, n of the RGB matrixes are now initialized to contain $255 \cdot (1 - c)$.

Now we have generated the RGB matrixes required for the generation of a RGB texture. We use the matrixes as inputs for the C++ libraries and we obtain the image (1250x752 px). We will call this method *singleParameterRGB*. The texture generated will display pure red pixels if the value of c in position m, n is equal to one and the cell originally contained a positive value for S_i; as c decreases the saturation of green and blue will grow leading to a whiter colour. If the original value of S_i was negative the procedure is the same but the roles of the green and red are reversed.

This method is used also for the creation of the images from Stokes parameters S_2 and S_3.

Examples of images generated with these method are below.

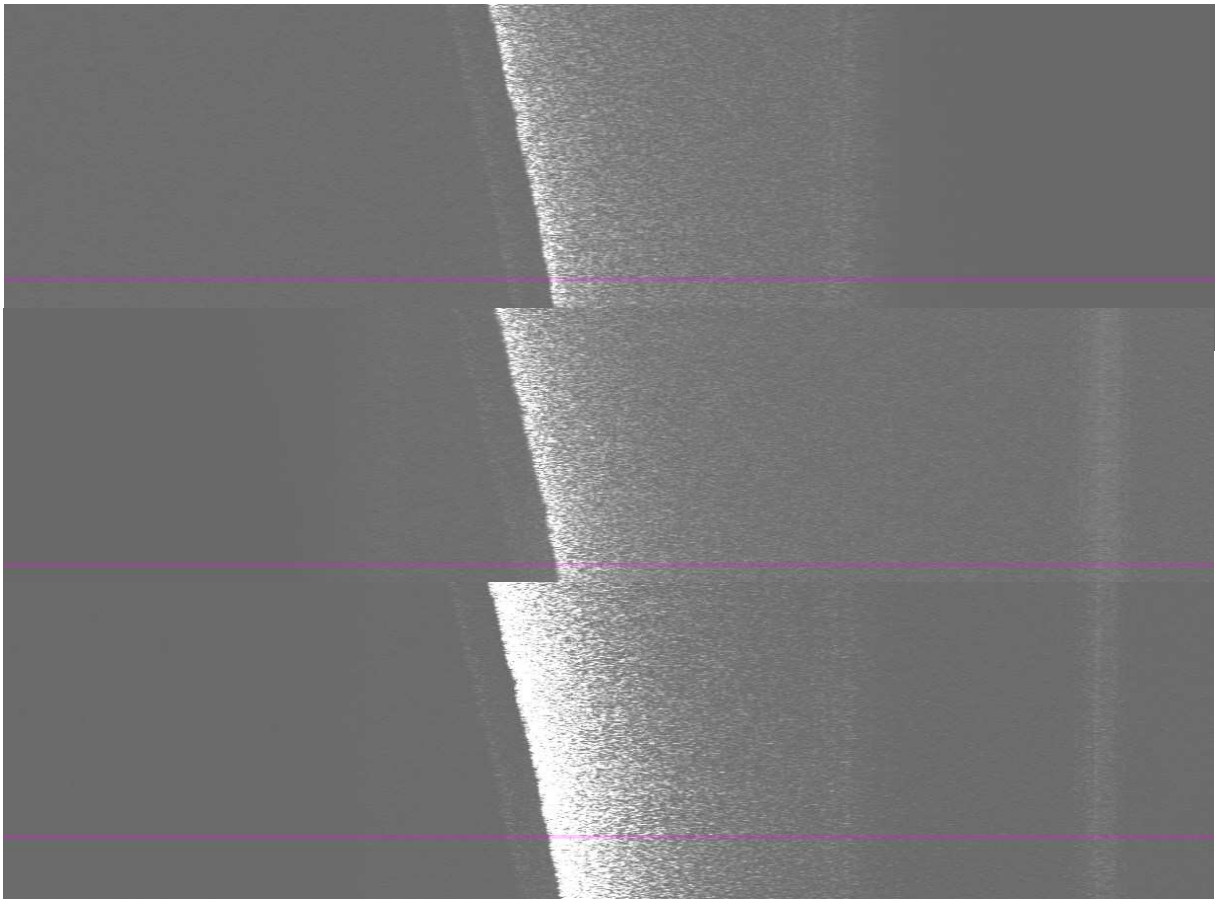

Figure 4.10: greyscale images of the channels and S_0. The sample is a curved cardboard

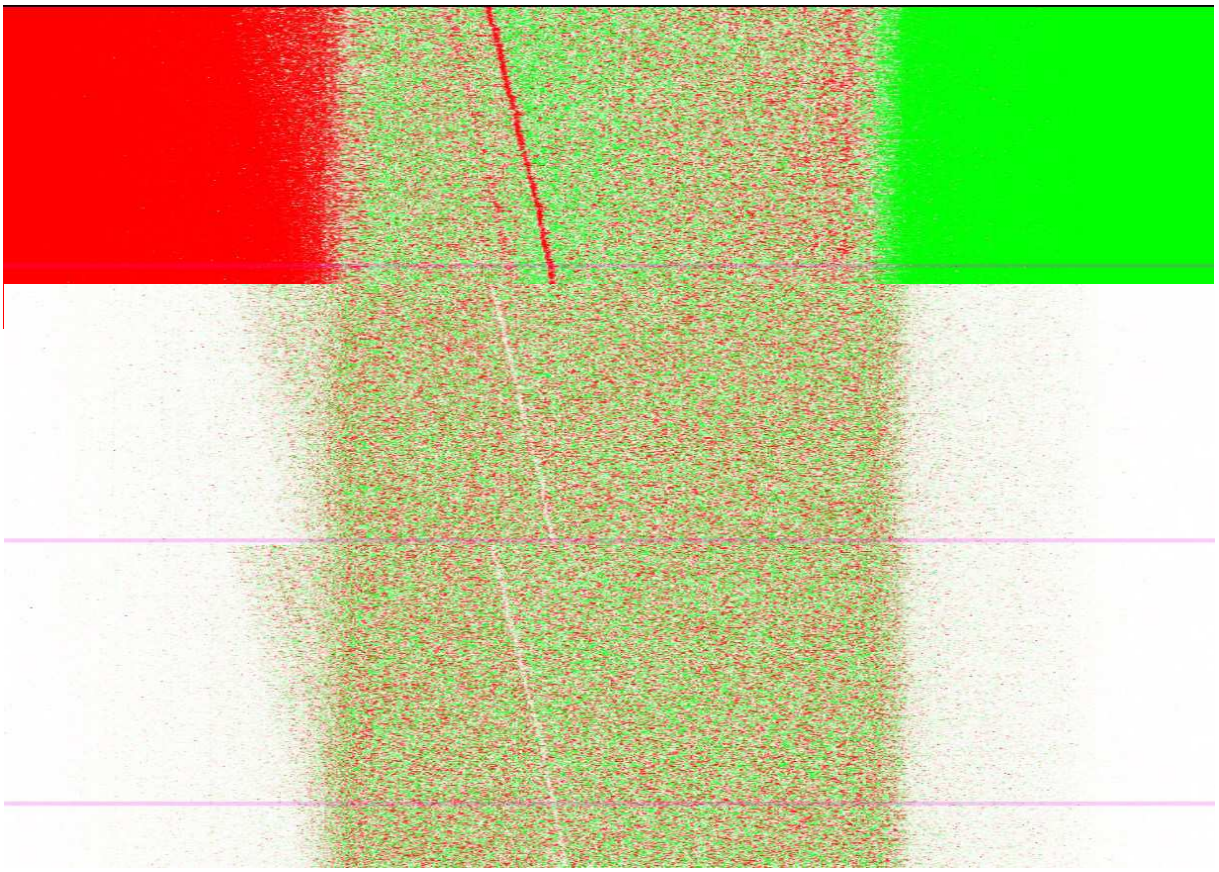

Figure 4.11: Single Stokes parameters images for S_1, S_2, S_3. Sample is the same cardboard of figure 4.10

As we can see the images associated to S_1, S_2, S_3 are not really readable. We need to take into consideration more than one parameter in order to have meaningful images.

For the green and red band on S_1 is due to the channel shift we used to overlap the channels. On the right only the samples of channel B are different from 0 resulting in all the pixel in that region to be associated with green since the second channel is that with higher intensity. On the left the red band is due for the same reasons, but this time is channel A to have valorised samples.

In images S_2, S_3 the areas in which we lack the samples coming from one of the channels will be marked as withe. The with is associated to a 0 value in these parameters; the lack of information from a channel in a region leads to$2\psi\ or 2\chi$ being 0 in that area.

4.8 Two parameter images

The main problem with the images produced by *singleParameterRGB* is that all the pixels have the same saturations, making impossible to clearly distinguish the in air regions and the regions inside the sample.

In order to improve the readability we will also add information from S_0 as weights for the matrixes produced by *singleParameterRGB*. After obtaining the RGB matrixes we will call a new method that will take the following steps:

- Consider S_0. buffer.
- Acquire the maximum value of the buffer.
- Normalize the matrix by dividing every element by the maximum identified.
- The resulting matrix has all values between 0 and 1. This matrix will be our weight matrix.
- Multiply cell by cell the RGB matrixes by the weight matrix.

The weighted RGB matrix will be then sent to create the texture.

The images produced in this case are as follow.

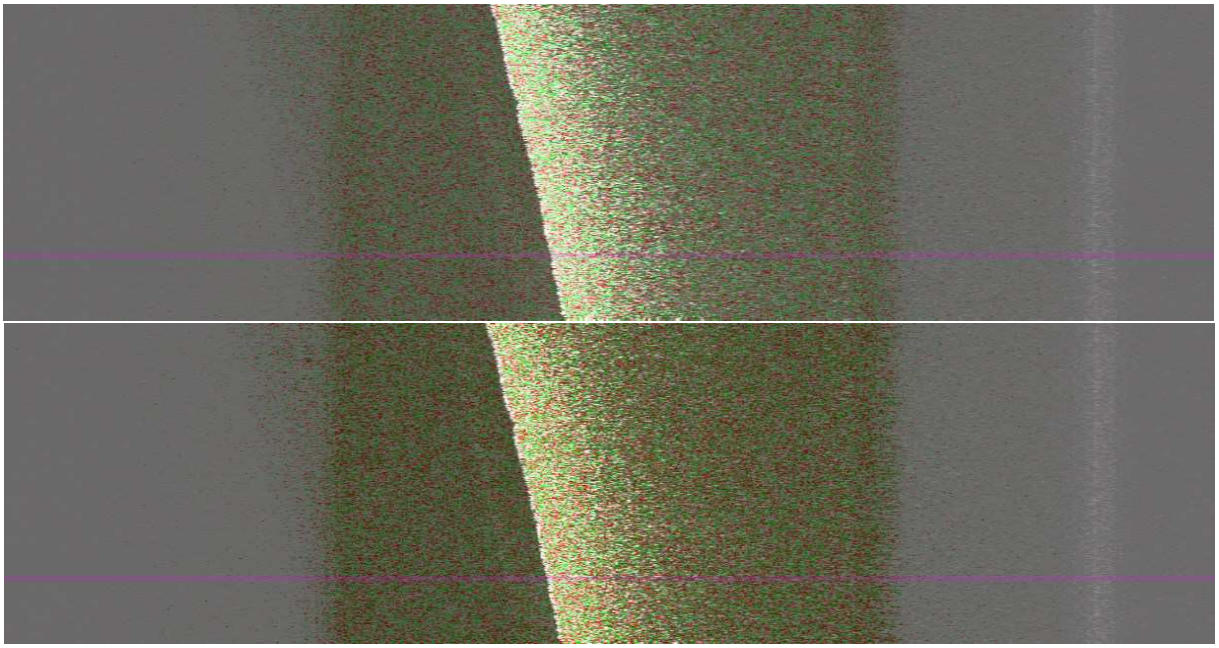

Figure 4.12: double Stokes parameters images for S_2, S_3 using S_0 as weight.

4.9 Intensity and elliptical parameter images

The images produced with the stokes vector have some utility:

- S_0 images are equivalent to a normal OCT image since they only map intensity.
- S_1 images allow to discover whether in a region there is a preference for some polarization.
- $S_2 = Ip \sin 2\psi \cos 2\chi$ images can't be easily used to derive any property directly.
- $S_3 = Ip \sin 2\chi$ images will map the angle 2χ but not in a linear scale.

To improve the readability we intend to recover the elliptical parameter from the Stokes vectors for each pixel. The formulas are:

$$2\chi = \tan^{-1}\frac{S_2}{S_1}$$

$$2\psi = \sin^{-1}\frac{S_3}{S_0}$$

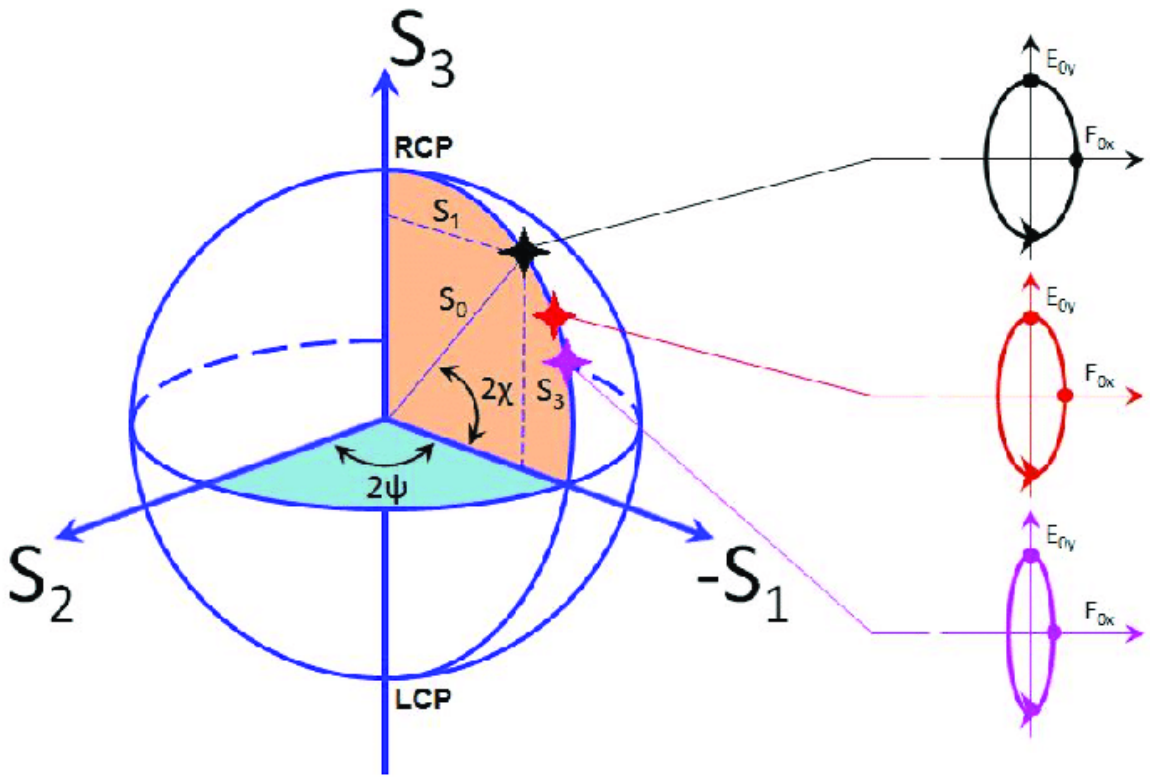

Figure 4.13: Poincarrè sphere whit the elliptical angle highlighted.

Due to the ambiguity of the functions $\tan^{-1}$ and $\sin^{-1}$ the angle that we will estimate with C++ will be on the following intervals:

$$2\chi \in \left[-\frac{\pi}{2}, \frac{\pi}{2}\right]$$

$$2\psi \in \left[-\frac{\pi}{2}, \frac{\pi}{2}\right]$$

To generate the new images using the elliptical parameter we will recycle the method used for the images using two Stokes parameters. S_0 will once again be used to produce the weight matrix wile the second parameter will be eighter 2χ or 2ψ. Since the colour are decided using the normalized Stokes parameter for commodity we are required to change the interval on which the angles are defined to be: $[-1,1]$. We change the domain by dividing the elliptical parameters by $\frac{\pi}{2}$. We can now repeat the same steps used in the previous paragraph.

The colour coding is as follow:

- Black: for no intensity.
- Red: positive angles.
- Green: negative angles.
- White: angle equal to 0.

The closer to $\frac{\pi}{2}$ the angle the more red is present. If the angle reduces the colour will become wither until becoming pure withe when reaching the 0. If the angle continues to decrease it will turn progressively greener until reaching a pure green for $-\frac{\pi}{2}$.

The intensity of light will define the saturation of the pixels. We have full saturation for :

$$S_0 \geq th_{upper}$$

Where th stands for threshold. Zero saturation , hence black, for :

$$th_{upper} \geq S_0$$

Since the colour will turn darker whenever the intensity is lower we didn't choose blue for negative angles since it could be confusing.

Using these images we are now capable to see if regions of the sample presents birefringent properties. Birefringence manifest in an evolution of the elliptical Angeles in the material. In birefringent materials the components $E_{\perp}$ and $E_{//}$ will see different refractive indexes; introducing an alteration in the polarization state evolution in space causing the angles 2χ and 2ψ to evolve generally at different speeds.

To identify the birefringent regions we are looking for areas in the 2χ images in which the colours change at a different frequency compared to the same region in the 2ψ image.

Although looking for the spatial evolution of 2χ and 2ψ is sufficient to detect birefringence it's not a convenient method. Looking through the literature on PS-OCT we have found that elliptical angle imaging generally make use of pointers that select the surface of the sample. Once the surface has been identify the angles 2χ or 2ψ are evaluated. The angles that will be used for the imaging of the pixel in position (n, m) will no longer be the 2χ or 2ψ of the pixel, but the difference between the elliptical angle at the surface and the corresponding elliptical angle in position (n, m).
Below an image obtained by measuring the difference between surface angle 2χ and 2χ at the other depth.

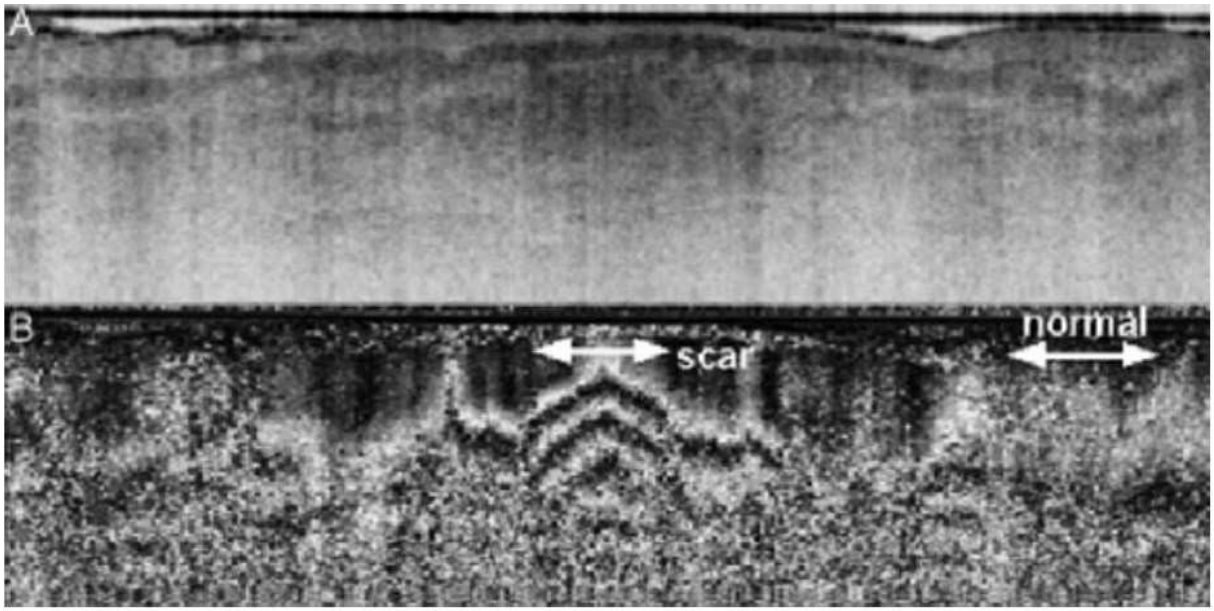

Figure 4.14: A) traditional intensity image of skin. B) a PS-OCT image of the same skin mapping the difference between the angle 2χ at the surface - 2χ at the other depth. From image B we are capable to detect a scar due to the different evolution of the elliptical angle in space[1].

We implemented our version of this method by using a vertical cursor that we can move by using a slider. The column selected will be highlighted in yellow. If we check the checkbox in figure 4.15 while the channel drop menu has either: rotation axes or phase retardation. We will use the method for the elliptical parameter texture, while using as inputs the phase difference between the angles in the corresponding pixel and the elliptical parameter in the selected position within the Ascan.

The results of this method are displayed in chapter 5 were we will comment some images taken.

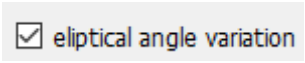

Figure 4.14: eliptical angle difference checkbox

4.10 Experimental three parameter images

This is the final type of imaging that we will try to implement. It's completely experimental since I didn't found anywhere attempts to show simultaneously all three parameters in the same picture.

We attempted to display the two elliptical angles and the intensity all in the same picture using HSL colours.

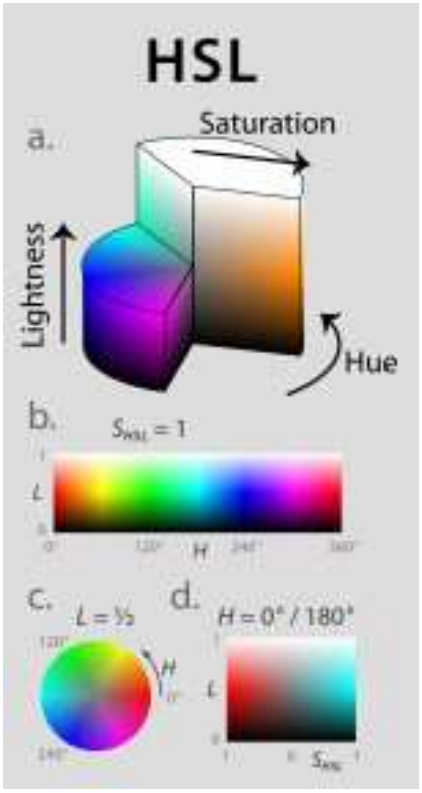

Figure 4.16: HSL colour diagram indicated by a). b) display all the colour possible by fixing the S to 100. C) is the colour wheel obtained with a horizontal section of the HSL cylinder. D) is a section of the HSL cylinder taken with a vertical plane passing through the center.

HSL is an alternative to RGB in order to code colours. In RGB each pixel is defined by three integers between 0 to 255; each of these integers defines the saturation of one of the colours: red, green and blue. In this scheme black is defined by the minimum saturation for all colours while white by maximum saturations for all. Grey scale is obtained by using all three basic colours with the same saturation, but with values between the black and white.

In HSL colours are still defined by three values, but each have completely different meanings:

- **Lightness (L):** is a number between 0 and 100 which define ow close to the white (L=100) or the black (L=0) the shade of the selected colour will be.

- **Saturation (S):** once again a value between 0 and 100. This time this indicates the amount of the selected colour that will be displayed. S=0 will lead the colour to be completely defined by the Lightness parameter.
- **Hue (H):** also known as colour coordinate; it define the selected colour. It's a number in degree so it' value ranges between 0° and 360°. The colour red correspond to 0° and 360° green to 120° and blue to 240°. Angles in between the basic colour are obtained by mixing the two primary colour in proportion to the distances between them.

Since our C++ methods use RGB we are required to translate the HSL colour coordinates into RGB. This process can be done using the following formulas:

$$C = (1 - |2L - 1|) \times S$$

$$X = (1 - \left|\frac{H}{60°}\ mod\ 2 - 1\right|) \times C$$

$$m = L - \frac{C}{2}$$

$$(R', G', B') = \begin{cases} (C, X, 0) & 0° \leq H \leq 60° \\ (X, C, 0) & 60° \leq H \leq 120° \\ (0, C, X) & 120° \leq H \leq 180° \\ (0, X, C) & 180° \leq H \leq 240° \\ (X, 0, C) & 240° \leq H \leq 300° \\ (C, 0, X) & 300° \leq H \leq 360° \end{cases}$$

$$(R, G, B) = \big((R' + m) \times 255, (G' + m) \times 255, (B' + m) \times 255\big)$$

Now that we have the algorithm to convert HSL coordinate to a format compatible with our texture generator we only have to define how to assign the parameters.

Lightness is assign to the light intensity since it's logically more fitting. We use the upper and lower thresholds sliders in order to define the ranges:

- If $S_0 < th_{lower}$ we set $H = 0$
- If $S_0 > th_{upper}$ we set $H = 100$
- If $th_{lower} < S_0 < th_{upper}$ we set $H = \frac{S_0 - th_{lower}}{th_{upper}} \times 100$

For the saturation we chose the angle 2χ or 2ψ; the step taken to fit the desired range are:

- $2\chi' = 2\chi + \frac{\pi}{2}$
- $S = \frac{2\chi'}{\frac{\pi}{2}} \times 100$

Finally 2ψ is assign to HUE. Step taken to fit the desired range are:

- $2\psi' = \left(2\psi + \frac{\pi}{2}\right) \times 2$
- $S = \frac{2\psi'}{\pi} \times 180°$

An example of how these images looks is below.

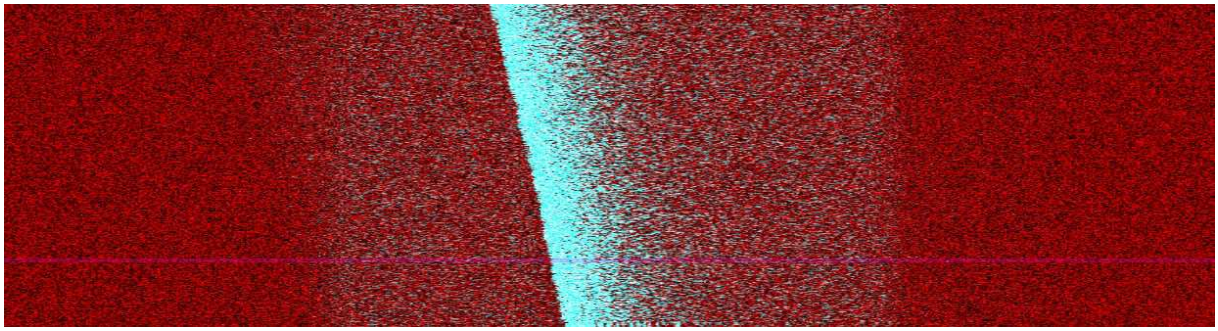

Figure 4.17: HSL texture of the cardboard we used so far.

This image is quite unreadable. Trying to display all three parameter (intensity, 2ψ and 2χ) has been proven to be a failure.
In particular the intensity has to be used as Lightness since this will allow us to identify the regions with backscattering from those with none. The problem arises when we have high reflection. These area will be forced to become withe no matter the values of the other parameters. This results in L overwriting both S and H; we can partially solve this problem by adjusting the upper and lower threshold sliders in order to never reach $L > 0.8$. we avoided L saturation in figure 4.17, but the outcomes is that the noise cached in regions with no backscattering is now enough to be displayed lowering the image quality.
Finally also the Saturation parameter can overwrite the Hue. Low values of S will lead to black for 0 or various shades of grey that are not distinguishable between each other.

HSL images will not be discussed in chapter 5 since are not usable.

CHAPTER 5: Introduction to OCT

In this chapter we will analyse to the images we can generate with this set-up. From these images we can observe our OCT system performances and issues.

5.1 Power losses and long fibers

We took some images of semi-transparent material with low no internal reflection such as scotch and crystals. The results are as follow.

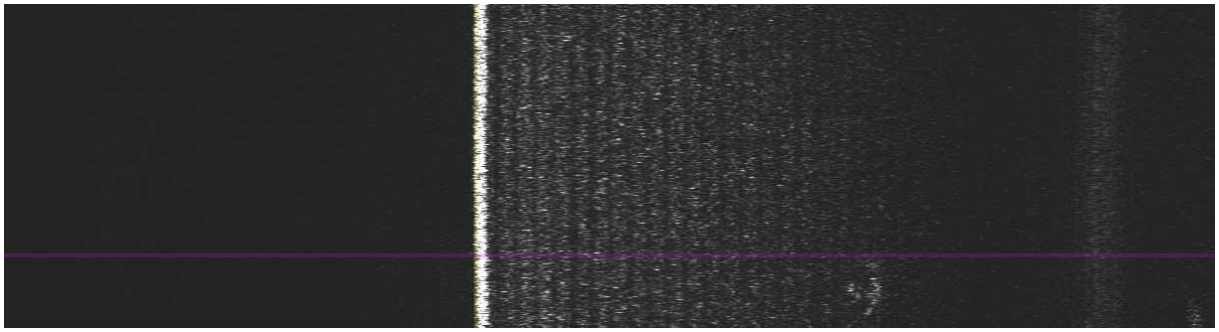

Figure 5.1: Scotch images of intensity from top to bottom we see: horizontally polarized light, vertically polarized light and overall intensity

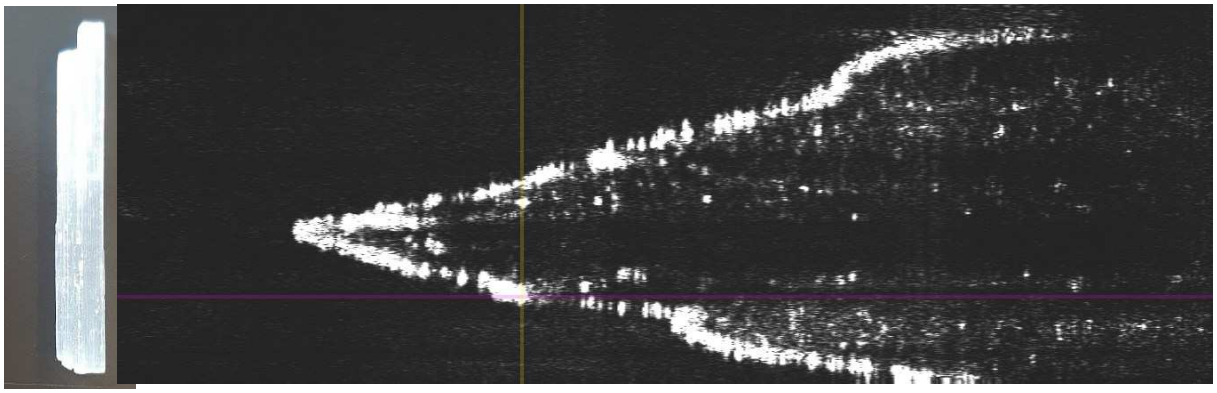

Figure 5.2: crystal images of intensity from top to bottom we see: horizontally polarized light, vertically polarized light and overall intensity. On the top right corner an image of the crystal bar.

In figures 5.1 we are observing the surface of a roll of scotch. We can clearly see the surface between air and the first layer of scotch; but inside the roll we have very little backscattering. In Figure 5.2 we are observing the crystal bar shown on the left. Here we have similar observations; the air-crystal interface is clearly defined; but the internal reflections are barely visible.

The inability to perceive internal reflection inside translucent material prevent us to evaluate the Stokes parameters inside the material. Without the possibility to evaluate the elliptical angles we are not capable to check for the birefringence. With these considerations we can

conclude that we will not be able to use Crystals to showcase birefringent materials; we will need to use opaque birefringent material such as: bones, cartilages and teeth.

Analysing the optical circuit we can deduce that the reason we are not capable to detect the internal reflections in semi-transparent material is due to the high amount of losses in our set-up. The necessity of balancing the arms of the device and not having fiber segments appositely cut to fit the system needs led to the use of multiple fiber brackets found around the lab in order to generate two equals paths.
This approach has led to optical path in the fiber of 11.5 m (considering section that have been traversed two times). The extremely long length of the arms has led to high chromatic dispersions and to an high number of fibber connectors. Fiber connectors usually introduce a 3 dB loss.
The number of connectors in the sample arm is 6 with the connectors in position J and C (in figure 5.3) being traversed 2 times; resulting in losses happening 8 times.
The number of connectors in the reference arm is instead is 10 with no connector being traversed multiple times. We can conclude that the system is losing most of the light the propagates within it.
The best solution to the problem would be cutting and splicing of fibers specifically for our circuit in order to minimise the amount of connectors and hence losses.

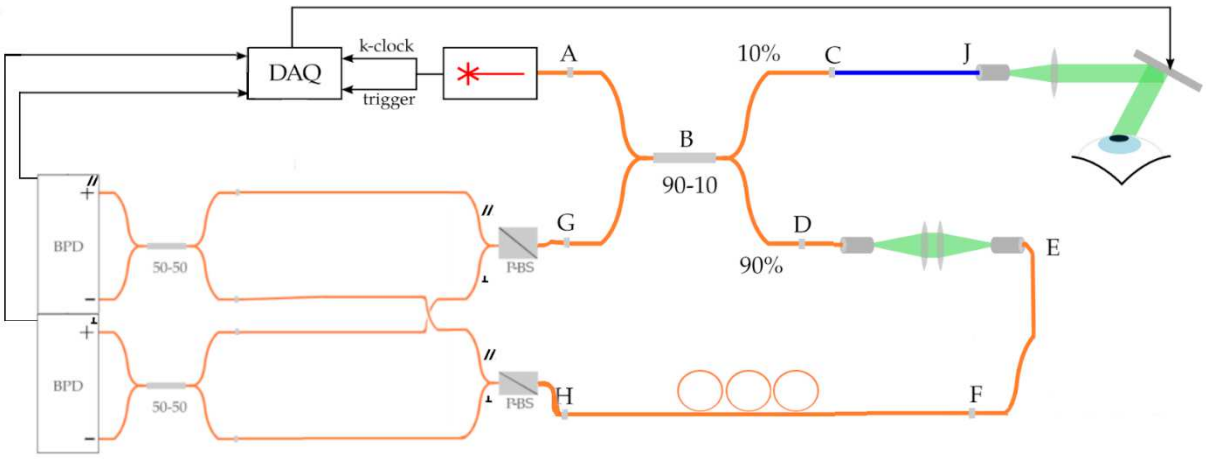

Figure 5.3: schematic of our OCT system previously shown as figure 4.16.

5.2 What can be learned by elliptical angles images.

We will recall here the image 4.14 reporting the angle 2χ and it's evolution in skin. The sample reports healthy skin and a section of a scar (both are birefringent materials). This image has been taken in order to highlight that scar tissue seams to have cell organized following a more compact pattern and a different structure. The difference in cell density and orientation in the scar manifest as a change in refractive index. In particular the increase in the cell density has led to an increase in refractive index and hence a quicker evolution of the parameter 2ϑ in the area occupied by scar tissue.

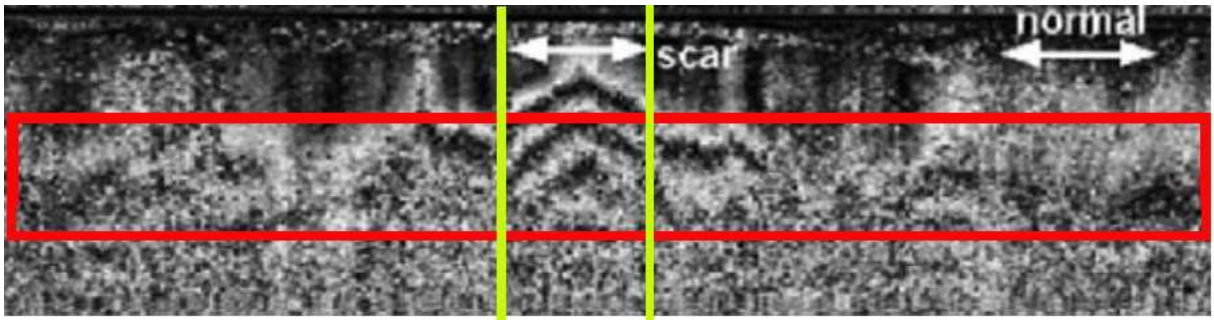

Figure 5.4: image of the skin whit highlighted the region we will use to make the comparison. The red area is the region with a similar level of noise compared to our PS-OCT. The area between the yellow line is the scar tissue with higher density causing the polarization evolution to be faster in te region.

As we saw in section 4.3 birefringent materials causes a change in polarization and hence a change of the parameter 2ϑ during the propagation. In section 4.3 we have seen that the birefringence manifest as a rotation of the polarization state on the Poincarrè sphere. This means that it's possible to find materials that will only manipulate one of the elliptical angles 2χ and 2ψ if the diattenuation is particularly weak. This means that we should look at both 2χ and 2ψ images in order to asses birefringence. If a material does not present variation in colour in images that colour code 2χ or 2ψ it means that the material doesn't introduce phase retardations between the components and hence it's not a birefringent.

As already said our set-up is extremely lossy so the noise of the of the BPD is enough to introduce very noticeable changes in the angle considered for single pixels if the noise contributions on channel A have opposed sign compare to channel B. we will then consider the dominant colour of an area to judge the value of the elliptical angle in the regions.

Our noisy images will be then be more comparable to the lower section of the figure 5.4 (region highlighted); in the lower regions there is less backscattered light hence the noise has heavier consequences in evaluating the selected elliptical parameter.

5.3 Opaque non-birefringent materials

Here will be shown some Bscans of opaque materials without birefringence properties.

5.3.1 Wood

Images taken of a piece of wood.

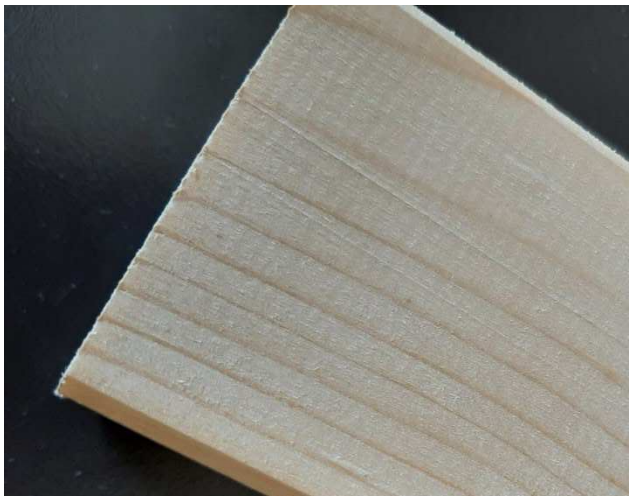

Figure 5.5: image of the wood sample.

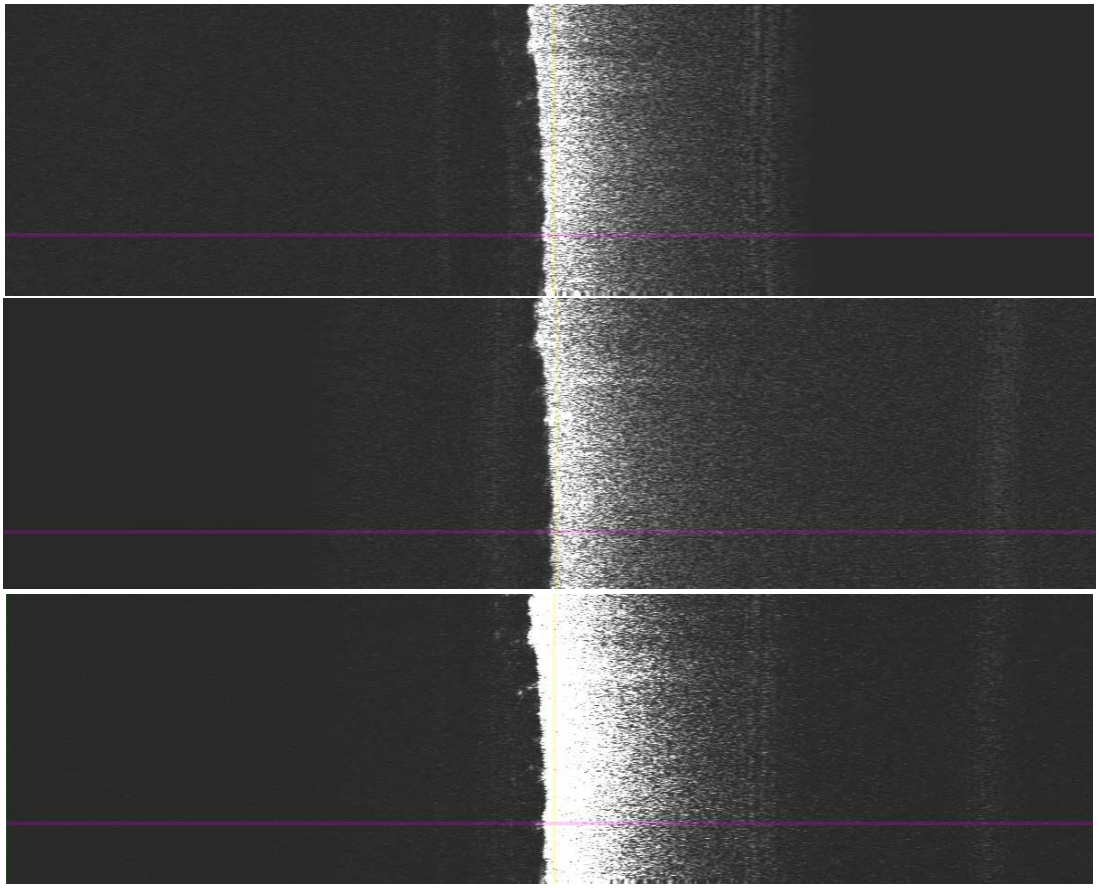

Figure 5.6: Wood images of intensity from top to bottom we see: horizontally polarized light, vertically polarized light and overall intensity (S_0).

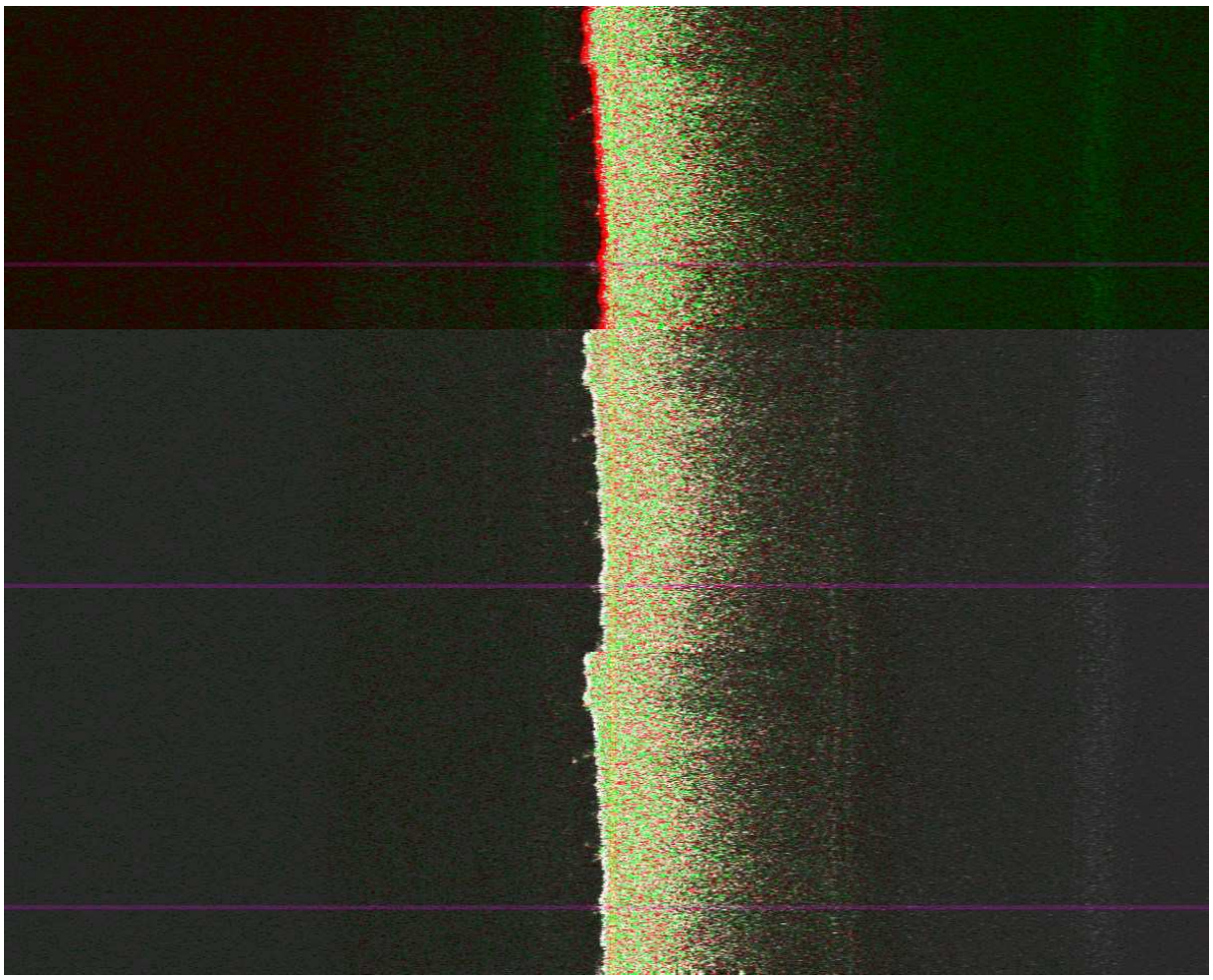

Figure 5.7: wood images of stokes parameters weighted by the light intensity from top to bottom we see: S_1, S_2 and S_3.

The Stokes images for S_2 and S_3 do not contain information of interest since they reports the same information of the images 2ψ and 2χ, but presented with a non-linear scale which makes colours change much quicker. As we made these observations we choose to not display S_2 and S_3 for other samples. S_1 images gives us information on which polarization of light is dominant in various area; this information isn't particularly useful hence it will not be reported for new samples.

The birefringence information are recovered by the images reporting elliptical angles.

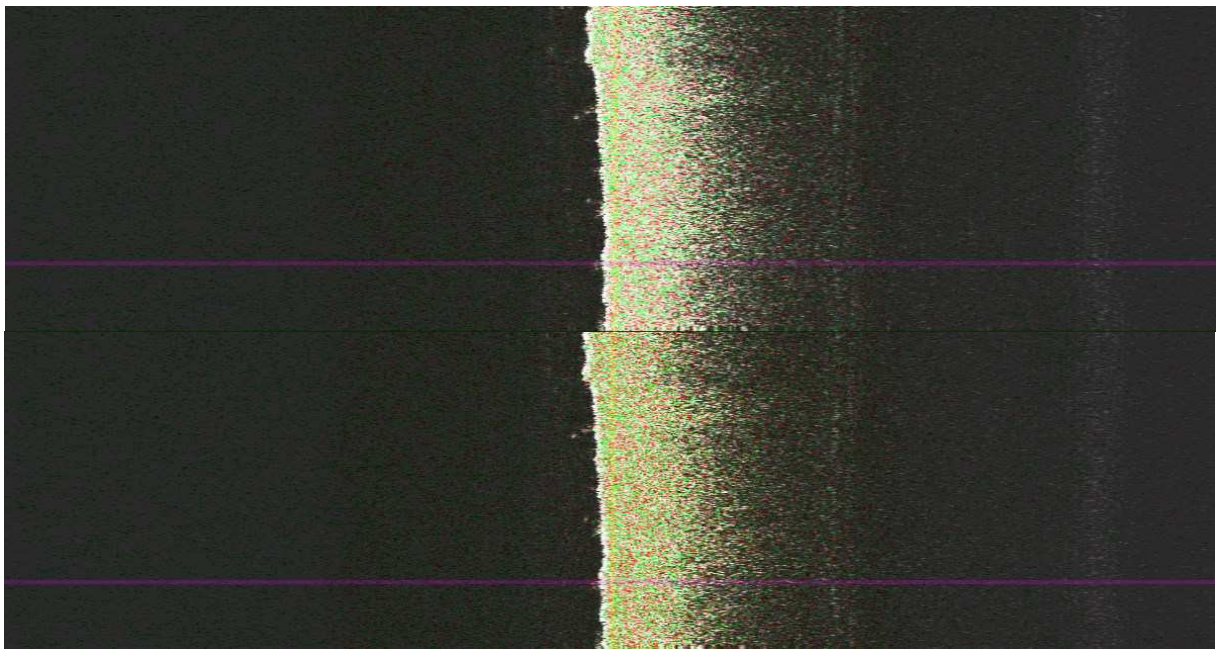

Figure 5.8: wood images of elliptical angles weighted by the light intensity from top to bottom we see: 2ψ and 2χ.

In figure 5.8 the 2ψ image has a whitish green colour and doesn't present regions with different colour composition. The red granularity and bright green pixels have to be attributed to the noise of the BPDs. For the 2χ image the texture is still uniform although the dominant colour is a brighter shade of green.

From these images the materials doesn't seem to be birefringent since the colours are uniforms.

Now we will take a look to the phase differential images (discuss in section 4.9 that use the angle difference between the samples highlighted in yellow and the angle at the location).

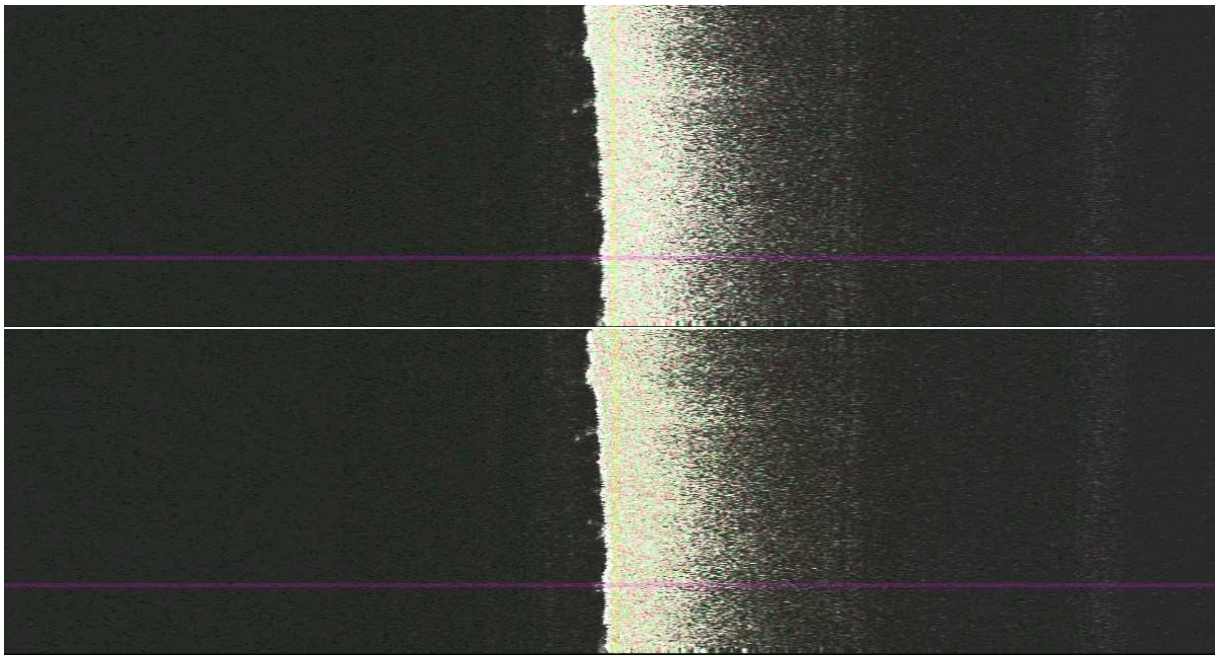

Figure 5.9: wood images of elliptical angles differences weighted by the light intensity from top to bottom we see: 2ψ and 2ϑ.

Figure 5.9 is just a whiter version of figures 5.8.

if we compare the 2ψ images with the 2χ we can notice that the images are mostly white in all the surface. This means that the elliptical angle considered is mostly unchanged in the sample and the polarization remain constant.

Since both images show the same behaviour (ie they are not changing the angles in any way) we can conclude that there is no birefringence.

5.3.2 Cotton

We are now sampling a ball of cotton. This material could display some birefringence if the fibers are oriented in the same direction due to mechanical forces; for this reason we tried manually stretching the sample.

Figure 5.10: image of the wood sample.

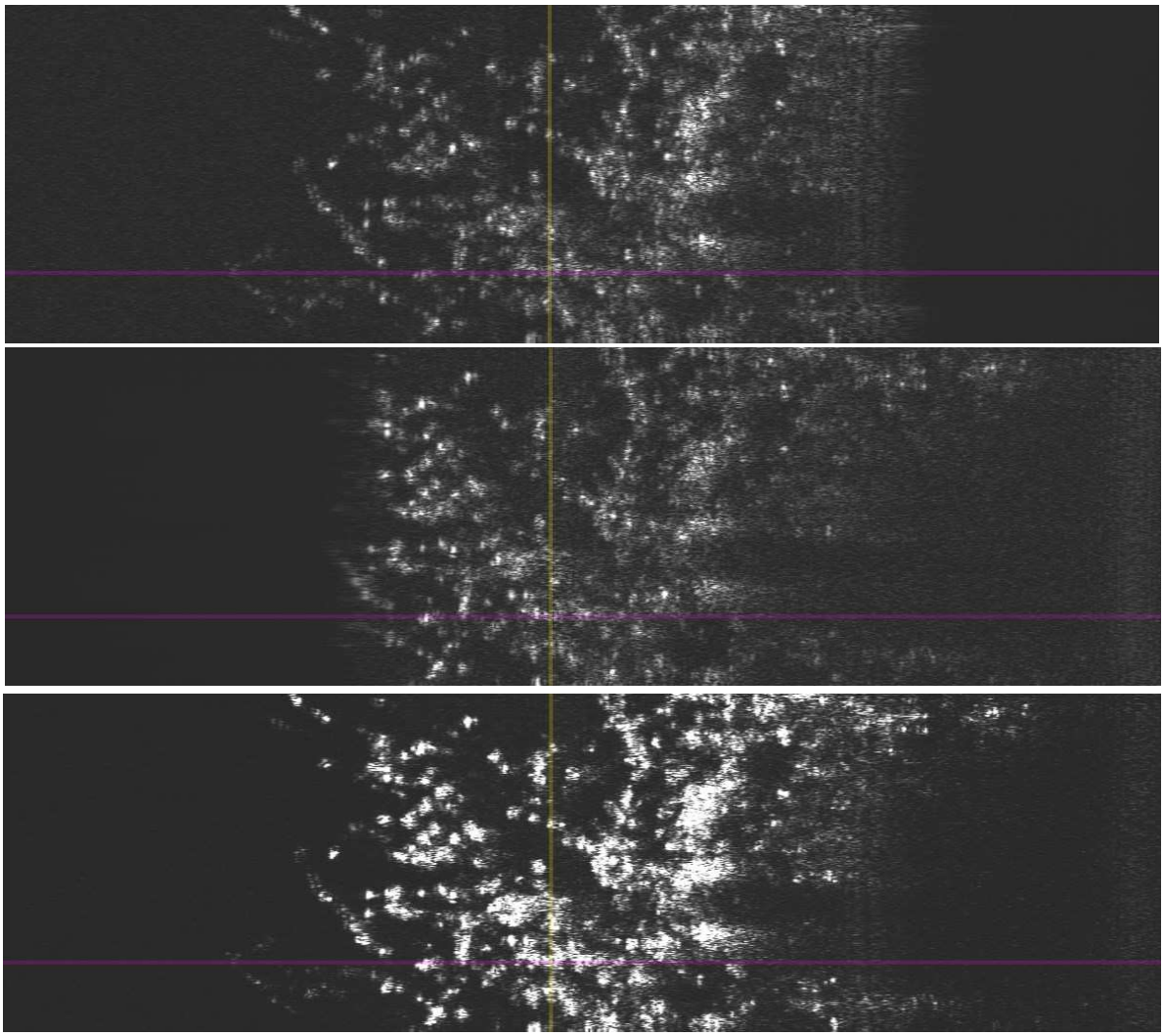

Figure 5.11: Wood images of intensity from top to bottom we see: horizontally polarized light, vertically polarized light and overall intensity (S_0).

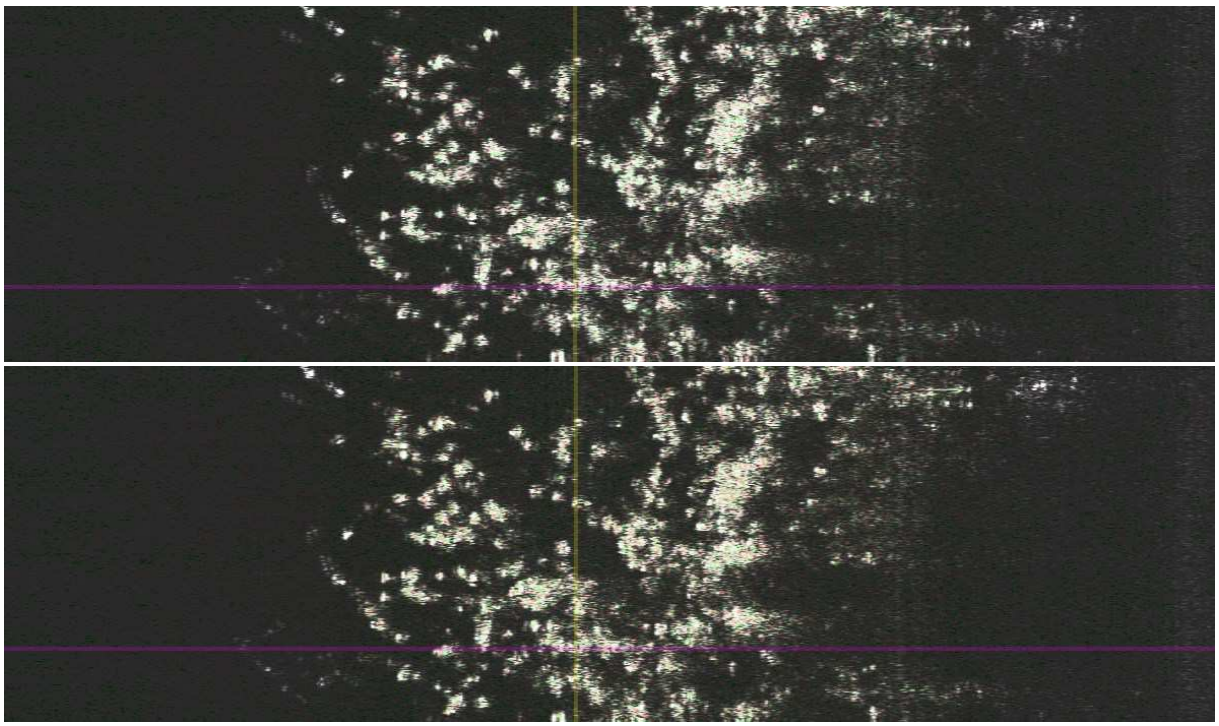

Figure 5.12: wood images of elliptical angles weighted by the light intensity from top to bottom we see: 2ψ and 2χ.

Since there isn't an actual surface we couldn't use the differential method.

Also in this case 2ψ and 2χ images shows that the polarization is largely unchanged since all the scattering centres have the same texture. We can conclude that it's not birefringent and our attempt to generate some birefringence have eighter failed or generated too little of a refractive index variation to be perceived.

5.4 Opaque birefringent materials

Here will be shown some B-scans of birefringent materials.

5.4.1 Hen Cartilage

The sample in Figure 5.13 is a cartilage taken from a chicken wing. The sample has been cooked and then extracted so some damaged may have caused variation in the refractive index due to the heat and mechanical forces that have been applied onto it.

Figure 5.13: image of the cartilage sample.

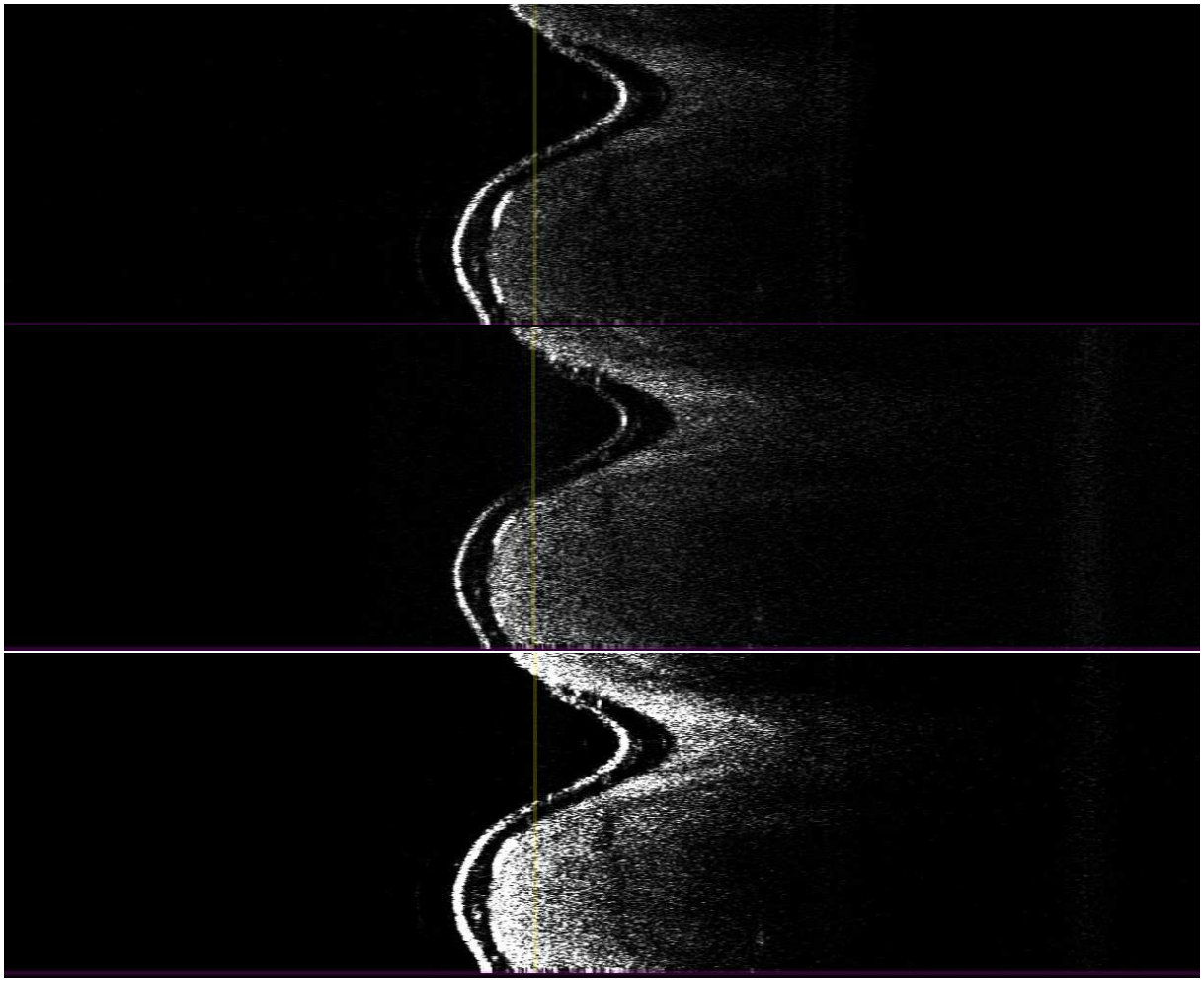

Figure 5.14: Cartilage images of intensity from top to bottom we see: horizontally polarized light, vertically polarized light and overall intensity (S_0).

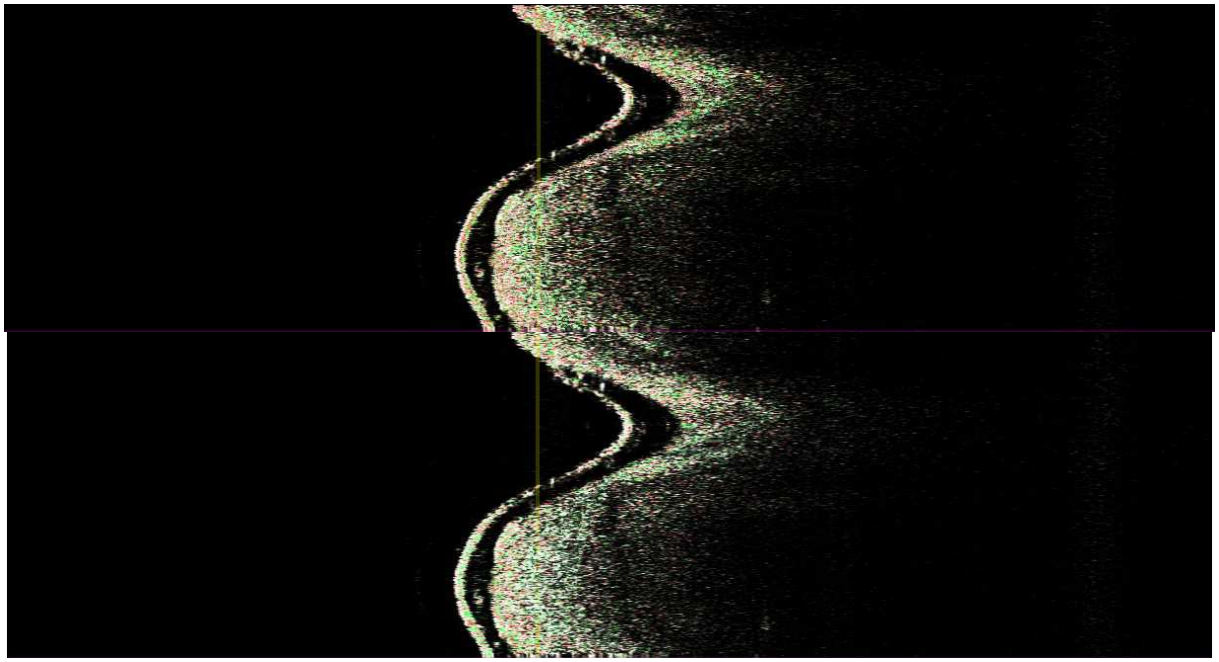

Figure 5.15: cartilage images of elliptical angles weighted by the light intensity from top to bottom we see: 2ψ and 2χ.

In figures 5.15 we can identify in the top picture (reporting 2ψ) regions dominated by the red ($\frac{\pi}{2}$) colour that evolve into green ($-\frac{\pi}{2}$).

In the 2χ image we can notice area with different pigments. In particular the second image has some red on the surface of the sample that then leaves space for a large white-green dominated region. The greenish space in in the 2χ image are close to white indicating $2\chi \approx 0$; highlighting a slower evolution. Having colour changes in the 2ψ and 2χ is the tail-tail sign of birefringence. We can conclude that our cartilage is indeed a birefringent.

Below the 5.14 images with the different coloured regions highlighted.

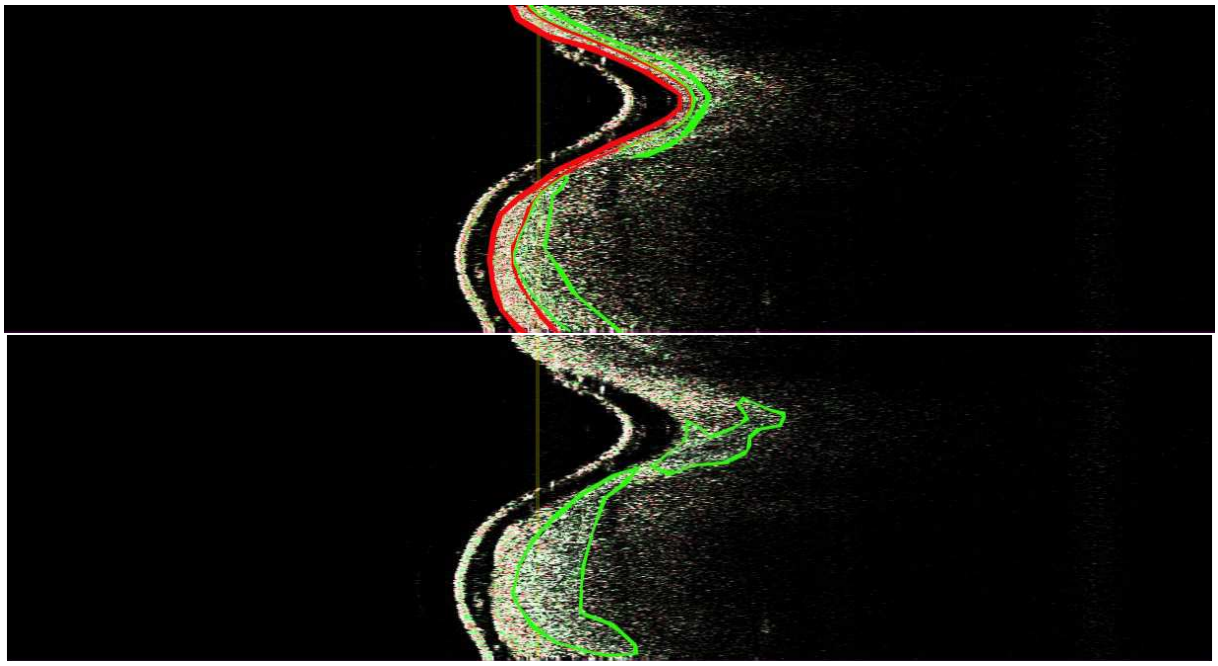

Figure 5.16: cartilage images of elliptical angles with the different area highlighted. from top to bottom we see: 2ψ and 2χ.

Last consideration. Since the two images both presents areas with different dominant colours we know that the rotation axes imposed by the birefringence does not coincide with the axes S_3 *or* S_1 since if it was the case then respectively 2χ or 2ψ wouldn't have changed.

Since the surface of the sample is not straight it wasn't possible to use the method for the mapping of the angle difference between the surface and the pixel underneath (ie at its right); this is not a problem for the diagnosis of birefringence since it doesn't provide new information but only a different type of visualization of the evolution of the elliptical angles.

5.4.2 Shark tooth

This sample is a fossilised shark tooth.

Figure 5.17: image of the tooth sample.

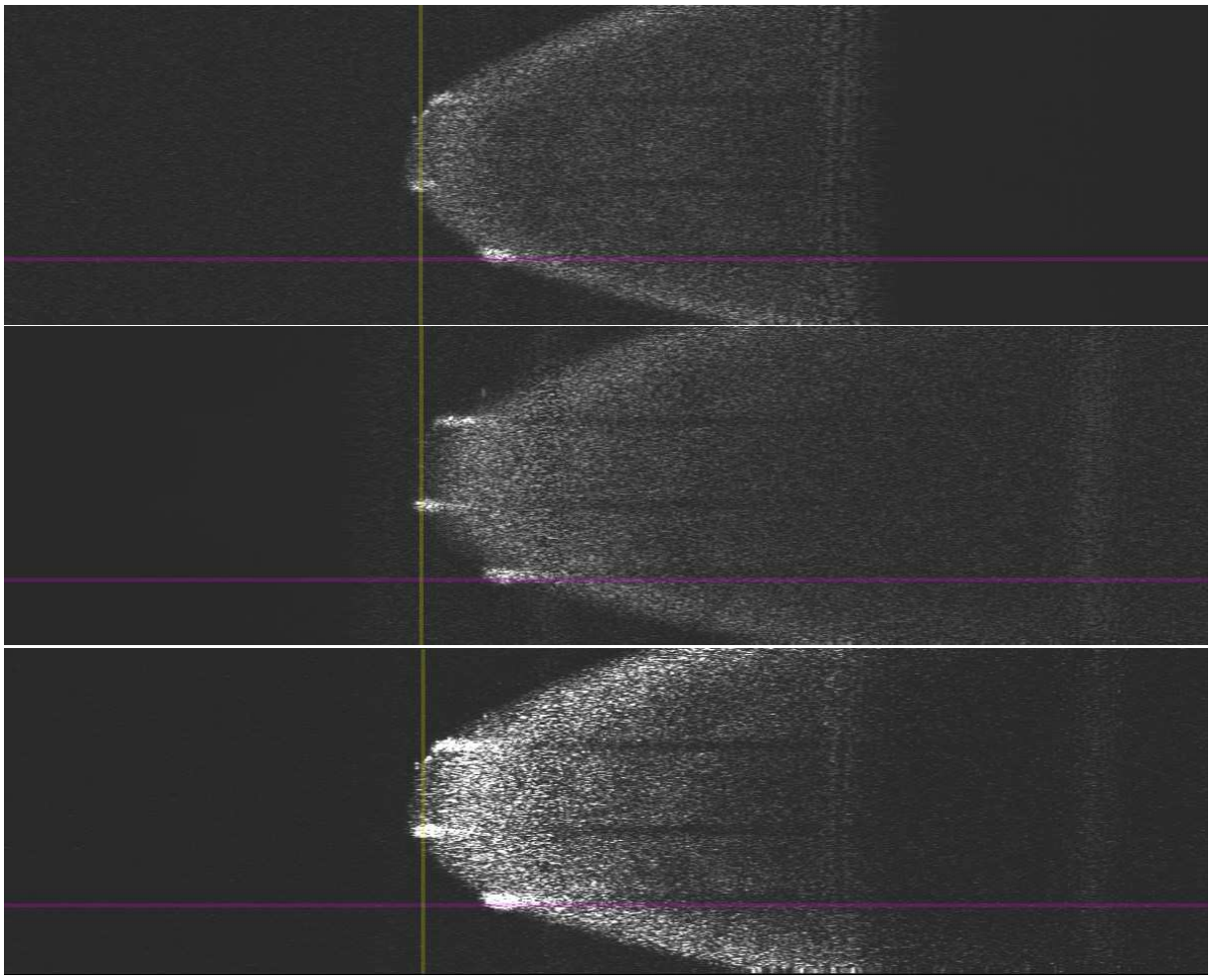

Figure 5.18: Tooth images of intensity from top to bottom we see: horizontally polarized light, vertically polarized light and overall intensity (S_0).

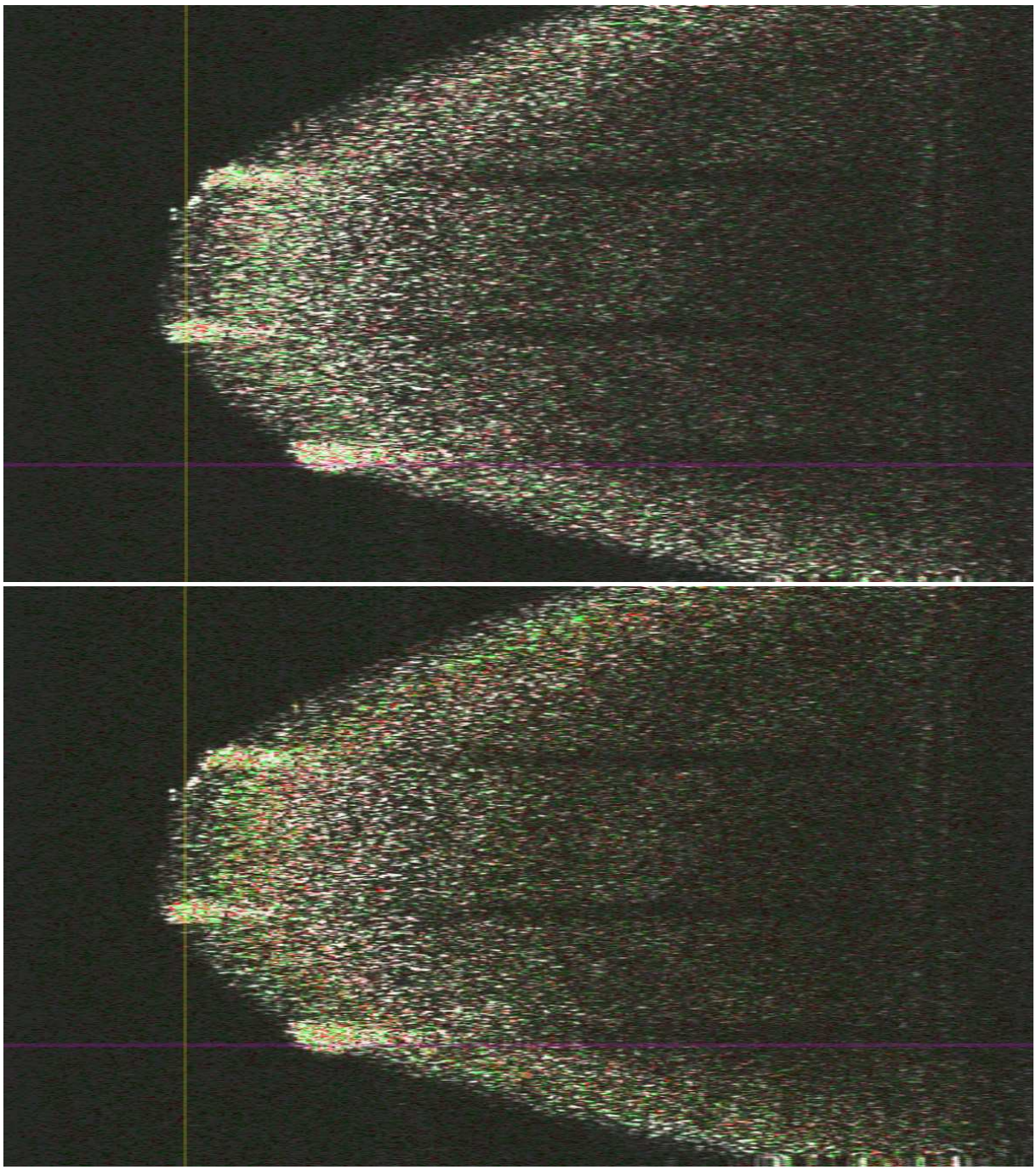

Figure 5.19: Tooth images of elliptical angles weighted by the light intensity from top to bottom we see: 2ψ and 2χ.

In figures 5.19 we can do similar consideration to those made for the cartilage.
In the 2ψ image the surface is a white with red contamination that evolves to a green. The colour change is slow, but present.
Also 2χ presents a colour shift from a light green surface to a bright green just underneath that quickly evolves to a bright red area to then fades to a whitish red.
The evolution of the elliptical angles shown through the colour changes reveals the birefringent nature of the tooth.

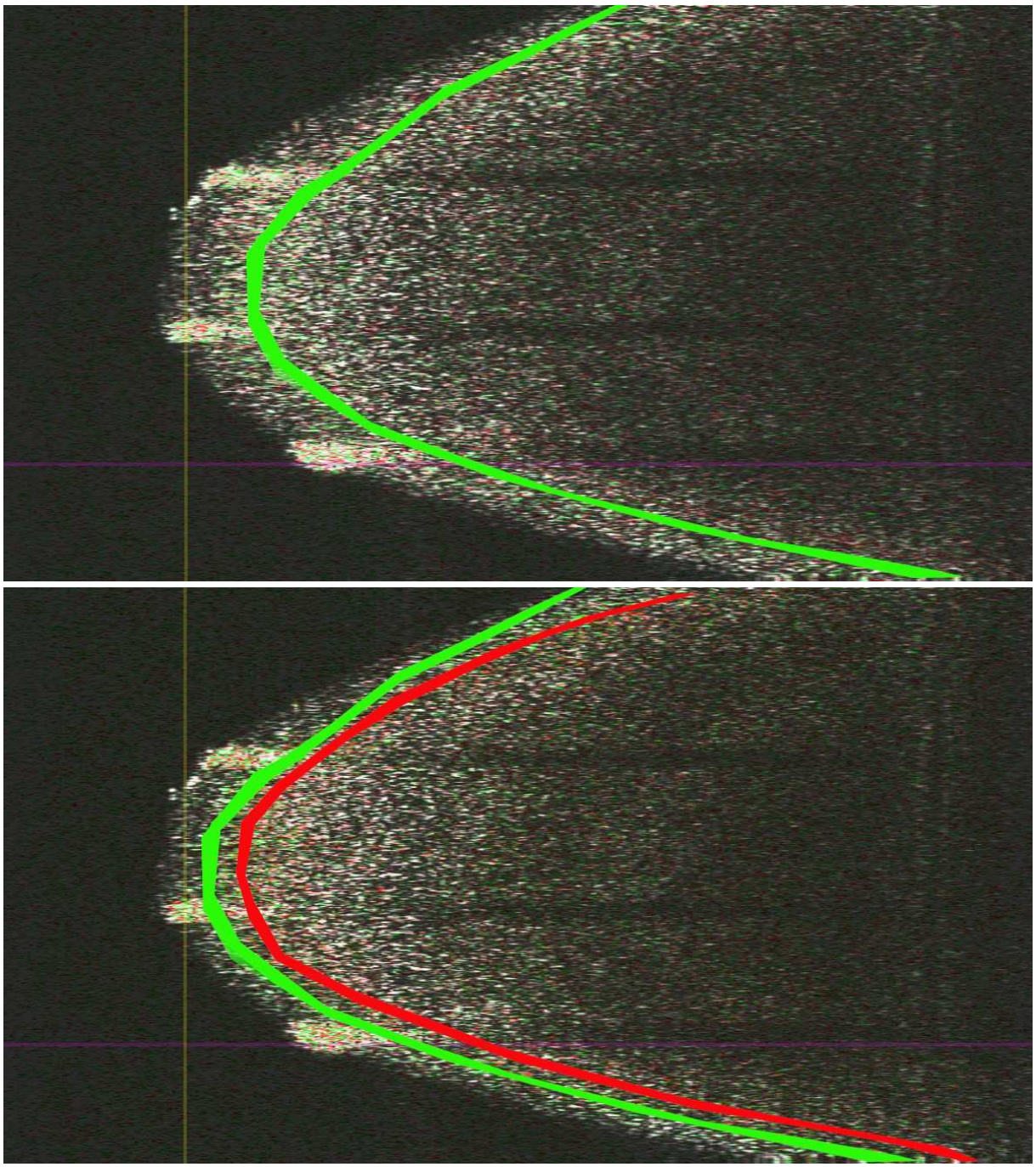

Figure 5.20: tooth images of elliptical angles with the different area highlighted. from top to bottom we see: 2ψ and 2χ.

5.5 Results of the thesis

The optical circuit created for this thesis has proven capable to accurately take images of light intensities based on the polarization.
From the two channels our software has proven capable to combine the two data streams to realize various types of images in real time. From the channel menu in the interface (Figure 5.21) we can select which image we desire to be display between.

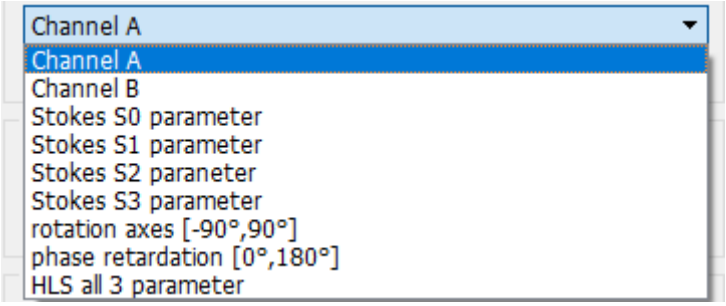

Figure 5.21: Channel menu.

The options: 1, 2, 3 allow for the display of intensity images. These intensity images are the standard requirement for an OCT device. The correct realization of these proves that we manage to correctly elaborate the interference signals measured by our BPDs.
Options :4,5,6, allow for the display of respectively: S_1, S_2 and S_3 parameters from the Stokes vector weighted using the S_0 parameter (Intensity). These images have little purpose aside for debugging and to check if we can estimate the Stokes vectors of all the pixels in real time.
Option 7 and 8 allows for the visualization of the elliptical angles. These images in particular where the key parameter to decide whether our system is a success. PS-OCT are identified by their capability to track the evolution of the polarization from traditional intensity OCTs.
Section 5.5 showed us that the system realized is capable to estimate the elliptical angles and produce images that enable to asses birefringent properties of materials.
We can then assert that the we satisfy the objective and realized a functioning PS-OCT.
It still has to be said that the set-up is affected by too many losses and hence produce noisy images. To improve this aspect it is needed the use of fibers appositely cut and improve the alignment structure for the transmission reference arm.

Conclusion

This thesis is inspired by the future developments presented in [1]. In its predecessor it was implementation of a high-speed SS-OCT system. In this thesis we evolved the setup presented in [1] by implementing two channels in order to evaluate Stokes parameters and elliptical angles to archive a PS-OCT.

A C++ OCT software has been realized in order to have real-time low-delay video while correcting dispersions and mirror curvatures. The software introduced polarization images obtained by simultaneous elaborations of the two channels.

This system has been used to sample various materials to be used for the production of intensity and elliptical angles images. Additionally, methods for the visualization of Stokes parameters images are in place. Finally, we have tried an implementation of tree parameter imaging using HLV; this method has then been discarded since it proved to produce poorly readable images.

Finally this thesis offers an explanation on how to read polarization images for then display and comment some images taken to prove the validity and achievement of the objective.

Bibliography

[1]Marcon Gianluca, Palmieri Luca, Marcon-design-of-a-realtime-OCT,

[2] J.G. Fujimoto, M.E. Brezinski, G.J. Tearney, S.A. Boppart, B.E. Bouma, M.R. Hee, J.F. Southern, E.A. Swanson, Biomedical imaging and optical biopsy using optical coherence tomography. Nat. Med. 1, 970–972 (1995)

[3] M.E. Brezinski, G.J. Tearney, B.E. Bouma, J.A. Izatt, M.R. Hee, E.A. Swanson, J.F. Southern, J.G. Fujimoto, Optical coherence tomography for optical biopsy. Properties and demonstration of vascular pathology. Circulation 93, 1206–1213 (1996)

[4] A.F. Fercher, C.K. Hitzenberger, G. Kamp, S.Y. Elzaiat, Measurement of intraocular distances by backscattering spectral interferometry. Opt. Commun. 117, 43–48 (1995)

[5] Shipman, James; Wilson, Jerry D.; Higgins, Charles A. (2015). An Introduction to Physical Science, 14th Ed. Cengage Learning. p. 187. ISBN 978-1-305-54467-3.

[6] Max Born, Emil Wolf, A. B. Bhatia, P. C. Clemmow, D. Gabor, A. R. Stokes, A. M. Taylor, P. A. Wayman, and W. L. Wilcock. Principles of Optics: Electromagnetic Theory of Propagation, Interference and Diffraction ofLight. 7th ed. Cambridge University Press, 1999. doi: 10.1017/CBO9781139644181.

[7] J.S. Schuman, C.A. Puliafito, J.G. Fujimoto, Optical Coherence Tomography of Ocular Diseases, 2nd edn. (Slack, Thorofare, 2004)

[8]Optical Coherence Tomography second Edition; Authors: Wolfgang Drexler, James G. Fujimoto; publisher: SpringerReference; publishing year 2015.

[9] M.A. Duguay, A.T. Mattick, Ultrahigh speed photography of picosecond light pulses and echoes. Appl. Optics 10, 2162–2170 (1971)

[10] Dong-hak Choi, Hideaki Hiro-Oka, Kimiya Shimizu, and Kohji Ohbayashi. «Spectral domain optical coherence tomography of multi-MHz A-scan rates at 1310 nm range and real-time 4Ddisplay up to 41 volumes/second.» In: Biomedical Optics Express 3.12 (2012), p. 3067. issn: 2156-7085. doi: 10.1364/BOE. 3.003067. url: https://www.osapublishing.org/abstract. cfm?URI=boe-3-12-3067.

[11] A.D. Aguirre, P. Hsiung, T.H. Ko, I. Hartl, J.G. Fujimoto, High-resolution optical coherence microscopy for high-speed, in vivo cellular imaging. Opt. Lett. 28, 2064–2066 (2003)

[12] J.A. Izatt, M.R. Hee, G.M. Owen, E.A. Swanson, J.G. Fujimoto, Optical coherence microscopy in scattering media. Opt. Lett. 19, 590–592 (1994)

[13] G.J. Tearney, M.E. Brezinski, B.E. Bouma, S.A. Boppart, C. Pitvis, J.F. Southern, J.G. Fujimoto, In vivo endoscopic optical biopsy with optical coherence tomography. Science 276, 2037–2039 (1997)

[14] G.J. Tearney, S.A. Boppart, B.E. Bouma, M.E. Brezinski, N.J. Weissman, J.F. Southern, J.G. Fujimoto, Scanning single-mode fiber optic catheter-endoscope for optical coherence tomography. Opt. Lett. 21, 543–545 (1996)

[15] Wolfgang Drexler and James G. Fujimoto, eds. Optical Coherence Tomography. Cham: Springer International Publishing, 2015. isbn: 978-3-319-06418-5. doi: 10.1007/978-3-319-06419-2. url: http://link.springer.com/10.1007/978-3-319-06419-2.

[16] J. Zhang, J.S. Nelson, Z.P. Chen, Removal of a mirror image and enhancement of the signalto-noise ratio in Fourier-domain optical coherence tomography using an electro-optic phase modulator. Opt. Lett. 30(2), 147–149 (2005)

[17] X. Clivaz, F. Marquis-Weible, R.P. Salathe, Optical low coherence reflectometry with 1.9 mm spatial resolution. Electron. Lett. 28, 1553–1554 (1992)

[18] M. Wojtkowski, A. Kowalczyk, R. Leitgeb, A.F. Fercher, Full range complex spectral optical coherence tomography technique in eye imaging. Opt. Lett. 27(16), 1415–1417 (2002)

[19] J G Fujimoto, C a Puliafito, R Margolis, A Oseroff, S De Silvestri, and E P Ippen. «Femtosecond optical ranging in biological systems.» In: Optics Letters 11.3 (1986), p. 150. issn: 0146-9592. doi: 10.1364/OL.11.000150. url: https://www.osapublishing.org/abstract.cfm?URI=ol-11-3-150

[20] Y. Wang, T. Funaba, T. Ichimura, N. Tanno, Optical multimode time-domain reflectometry. Rev. Laser Eng. 23, 273–279 (1995)

[21] MaciejWojtkowski, Rainer Leitgeb, Andrzej Kowalczyk, Tomasz Bajraszewski, and Adolf F. Fercher. «In vivo human retinal imaging by Fourier domain optical coherence tomography.» In: Journal ofBiomedical Optics 7.3 (2002), p. 457. issn: 10833668. doi: 10.1117/1.1482379. url: http://biomedicaloptics.spiedigitallibrary.org/article.aspx?doi=10.1117/1.1482379.

[22] A.F. Fercher, C.K. Hitzenberger, W. Drexler, G. Kamp, H. Sattmann, In vivo optical coherence tomography. Am. J. Ophthalmol. 116, 113–114 (1993)

[23] David Huang et al. «Optical Coherence Tomography HHS Public Access.» In: Science. November 22.2545035 (1991), pp. 1178– 1181. issn: 0036-8075. doi: 10 . 1002 / jcp . 24872 . The. arXiv: 15334406.

[24] J.A. Izatt, M.D. Kulkarni, H.-W. Wang, K. Kobayashi, M.V. Sivak Jr., Optical coherence tomography and microscopy in gastrointestinal tissues. IEEE J. Sel. Top. Quantum Electron. 2, 1017–1028 (1996)

[25] C.F. Bohren, D.R. Huffman, Absorption and Scattering of Light by Small Particles (Wiley, New York, 1983)

[26] .J. Gil, E. Bernabeu, Obtainment of the polarizing and retardation parameters of a non-depolarizing optical system from the polar decomposition of its Mueller matrix. Optik 76(2), 67–71 (1987)

[27] W.A. Shurcliff, S.S. Ballard, Polarized Light (Van Nostrand, New York, 1964)

[28] Marinko V. Sarunic, Michael A. Choma, Changhuei Yang, and Joseph A. Izatt. «Instantaneous complex conjugate resolved spectral domain and swept-source OCT using 3x3 fiber couplers.» In: Optics Express 13.3 (2005), p. 957. issn: 1094-4087. doi: 10. 1364/OPEX.13.000957. url: https://www.osapublishing.org/ oe/abstract.cfm?uri=oe-13-3-957.